The Pennsylvania State University

The Graduate School

DESIGN, MODELING AND TESTING OF AN ELECTRO-THERMAL ICE PROTECTION SYSTEM FOR WIND TURBINES

A Thesis in

Aerospace Engineering

by

David V. Getz

Submitted in Partial Fulfillment

of the Requirements

for the Degree of

Master of Science

December 2019

The thesis of David V. Getz was reviewed and approved* by the following:

Jose L. Palacios
Associate Professor of Aerospace Engineering
Thesis Advisor

Dennis McLaughlin
Professor of Aerospace Engineering

Amy Pritchett
Professor of Aerospace Engineering
Head of the Department of Aerospace Engineering

*Signatures are on file in the Graduate School

Abstract

There has been a substantial growth in the total installed wind energy capacity worldwide, especially in China and the United States. Icing difficulties have been encountered depending on the location of the wind farms. Wind turbines are adapting rotor ice protection approaches used in rotorcraft applications to reduce aerodynamic performance degradation related to ice formation. Electro-thermal heating is one of the main technologies used to protect rotors from ice accretion and it is one of the main technologies being considered to protect wind turbines.

In this research, an anti-icing configuration using electro-thermal heating was explored to find optimum power density requirements to keep the rotor blade free of ice at all times. The objective of these experiments were to identify the feasibility of the power requirements from the stake holders and determine an initial power density for the de-icing approach. The electro-thermal heater system located on the spinning wind turbine representative blade sections were powered through a slip-ring. The wind turbine sections were ½ scale models of the 80% span region of a generic 1.5 MW wind turbine blade. The icing cloud impact velocity was matched with a 1.5 MW wind turbine at full production. Three icing conditions were selected for this research: Light, Medium and Severe. Light icing conditions were created using clouds at -8°C with a 0.2 g/m^3 liquid water content (LWC) and water droplets of 20 µm median volumetric diameter (MVD). Medium icing condition clouds had a LWC of 0.4 g/m^3 and 20 µm MVD, also at -8°C. Severe icing conditions had an LWC of 0.9 g/m^3 and 35 µm MVD at -8°C. Experimental anti-icing results were compared with LEWICE, a NASA developed analytical heat transfer software. The average output temperature discrepancy between the suction and pressure sides of the airfoil were 39.5% and 11.1%, respectively. The correlation coefficient of the pressure-side output temperature and power density showed a positive correlation of 0.9516. The anti-icing configuration with the allocated power requirements was deemed unfeasible.

This thesis then discusses the design process required to develop a de-icing ice protection system (ice is allowed to accrete to then be removed) for wind turbines and a design procedure was developed. Initially, ice accretion thickness gradients along the span of the rotor blade for light, medium and severe icing conditions were collected. Ice accretion rates along the span of the representative full-scale turbine blade in the severe icing condition ranged from 1.125 mm/min to 1.85 mm/min. Given the maximum power available for the de-icing system (100 kW), heating zones were determined along the span and the chord of the blade. The maximum available power density for each span-wise heater section was 0.385 W/cm^2. The heating sequence started at the tip of the blade, to allow de-bonded ice to shed off along the span of the rotor blade due to centrifugal forces. Given the continuity of the accreted ice, heating a zone could de-bond the ice over that specific zone, but the ice formation could not detach from the blade as it would be cohesively connected to the ice over its adjacent inboard zone. The research determined the critical minimum ice thickness required to shed the accreted ice mass with a given amount of power availability by not only melting the ice interface over the zone, but also creating sufficient tensile forces to break the cohesive ice forces between two adjacent heating zones. The quantified minimum ice thickness to overcome ice cohesive forces were obtained for all identified icing conditions. The minimum ice thicknesses required for effective shedding at 26.7%, 44.4% and 62.2% of the span were 7.2mm, 5mm and 4mm, respectively. The digitized ice areas of these thicknesses were used to calculate the centrifugal force at each heater section. The experiment data was critical in the design of a time sequence controller that allows consecutive de-icing of heating zones along the span of the wind turbine blade with the allocated power.

Table of Contents

List of Figures

List of Tables

List of Symbols

A	-	Disk area (m)
AoA	-	Angle of attack (°)
A_{CS}	-	Cross-sectional area (m^2)
C_d	-	Drag coefficient
C_l	-	Lift coefficient
C_m	-	Pitching moment coefficient
CF_{AERTS}	-	Centrifugal force in AERTS facility (N)
CF_{WT}	-	Centrifugal force on the wind turbine (N)
C_p	-	Specific heat capacity $\left(\frac{\mathrm{J}}{\mathrm{kgK}}\right)$
D	-	Disk area (m)
GW	-	Gigawatt
H	-	Test model height distance (m)
HP	-	Horsepower
k	-	Thermal conductivity $\left(\frac{W}{mK}\right)$
k_{ref}	-	Thermal conductivity at reference temperature $\left(\frac{W}{mK}\right)$
kW	-	Kilowatt
L_{AERTS}	-	Length of heater section in AERTS (m)
L_{WT}	-	Length of heater section on wind turbine (m)
LWC	-	Liquid Water Content $\left(\frac{g}{m^3}\right)$
m	-	Slope of temperature dependence $\left(\frac{W}{mK^2}\right)$
m_{AERTS}	-	Ice mass of the heater section in AERTS
m_{WT}	-	Ice mass of the heater section on wind turbine

MVD	-	Median volumetric diameter (μm)
P_w	-	Available wind power (Watts)
r_{AERTS}	-	Radius to rotation axis in AERTS
r_{WT}	-	Radius to rotation axis on wind turbine
RPM	-	Revolutions per minute
T	-	Temperature (Kelvin)
T_{ref}	-	Reference temperature (Kelvin)
u	-	Incoming air velocity $\left(\frac{m}{s}\right)$
USB	-	Universal Serial Bus
V	-	Volt
α	-	Thermal diffusivity $\left(\frac{W}{mK^2}\right)$
ρ	-	Density $\left(\frac{kg}{m^3}\right)$
μ	-	Micro unit denoting a factor of 10^{-6}
Ω_{AERTS}	-	Rotational velocity at heater section in AERTS
Ω_{WT}	-	Rotational velocity at heater section on wind turbine

Acknowledgments

I would like to sincerely thank my advisor and mentor, Dr. Jose Palacios, for his time, effort, commitment and support during my time as a graduate student. His advice and ambitious nature make me very proud to have studied under his direction. The knowledge and professional skills I have acquired and developed through this experience are significantly impacted by Dr. Palacios. Obtaining this degree from The Pennsylvania State University would have never been possible without Dr. Palacios's commitment and determination to acquire funding for the research. I would like to thank Dr. Dennis McLaughlin for the NASA Fellowship recommendation. The additional heat transfer research for different applications and the overall collaboration shaped my interpersonal skills and broaden my knowledge of the industry. I would like to give a special thank you to my colleague, Sihong Yan. His academic knowledge and skills were indispensable throughout my research. I have great respect for him and consider him a leader, advisor and mentor. Gratitude is also extended to my colleague, Grant Schneeberger, for his initial recommendation to Dr. Palacios and support through my experimental studies.

Finally, I would like to thank my family for their unconditional love and support throughout my life. My parents have taught me manners, integrity, respect and responsibility, which I am deeply grateful for. Growing up with a self-employed father delivered a skillset and a type of thinking that I cannot explain. Lastly, all would fail if I did not have such an amazing wife. She gives me the strength to carry on through the ups and downs, so I would like to dedicate this hard work as a small token of appreciation for her endless love.

Chapter 1: Introduction

1.1 Problem Statement

Wind turbines are located on wind farms that experience hazardous icing events. Due to the ice formation altering aerodynamic performance, the estimated loss of total annual energy production (AEP) is approximately 20% [13-15]. With the power requirements given from the stake holder, can an ice protection system be designed, modeled and tested within reasonable costs? This research developed a design procedure for an ice protection system in the de-icing configuration with the common goal of not exceeding the power limitations from the stake holder. Experimental data coupled with LEWICE modeling guided this research to successful develop an ice protection system for the wind turbine of interest.

1.2. Thesis Objective

The objective of this research was to design and test an ice protection system (IPS) for wind turbines. The electro-thermal system possesses the capability to perform as an anti-icing and de-icing system. The goal of the anti-icing mode is preventing ice accretion. The de-icing system's goal is to enforce controlled shedding of thin ice layers with the benefit of reduced power consumption with respect to the anti-icing configuration. Ideally, an anti-icing solution would be used. This thesis assesses if anti-icing electro-thermal techniques are feasible given typical power availability for IPS from the turbine.

To achieve these objectives, the goals of this research are to:

- Use LEWICE to model the anti-icing heater configurations and ice accretion at different atmospheric and velocity conditions. The analytical predictions can assist the assessment of feasibility of anti-icing schemes and to guide heater coverages and power densities for a de-icing approach.

- For model verification, compare LEWICE results to experimental results for the anti-icing configuration.
- Define the ice accretion slope along the span of the turbine blade for several icing conditions.
- Through experimentation, determine the minimum ice thickness at each heater zone to produce centrifugal ice shedding and overcome ice cohesive forces.
- Evaluate the optimal power density required to effectively shed ice accretion in the de-icing configuration.
- Design a time sequence controller and procedure for the de-icing ice protection system based on the experimental data obtained.

1.3 Thesis Overview

These research objectives will be addressed and subdivided into the following chapters:

Chapter 2: LEWICE Modeling

The analytical software, LEWICE 3.2, was chosen and utilized to model the transient icing physics in various atmospheric conditions. These efforts are conducted to become aware of ice predictions and match the anti-icing experimental results. A MATLAB batch code was developed to acquire the capability of mass-producing modeling results and perform trade studies.

Chapter 3: Facility Overview and Experiment Set-Up

An overview of The Adverse Environment Rotor Test Stand (AERTS) was presented. The liquid water content (LWC) was calibrated for the blade geometry in AERTS. The Arduino set-up, LabVIEW interface and testing procedures were also discussed in this chapter.

Chapter 4: Results and Verification

Output temperature results in the anti-icing configuration were compared with LEWICE predictions. The optimum power density was determined for the severe icing condition as a conservative approach. Experimental results for ice accretion rate vs span percentage, centrifugal shedding, and power variation are presented for the de-icing configuration. The de-icing IPS is developed and designed.

Chapter 5: Conclusions and Recommendations

The final chapter discusses conclusions drawn from this research and offers recommendations for future work. Recommendations for future work are based on the results and observations during experimentation.

1.4. Wind Turbine Industry

1.4.1. Wind Turbine Overview

Among renewable resources, wind energy is the only that provides a mature technique and also has promising commercial prospects and large-scale electricity generation [1, 2]. Wind energy has been used to generate electrical power for over 100 years. It began when Professor James Blyth, from Scotland, designed a windmill to generate electricity in 1887 [3]. The following year, 1888, the wind machine was constructed by Bruch and installed for operation on the Atlantic coast. This event solidified the direction of the engineering for the wind power market. During the 1920s and 1930s, the United States widely developed wind machines (<1 kW) in rural areas. This period experienced a peak popularity for wind machines; the United States installed approximately 600,000 units across the country [1, 4]. The industry boomed again during the oil crisis in the 1970s [5]. The price of oil rose significantly, which led to the focus on wind power development in the 1990s. Many countries adopted this energy generation method, like China, United States, Germany, Spain, Denmark, India and Turkey. These countries made substantial contributions towards the progression of wind energy [1, 6]. It is predicted that 5% of the world's energy will be produced from wind power generation by 2020 [7]. In the last decade, the average annual growth for the world's wind power generation was approximately 30% [8]. Shown in Figure 1 is the global wind power capacity installed between 1990 and 2015. The y-axis represents the installed capacity ranging from 0 to 450 GW. According to the World Energy Association, it is estimated that the capacity will reach 292GW in 2012 and 425 GW by 2015 [8, 9].

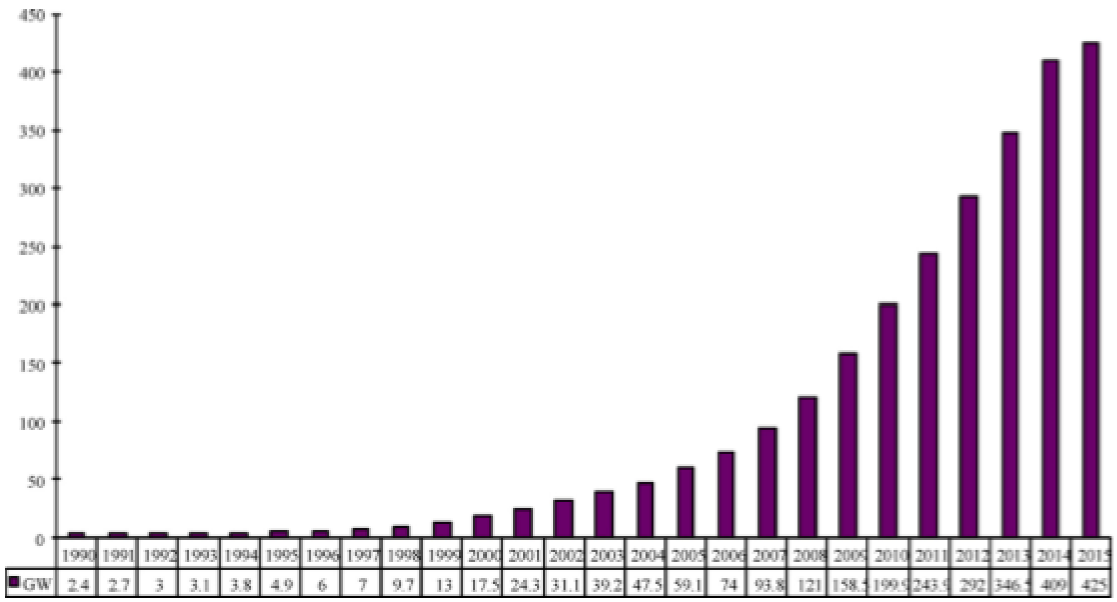

Figure 1: Global wind power capacity installed, GW, 1990-2015 [8, 9].

In 2009, the United States installed 10 GW with a total installed capacity of 40.2 GW. It is estimated that wind energy will generate 20% of the nation's electricity in 2030. Currently, it produces 2% of the nation's electricity [10]. In 2010, China surpassed the United States as the world's leader of wind power with a total installed capacity of 42.3 GW; a 64% increase through 2009. This is no surprise considering China's installed capacity nearly doubled each year since 2006. The total exploitable wind capacity in China, for both onshore and offshore, is around 700-1200 GW, according to the third National Wind Energy Resources Census [6]. The expansion of

China’s wind energy is predicted to reach 90 GW by 2015 and 200 GW by 2020. Shown in Figure 2 is the installed capacity of the leading wind power countries from 2001 to 2011 [10, 11].

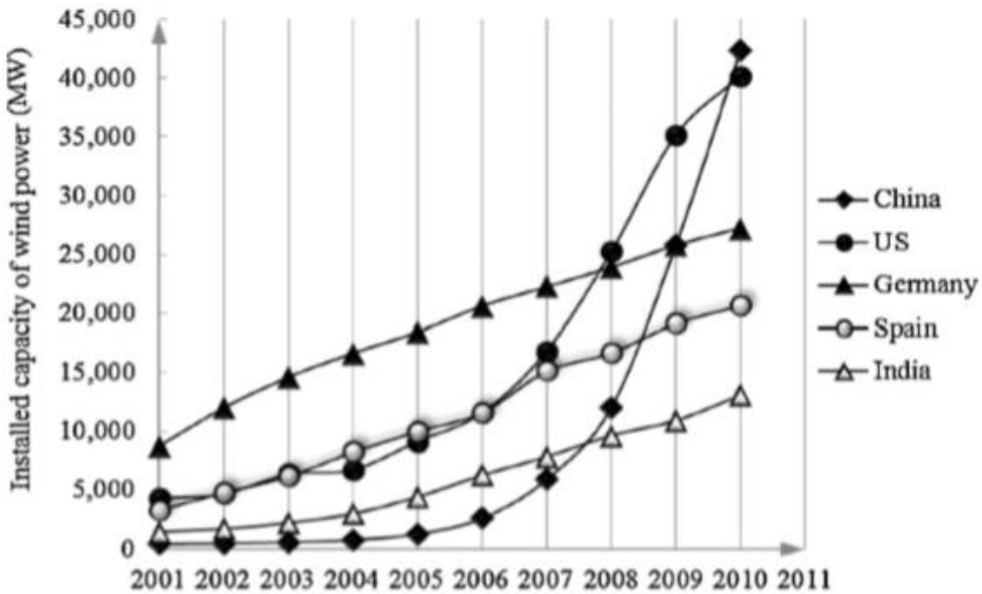

Figure 2: Installed win power capacity in leading countries [10, 11].

In 2010, the leading countries for wind power generation were China, United States, Germany, Spain and India. They had a total installed capacity of 42.3 GW, 40.2 GW, 27.2 GW, 20.7 GW and 13.0 GW, respectively. Most of these countries have onshore and offshore wind turbine sites. The advantages of onshore wind turbines include lower foundation cost, easier installation and integration of electrical systems, and more convenient accessibility for maintenance and operations. Offshore wind turbines developed faster than onshore, because the wind power is more intense and consistent. An offshore wind turbine can generate more wind power and operate for longer periods of time compared to onshore wind turbines [12].

The evolution of wind power has progressed successfully, but it also creates drawbacks. Wind turbines have strong environmental impact, such as noise, visual and climatic impact. The drawbacks are quite minor compared to fossil fuels, but the drawbacks should not be disregarded.

It is imperious to solve the minor drawbacks so the wind energy market can reach and maintain its' potential, regarding the world's energy generation.

1.4.2. Wind Turbines in Adverse Weather

Unfortunately, most wind turbines located in the northern hemisphere experience hazardous icing events due to the periodic cold climate of their location. It is known that air density changes with temperature and air density directly affects the power output of the wind turbine. The formula for available wind power is shown in Equation (1).

$$P_w = \frac{1}{2}\rho A u^3 \tag{1}$$

By exploring equation (1), there is a direct relationship between air density and power output, where the density is ρ ($\frac{g}{m^3}$) and available power output is P_w (Watts). The higher air density provides more available power output from the wind turbine. Therefore, the power output increases as temperature decreases. Also, the available power output of the wind turbine is proportional to the disk area of the blades, A, and the incoming velocity of the air, u. The accumulation of ice on the wind turbine will alter the blade geometry and degrade the aerodynamic performance of the rotor blade. The accumulation of ice is a complex combination of temperature, liquid water content (LWC) and median volumetric diameter (MVD), with many other variables. Many studies have shown that icing events led to severe losses in aerodynamic performance. The estimated loss of the total annual energy production (AEP) is approximately 20% [13-15]. A study regarding the energy loss during the winter season was piloted by Gillenwater et al. The study collected wind farm data over four winter seasons at two separate sites [16]. The data concluded that the average power loss between both sites was approximately 27%. Gillenwater stated that "the operational procedures during an icing event should be modified in order to reduce the risks (performance losses) and maximize production”. Continuous ice accretion can significantly affect the structural loading of the rotor blade leading to potentially hazardous situations. Often, severe icing conditions cause a complete loss of production due to the shut-down of the wind turbine [17]. A photograph of rime ice accretion on a wind turbine in Mt. Equinox, Vermont is shown in Figure 3. The photo on the right shows a close-up view of the ice accretion on the rotor blade and mechanical systems.

Figure 3: Photograph of rime ice accretion on a wind turbine in Mt Equinox, Vermont.

Wind tunnel experiments by Han et al. were conducted using a NACA 0012 airfoil in the Pennsylvania State University Adverse Environment Rotor Test Stand (AERTS). The accreted ice mass was molded then utilized for wind tunnel testing [18]. The aerodynamic performance was recorded over a series of angles of attack (AoA) and the effects of drag, lift and pitching moment are presented in Figure 4. The left figure represents drag coefficient vs AoA and the right figure exhibits lift force vs pitching moment coefficient.

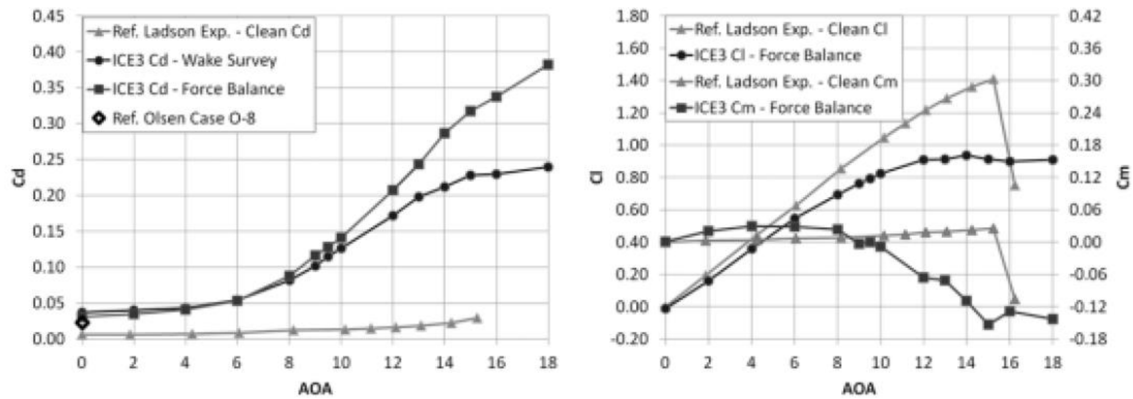

Figure 4: NACA 0012 drag, lift and pitching moment coefficients vs AoA [18].

The increase in drag is due to the accreted ice shapes on the leading edge of the airfoil. Angles of attack below 6° generate a relatively minor increase in the drag coefficient (C_d). The drag coefficient significantly increases for angles of attack greater than 6°. A wake probe survey concluded that the lift coefficient (C_l) was 35% lower with ice than clean airfoil for an angle of attack just before stall (~15°). The pitching moment (C_m) of the clean airfoil was relatively constant through the range angles of attack. With accreted ice on the airfoil, the pitching moment (C_m) possessed a strong relationship with angle of attack.

Icing conditions have led to research in various anti-icing and de-icing ice protection systems. Anti-icing systems prevent the rotor blade from accumulating any ice, while a de-icing IPS systems purposely shed off accumulated ice mass, periodically. The anti-icing IPS consume massive amounts of power because they operate continuously and must maintain the blade surface temperature above freezing. De-icing approaches run periodically and take advantage of the insulation effect of ice accretion. Among active ice protection systems, heating is currently the most efficient approach for wind turbines experiencing moderate to severe icing conditions [19, 20]. Hot air injection and electro-thermal techniques are the leading systems for effective heating systems. The advantage of the electro-thermal is the ability to be installed on existing wind turbines. However, all passive and active ice protection systems possess drawbacks. For example, anti-icing systems must minimize runback water from freezing on the aft section of the airfoil. The re-freezing of runback water can be prevented by subliming the ice interface of accreted ice. For an anti-icing configuration, the heater extent in the aft direction must be such that prevents running water from re-freezing on unprotected areas. The additional area coverage needed for anti-icing systems make them require larger power than de-icing. The anti-icing mode requires approximately 5 times more energy to operate, rendering it as too expensive for wind turbines. Manufacturers prefer to use the power to generate electricity rather than power ice protection systems, even though a cost analysis of the benefits of anti-icing integration versus energy production during icing events has not been found in the literature.

1.5. Icing Physics

1.5.1. Icing Conditions

Many icing parameters are interdependent of another and each play a role determining the accretion rate and shape of the ice. The characteristics of the ice are prescribed by the atmospheric temperature, droplet size, water content, and accretion time. The droplet size in the cloud is defined by the median volumetric diameter (MVD) in μm [21]. The MVD of the water droplet is a characteristic number that denotes the average water droplet size in an icing cloud. For consistency, an MVD is widely used to characterize the size of the droplets for all icing facilities. In reference [21], the measured MVD is tested as a function of air temperature. This correlation is shown in Figure 5 and the different symbols represent different data sources [22]. In the Adverse Environment Rotor Test Stand (AERTS) at The Pennsylvania University, the MVD is controlled by the input ratio of air and water to the NASA calibrated spraying nozzles [23]. The sensors on the nozzles provide the capability to determine the particle size by the input air pressure.

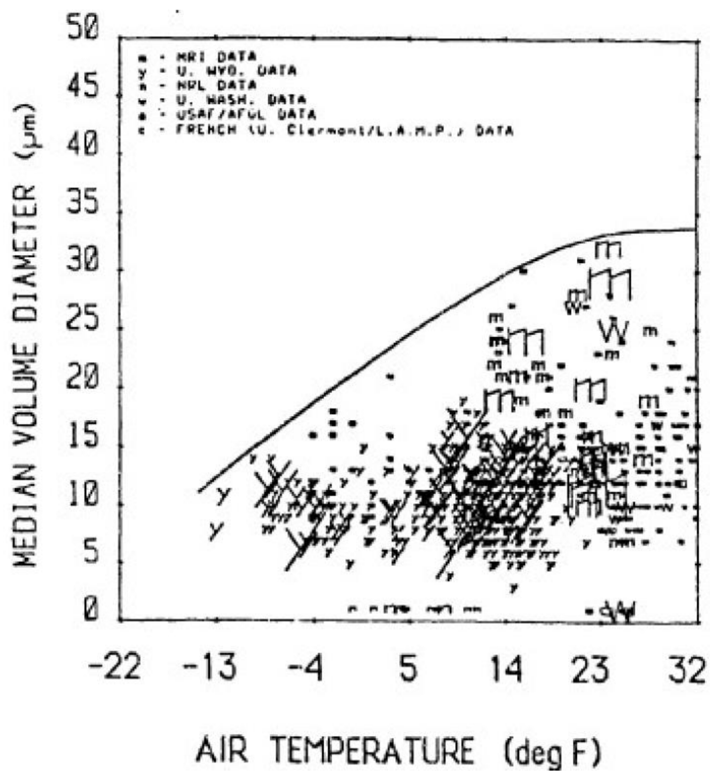

Figure 5: Measured MVD correlation with air temperature [22].

The water content of the icing cloud is defined by the liquid water content (LWC) in g/m^3. The LWC unit implies the water content per unit volume of the incoming air. It is the characteristic water-to-air concentration in a two-phase flow. Larger LWC values indicate more water content in the icing cloud. The data correlation with air temperature is recommended and suggested by the Federal Aviation Administration (FAA) in the Federal Aviation Regulations (FAR) Part 25 and Part 29 Appendix C [23]. The relationship of LWC and air temperature is shown in Figure 6 [22].

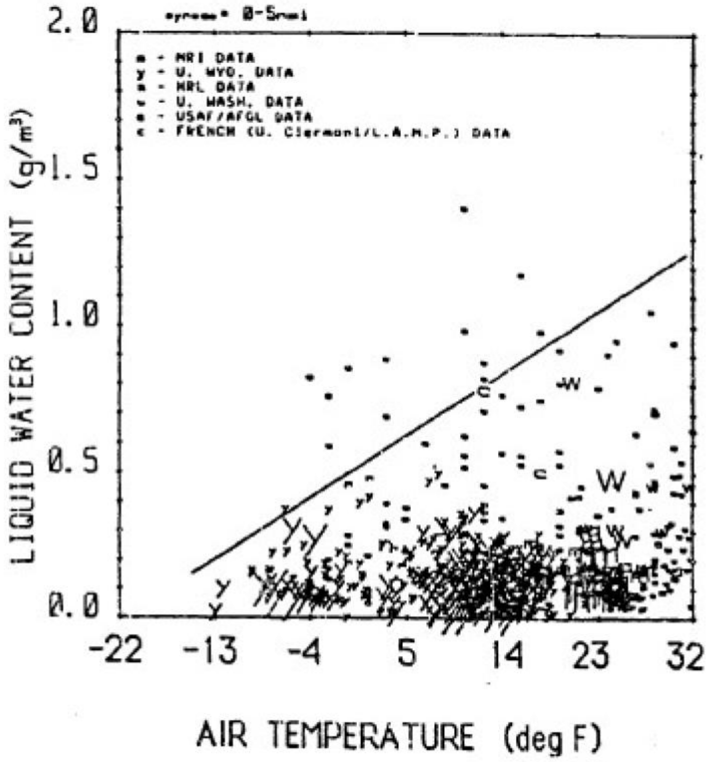

Figure 6: Measured LWC correlation with air temperature [22].

The analysis of MVD and LWC combinations need to be considered for proper characterization of an icing cloud. The sharp decline in MVD and LWC as the temperature decreases is shown in Figures 5 and 6. Typically, larger MVD-LWC combinations at warmer temperatures are more severe than lower MVD-LWC combinations at colder temperatures. Water possesses a large specific heat capacity, therefore, larger quantities of frozen water on the surface require more energy to eliminate or melt. Electro-thermal techniques seek low energy consumption schemes while ensuring effective ice protection systems.

Icing clouds can be categorized in two different meteorological forms: Stratiform and cumuliform clouds. Stratiform clouds are evenly distributed with a range of 17.4 nautical miles. This cloud form is referred to as "continuous". Cumuliform clouds are based on convective clouds with a range of 2.6 nautical miles [23]. A cumuliform cloud is referred to as "intermittent". During continuous icing events, less severe icing conditions are experienced. The continuous icing envelope is presented in Figure 7. The LWC ranges from 0.06 g/m^3 to 0.8 g/m^3 and the MVD ranges from 10 µm to 40 µm [24]. Intermittent clouds produce icing conditions with more severity. The intermittent icing envelope is shown in Figure 8. The LWC ranges from 0.3 g/m^3 to 2.9 g/m^3 and the MVD ranges from 15 µm to 50 µm [24]. For wind turbines, it is expected that cumuliform clouds will be very rare. The icing conditions that will be explored in this work will correspond to the continuous icing envelope.

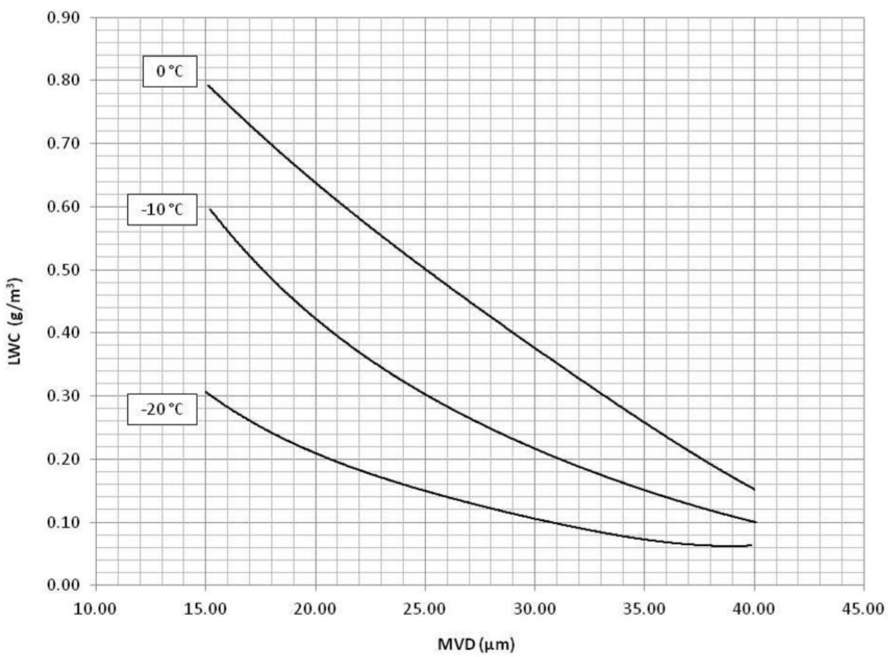

Figure 7: FAA Continuous icing envelope [24].

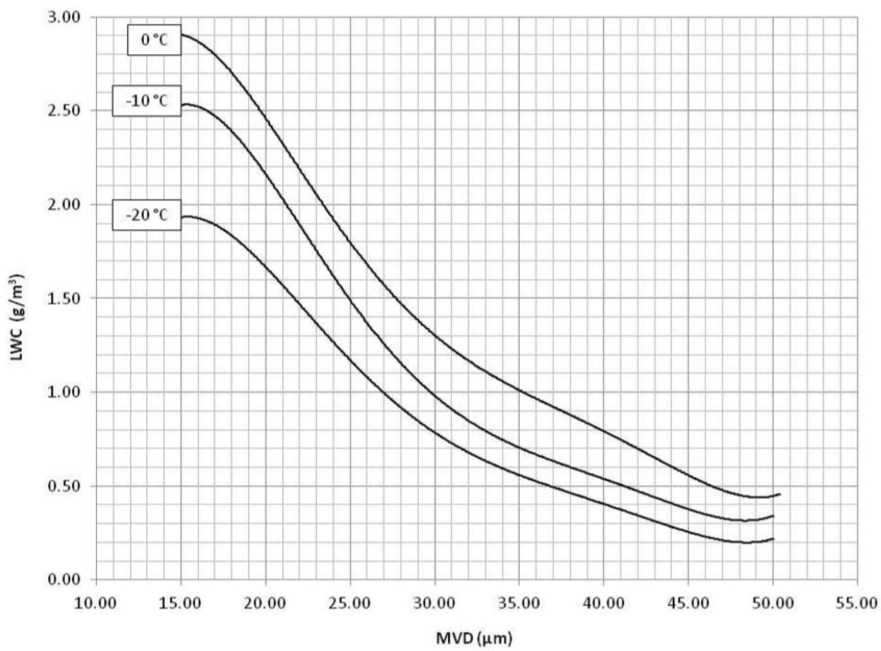

Figure 8: FAA Intermittent icing envelope [24].

1.5.2. Ice Shapes

The freezing of the super-cooled droplets can be complete or partial depending on how rapidly the latent heat of fusion can be released into the ambient air. There are two distinct icing regimes: rime and glaze. In a dry regime, all the water collected in the impingement area freezes on impact and forms rime ice. Rime ice is typically encountered at cold temperatures, small MVDs and low LWCs. Rime ice tightly conforms to the shape of the object accreting ice, which results in less severe aerodynamic penalties than glaze ice. Rime ice shapes tend to be more streamlined and possess a milky opaque appearance. In a wet regime, only a fraction of the collected water freezes on the impingement area forming glaze ice. The remaining water runs back and can freeze outside the impingement area. Glaze ice is usually associated with warmer temperatures, above -10°C, and larger LWC-MVD combinations. Glaze ice presents difficult challenges due to its' wet nature that results in deformed ice shapes relative to the surface component. The formation of horns and feathers possess complex shapes and structures, which grow in the direction into the airflow. The horns and feathers increase drag and drastically degraded aerodynamic performance. The increase in drag is due to the airflow separation after the horns and feathers. Three ice shapes from different icing regimes are exhibited in Figure 9. From left to right, it presents typical glaze, mixed and rime ice shapes. In general, glaze ice is more dangerous than rime since it possesses an irregular ice surface and protruded horns.

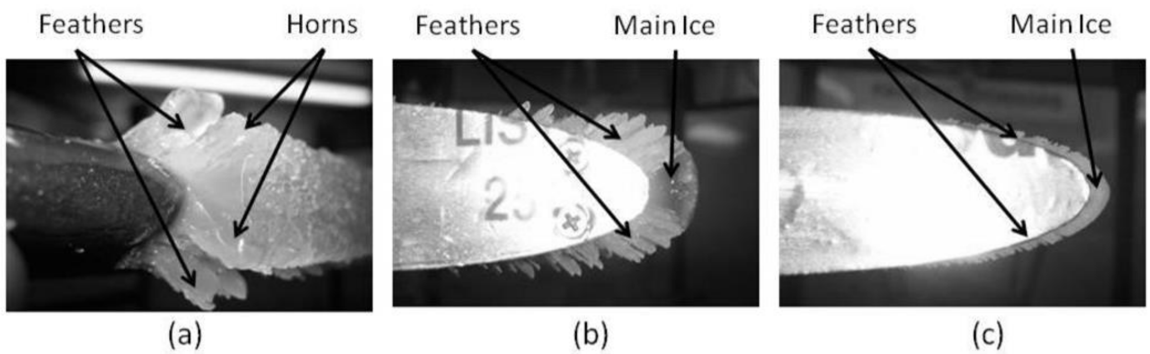

Figure 9: Glazed (a), Mixed (b), and Rime (c) ice regimes [37].

1.6. Ice Protection Systems

1.6.1. Electro-thermal

Electro-thermal techniques are the most common ice protection systems utilized in the field. Its' simplicity and ability to retrofit to existing wind turbines makes it an attractive option for stake holders. For wind turbines, it is imperative to protect the lower surface of the airfoil due to high angles of attack. The electro-thermal system sends electrical current to resistive circuits, which convert electrical energy to thermal energy. These resistive circuits are known as the heating elements. The heating elements are integrated into the rotor blade, which can sometimes lead to blade delamination. The risk of delamination can be reduced when the blade surface temperature is maintained below 50°C. The heating elements are typically adhered underneath the blade skin and coverlay. Coverlay is a material laminated to insulate the copper conductor. The blade skin is the layer of protection used to prevent surface erosion. The thermal energy converted from electrical energy in the heating elements travel through the layers via conduction. A simplified schematic of the layers is shown in Figure 10.

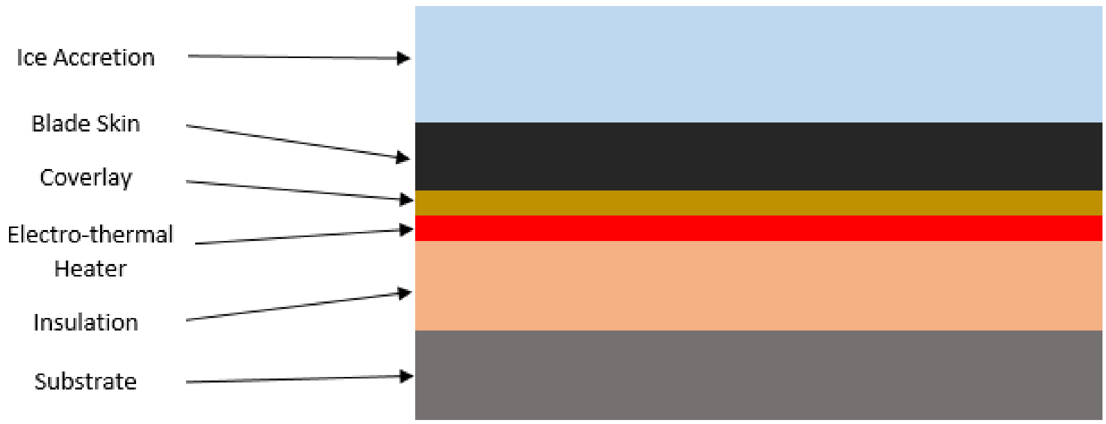

Figure 10: Simplified electro-thermal IPS schematic.

Electro-thermal ice protection systems in anti-icing mode can produce runback water that freezes on the aft section of the blade. The runback water will build an ice wall and severely degrade the aerodynamic performance of the airfoil. The re-freezing of runback water can be prevented by evaporating the impingement of super cooled water droplets. The evaporative mode for anti-icing systems require about 5 times more energy to operate. To minimize power consumption, it is recommended to divide the heaters into span-wise or chord-wise sections and cycle power to those heating elements. In the late 1970's, Sikorsky developed an ice protection system for the rotor blades on the UH-60 Black Hawk [25]. The helicopter is set to operate in -20°C conditions with a maximum LWC of 1.0 g/m^3. The initial design possessed four chord-wise heating elements on the outboard section of the rotor blade that were supplied power simultaneously. The unprotected inboard section caused an undesirable increase of torque, so the final design extended the heaters span-wise. Due to power restrictions, the IPS on the blades could only be powered in pairs. The proposed ice protection system experienced six hours of flight-testing in the artificial cloud produced by the US Army's CH-47 Helicopter Icing Spray System (HISS) and 20 hours of natural icing conditions in Minnesota. Testing confirmed the ability of the electro-thermal IPS to protect the UH-60 Black Hawk [25].

A Low Power Electro-thermal De-icing (LPED) system was developed by Goodrich. The LPED system does not send continuous or cycled AC electricity to the heating elements like conventional methods. The IPS system consists of a parting strip at the stagnation point of the airfoil and de-icing zones aft of the parting strip in the chord-wise direction. The parting strip was cycled from the 28 electric volt system to prevent ice accretion at the stagnation point on the leading edge. The temperature was monitored and limited to 220°F by a Resistance Temperature Device (RTD). The runback water refreezes on the de-icing zones. The de-icing zones received pulse energy from 3500 farad capacitors that discharged every three minutes for 1.4 seconds. During the winter of 2003 and 2004, the LPED system was flight-tested on a fixed wing aircraft and effectively protected the rotor blade in icing conditions for 20% to 50% less power than conventional systems [26].

The most recent conventional IPS powered by electro-thermal is a carbon nanotube (CNT). CNT's are manufactured and patched together to make a heating element. The fabrication process starts by growing CNTs 80 μm to 100 μm tall on a silicon wafer. Then, a sheet of nonporous Teflon is placed over the CNT and a steel tool with a small radius compresses the CNT in the plane of the silicon wafer. This process creates the heating element patch, which are placed side by side on a sheet of epoxy film and cured to build larger heating elements. Two heaters were bonded on the surface of a wing section and tested in the Cox & Company wind tunnel. The CNT IPS system was able to anti/de-ice at -5°F using a range of power densities between 0.6 W/in^2 to 5 W/in^2, but the system also had ice bridging issues from unprotected areas [27]. A three-step schematic shown in Figure 11 illustrates the fabrication process of a CNT compressed onto a Silicon wafer using guaranteed nonporous Teflon (GNPT) [28].

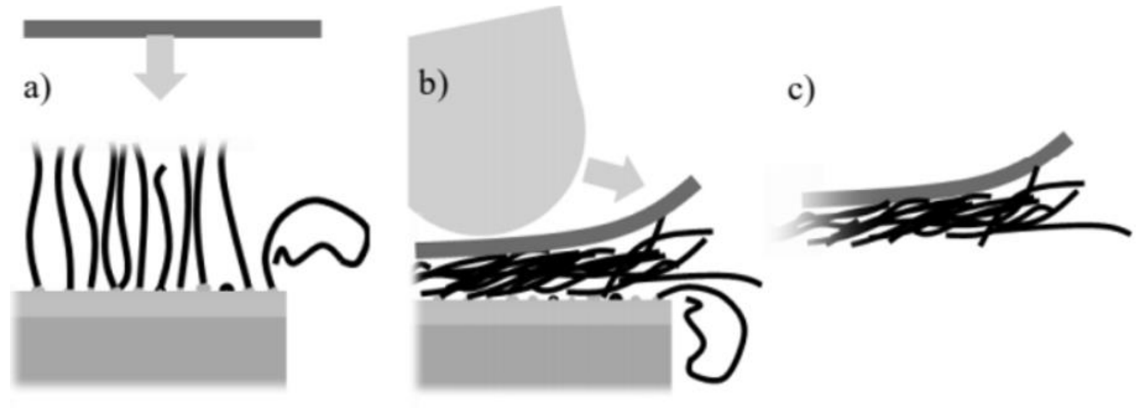

Figure 11: Schematic of CNT fabrication process [28].

1.6.2. Low Ice Adhesion Coatings

Low ice adhesion coatings are a type of passive ice mitigation techniques. They have a wide spread of applications in several industries. Regarding icing systems, the ice will naturally shed faster from a surface with lower adhesion strength. Passive systems are typically implemented for stake holders that cannot afford an active ice protection system. This category of materials is sometimes referred to as icephobic (even though a material that prevents ice formation has not been found). These coatings/materials can be integrated with an active anti-icing IPS to remove runback water. Superhydrophobic coatings are suitable for water, but are not feasible for impact icing. A low adhesion coating would minimize the amount of ice buildup before the ice naturally sheds from centrifugal forces. The major drawback for low ice adhesion coatings is the significant degradation of material properties due to erosion. Typically, these coatings are susceptible to maximum erosion on the leading edge of the airfoil due to the impact velocity of the particles. The US Army Aviation Applied Technology Directorate, Boeing and The Pennsylvania State University collaborated to test a wide range of potential leading edge materials for ice adhesion strength. Testing discovered that the icephobic coatings worked relatively well in the early stages, but severely degraded over time due to erosion. The adhesion strength for the eroded coating was five times higher than the original [29]. A comparison of adhesion strength for leading edge materials before and after erosion is presented in Figure 12.

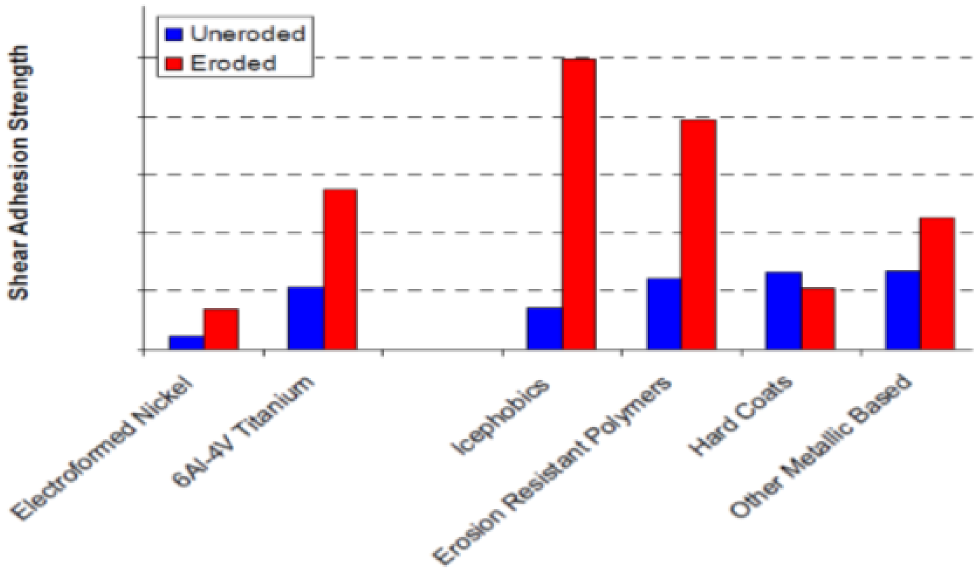

Figure 12: Comparison of adhesion strength for leading edge materials [29].

An icephobic coating was evaluated by NuSil, a silicon manufacturer. The coating, R-2180, was made from silicon material and possessed a significantly lower ice adhesion strength compared to other commercial coatings. At the 2012 American Helicopter Society (AHS) International forum, NuSil presented a paper that demonstrated the R-2180 coating attaining an adhesion strength 27 times lower than titanium and 14 times lower than stainless steel, two typical rotor blade leading edge materials. Unfortunately, the R-2180 coating was not tested for erosion characteristics at the time [30]. A comparison between the NuSil R-2180 and other commercial coatings is exhibited in Figure 13.

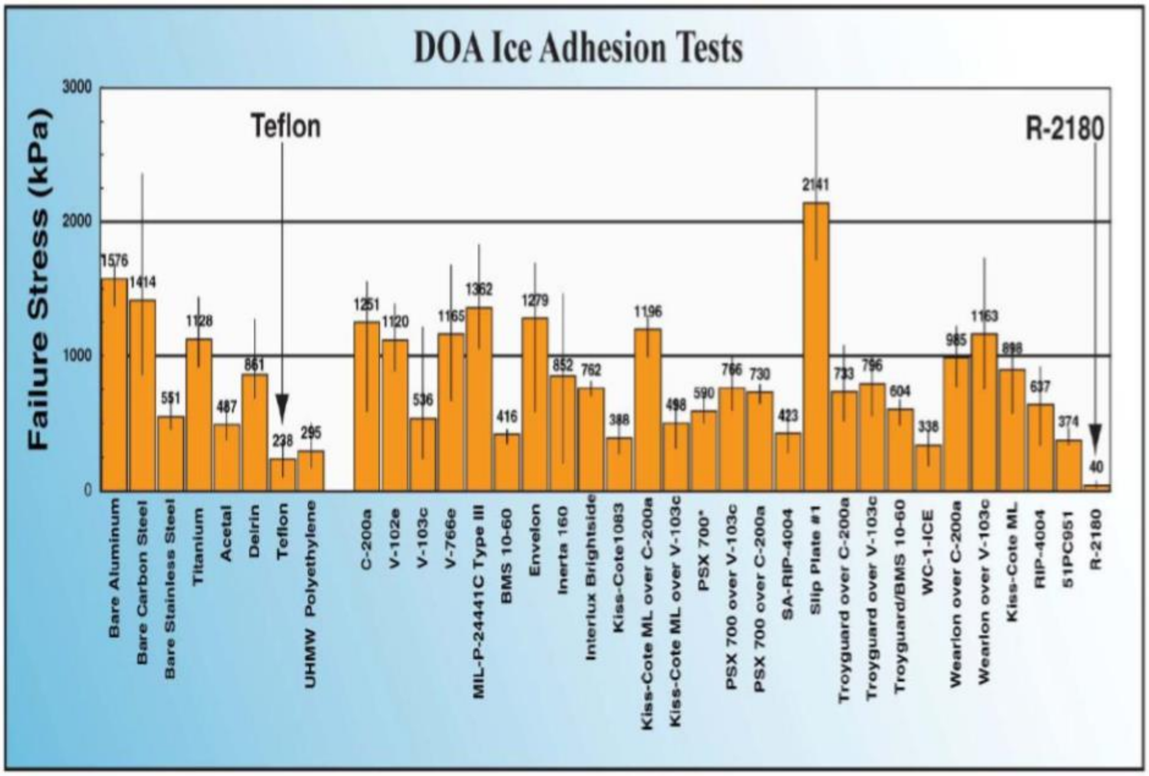

Figure 13: Adhesion strength comparison between NuSil R-2180 and other commercial coatings.

1.6.3. Electro-impulsive

Other ice protection methods exist, and they will be briefly mentioned. The electro-impulsive de-icing mitigation technique utilizes a coil of copper ribbon wire mounted to the span-wise spar on the ribs with a small gap between the coil and wing skin. The coils are supplied power from a bank of high voltage capacitors, which stores and discharges the energy. When the capacitors discharge energy, it creates an eddy current in the skin from the expansion and decay of the magnetic field. The magnetic fields repel each other with large forces in small displacements, which results in high accelerations. Two or three impulses from the ice protection system will delaminate and debond the ice mass on the surface. These ice protection systems are designed for fixed-wing aircraft that have a hollow leading edge. Blades for rotorcraft have solid leading edge to support bending loads, and removing material from the solid leading edge would degrade the stiffness of the blade. The electro-impulsive IPS typically consumes 1kW for general fixed-wing aircraft and 3kW for a medium sized helicopter [31]. A configuration schematic of the leading edge cap for an electro-impulsive IPS is shown in Figure 14. A cross-sectional view of the magnetic force (left) and a top-view of the copper Eddy coil is shown in Figure 15 [32].

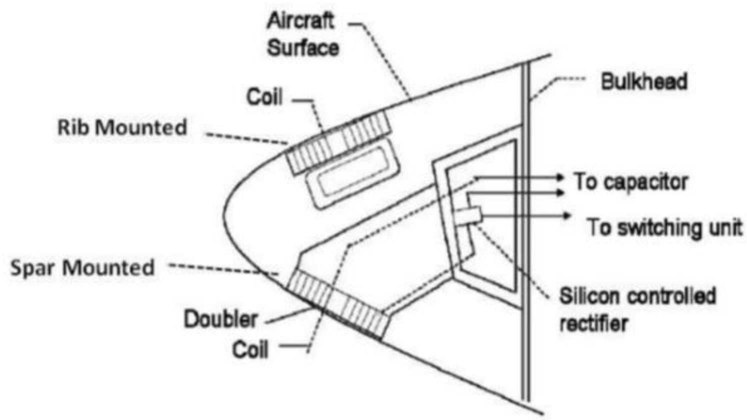

Figure 14: Electro-impulsive configuration schematic [27].

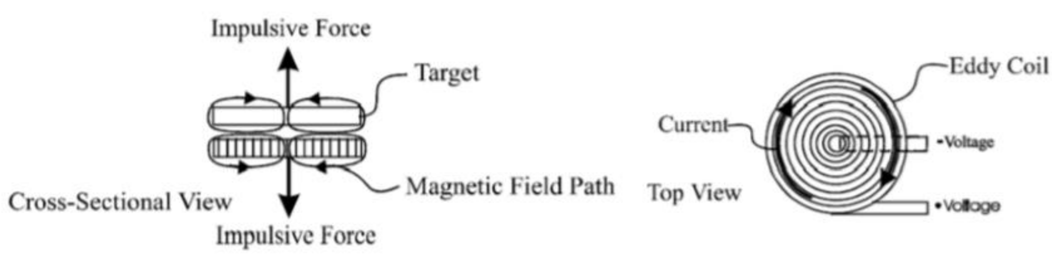

Figure 15: Cross-sectional view of magnetic force (left), and top-view of eddy coil (right) [32].

1.6.4. Pneumatic Systems

Pneumatic de-icing systems utilize mechanical energy to debond accreted ice opposed to thermal energy and is typically referred to as a pneumatic boot. This ice mitigation technique is used on systems with taut power and weight limitations. The boots are usually made from a neoprene material, synthetic rubber, for operational design and flexibility. When pressure is applied to the boot, it inflates and creates transverse shear stress along the ice-boot interface. The interface delaminates as soon as the shear stress overcomes the ice adhesion strength [33, 34]. A schematic of the pneumatic IPS with a layer of accreted ice is illustrated in Figure 16. An operational schematic for the pneumatic boot creating transverse shear stress that overpowers the adhesion strength of the ice is shown in Figure 17.

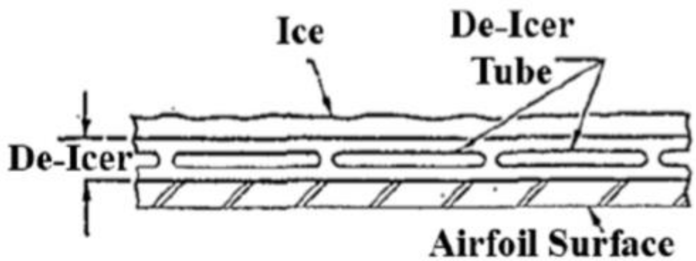

Figure 16: Pneumatic IPS schematic with accreted ice layer

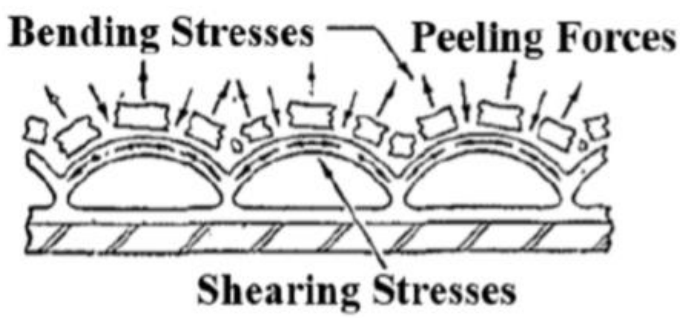

Figure 17: Operational schematic of pneumatic de-icing system.

A disadvantage of the pneumatic boot IPS resides with ice thickness. The system operates over a predetermined range of ice thicknesses. If the accreted ice thickness is too large, then the transverse shear stresses from inflation cannot delaminate the ice-boot interface. If the ice layer is too thin, then it develops a small flexible ice layer that creates imperfections, deeming the system unreliable. Therefore, pneumatic systems require a sensor that detects ice thickness and signals the pilot to active the de-icing system. Prototype pneumatic boots, developed by Goodrich, were retrofitted to the leading edge of the UH-1 main rotor blades in a chord-wise and span-wise orientation. The design utilized bleed air from the turbine engine to inflate the boots in two seconds. The pneumatic IPS prototype successfully delaminated ice at temperatures as cold as -20°C with LWCs as high as 0.8 g/m^3. It was also determined that the minimum thickness required for effective shedding was 0.3 inches (0.762 cm). The prototype boot tested on the UH-1 is presented in Figure 18 [31].

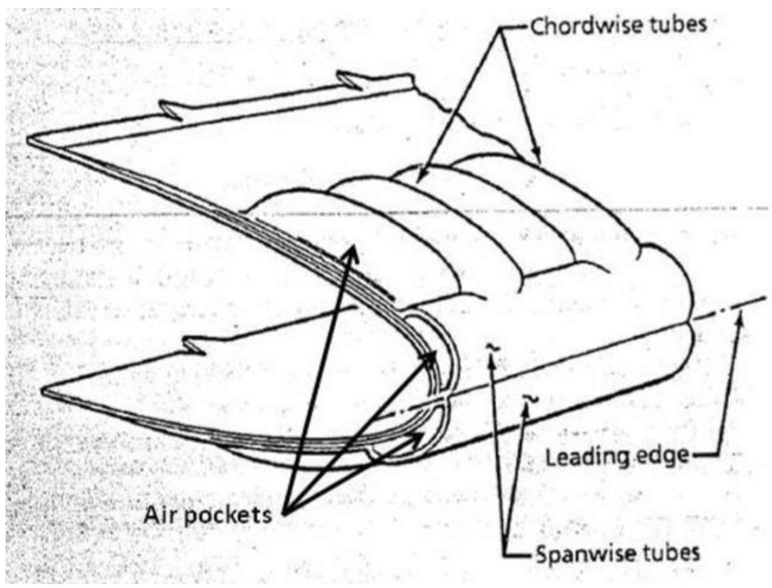

Figure 18: Prototype pneumatic boot tested on the UH-1 [31].

Chapter 2: Modeling

The analytical software, LEWICE 3.2, was chosen and used to model the icing physics in various atmospheric conditions. These efforts are conducted to evaluate the capability of the software to predict ice accretion when thermal energy is introduced and more importantly, determine if anti-icing schemes are feasible. Results were compared with experimental data for both anti-icing and de-icing configurations.

2.1. LEWICE

2.1.1. LEWICE Introduction

The evaluation of aircraft systems in icing conditions is important for both design and certification. Testing evaluation in icing facilities can be expensive, so it is beneficial for the manufacturer to analytically predict the performance of the system over a range of icing conditions to guide the system design and reduce testing time prior icing trials.

LEWICE is a computer software that contains an analytical ice accretion model that evaluates the thermodynamics of the freezing process that occurs when super-cooled water droplets impinge on a body [41]. To determine the shape of the ice, the atmospheric and meteorological conditions must be known as inputs. Atmospheric conditions consist of temperature, pressure and velocity, while meteorological conditions entail liquid water content, droplet diameter and relative humidity.

The software has four major modules: flow field calculation (panel method), particle trajectory and impingement evaluation based on Messinger's model, thermodynamic and ice growth calculation, and modification of current geometry by adding ice growth [35]. Initially, the flow field and droplet impingement characteristics are determined for the clean geometry. The thermodynamic model determines the ice accretion growth rate on each segment of the surface. LEWICE applies a time-stepping procedure to modify the ice accretion growth. When a time increment is specified in the main input file, this growth rate can be interpreted as an ice thickness and the body coordinates are adjusted to account for the accreted ice. This procedure is repeated until the desired icing time in the main input has been reached.

LEWICE can model any number of heaters, any chord-wise length, and any heater gap desired by modifying the heat transfer. The heaters may be controlled via temperature or timing. The heaters may turn on simultaneously or cycled with periods independent of each other. The heater's power density can also be modified. The user can specify any number of layers and thicknesses depth-wise into the airfoil. LEWICE has maximum flexibility and possesses the ability to model virtually any electro-thermal heater configuration.

Ice accretion shapes for cylinders and multi-element airfoils have been calculated using LEWICE. The calculated results have been compared to experimental ice accretion shapes obtained both in flight and in the Icing Research Tunnel at NASA Glenn Research Center. The results of this comparison with the experimental databased is described in a recent contractor report [36].

2.1.2. Blade Properties

The conducted research for the wind turbine needs to have an airfoil that has representative properties. Therefore, the DU 93-W-210 airfoil was selected for modeling and experimental procedures. The airfoil at the tip of the rotor blade has a 28.5 in (72.4 cm) chord with a span of 12 inches (30.48 cm). The DU 93-W-210 airfoil with the carrier blade amounts to a 55 in (139.7 cm) total span to the rotation axis. The physical properties of the representative test blade are illustrated in Figure 19. Peter Blasco at the Pennsylvania State University initially used these airfoils for performance testing [42]. A photograph of the test blade in the Adverse Environment Rotor Test Stand (AERTS) facility is shown in Figure 20. The leading edge of the heating elements are protected by an erosion tape with thermistors underneath. The span width of the heaters is slightly oversized in efforts to prevent ice bridging.

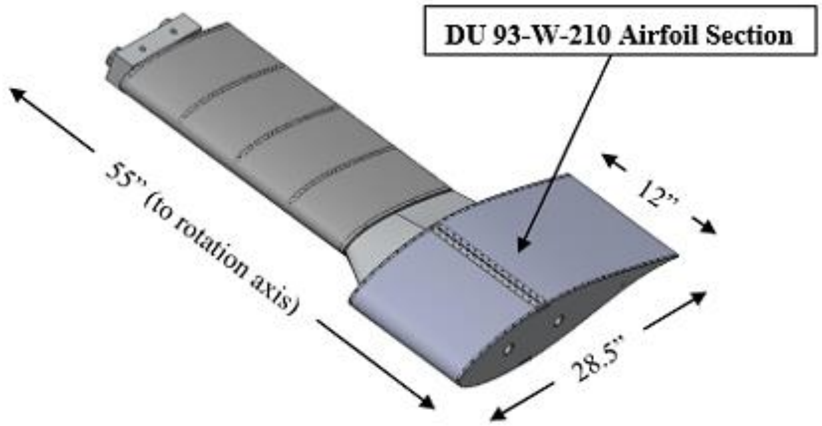

Figure 19: Representative rotor test blade.

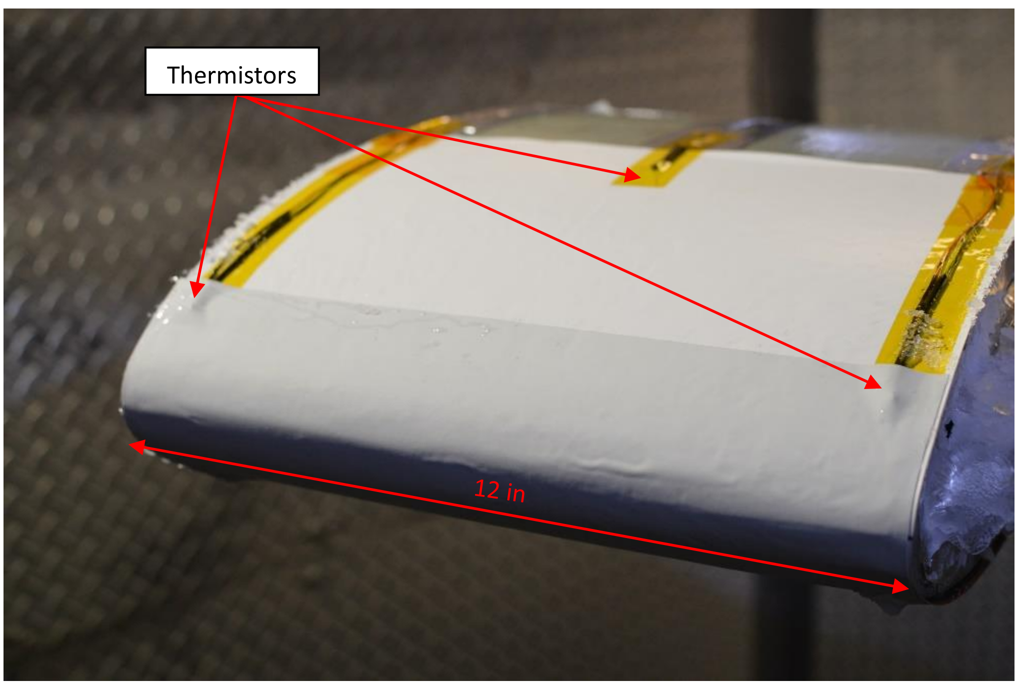

Figure 20: Photograph of the rotor test blade in AERTS facility.

Electro-thermal ice protection systems are the most common IPSs used due to their capability for retrofitting and robustness. It sends electrical current to resistive circuits, which convert electrical energy into thermal energy. There resistive circuits are known as the heating elements. These heating elements are typically adhered underneath the blade skin and coverlay.

Coverlay is a material laminated to insulate the copper conductor. The blade skin is the layer of protection used to prevent surface erosion. The thermal energy converted form electrical energy in the heating elements travel through the layers via conduction. A simplified schematic of the layers is presented in Figure 21.

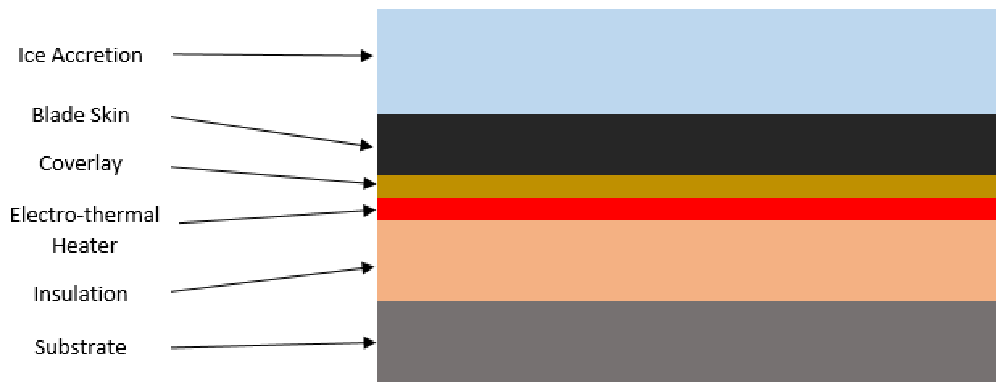

Figure 21: Simplified schematic of layers for an electro-thermal IPS.

The power availability for the ice protection system on the full-scale wind turbine is 100kW. The requested voltage for the system is 480V, which corresponds to a 339.4 root mean squared (rms) voltage. The wind turbine consists of 3 blades, each with a 45 meter radius. The 4 span-wise heater sections were chosen to begin at the 26.7% span location (12m from the root of the rotor blade). The chord coverage (CC) of each heater section is 1 meter. Therefore, each heater zone coverage for all three rotor blades was calculated using Equation (2).

$$Zone\ Coverage = \frac{(1 - 0.267) * Radius * CC}{\#\ of\ Zones} * 3 \tag{2}$$

The maximum available power density for each heater zone is calculated using the total available power (100kW) and the zone coverage calculated in Equation (2). Equation (3) displays how the maximum available power density for each heater zone was quantified.

$$Max\ Power\ Density = \frac{100\ kW}{Zone\ Coverage} \tag{3}$$

For the anti-icing configuration, each rotor blade is equipped with three heaters; the strip heater and the two auxiliary heaters. The strip heater is located on the leading edge of the airfoil, protecting 5.4% of the airfoil in the wrap direction, and provides the highest power density. The auxiliary heaters are behind the strip heater, in the aft direction, on the upper and lower side of the airfoil. The heaters are slightly overlapped to ensure continuous heater coverage on the leading edge. The width of the entire heater configuration covers approximately 25% of the airfoil in the wrap direction. A schematic of the anti-icing heater configuration is shown in Figure 22.

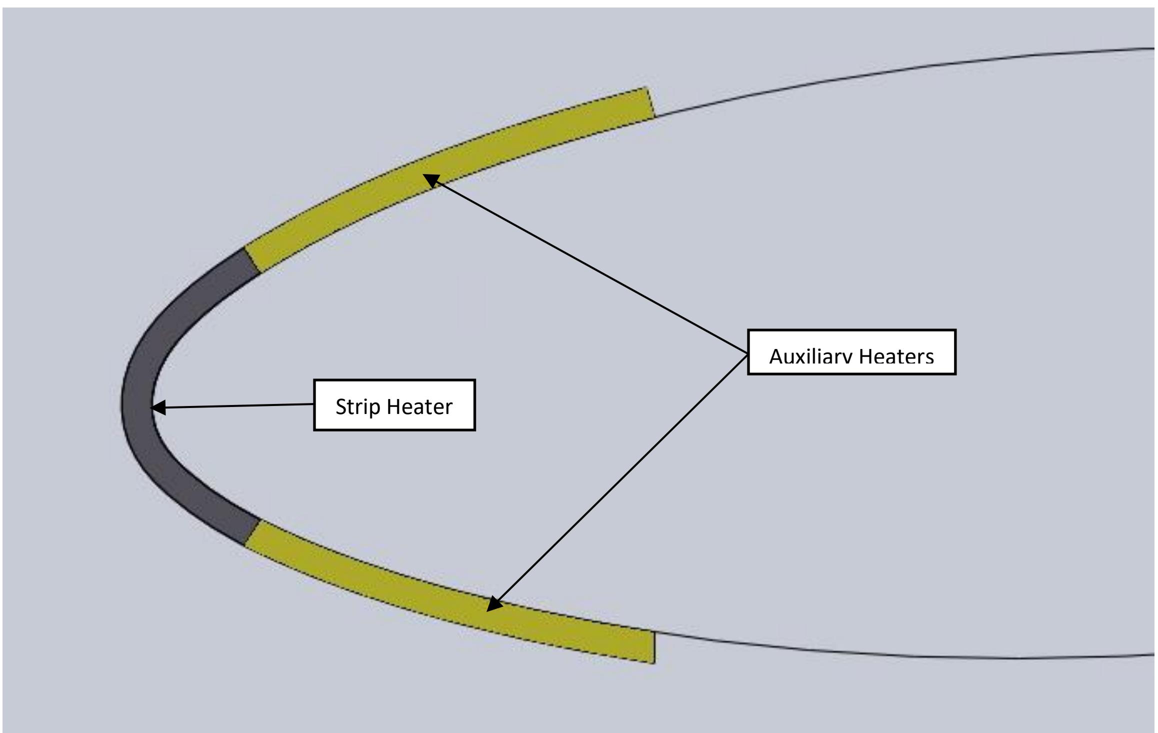

Figure 22: Schematic of Strip and Auxiliary heater configuration.

2.1.3. Main Input File

LEWICE will read in a main input file that is supplied by the user. The main input file is divided into four name-list sections: &LEW20, &DIST, &ICE1, and &LPRNT.

The first section, &LEW20, contains a collection of inputs and should immediately follow the title line. First, ITIMFL is a flag indicating whether LEWICE will use automatic time stepping calculated by the accumulation parameter or a user-defined number of time steps. TSTOP is the ending time of the icing simulation in seconds. IBOD is the number of bodies to be simulated. IFLO is the number of time steps to be used during the simulation. This variable is automatically calculated if the ITIMFL flag contains automatic time stepping. DSMN is the minimum size of the control volume (non-dimensionalized). Larger values of DSMN create fewer control volumes and few panels, while smaller DSMN values create more control volumes and panels. The default value for DSMN is 0.0004. NPL is the number of particle trajectories that define the collection efficiency distribution. LEWICE needs at least 10 trajectories to calculate an accurate collection efficiency curve. The default value for NPL is 24. RHOP is the density of the water particle in kg/m^3 and the default value is 1000. SLD is a flag that activates physical models and correlations for super-cooled droplets. If SLD equals 1, the program allows the droplets to break up prior to impact and splash upon impact. IGRID is a flag that allows a grid solution to be used in place of the potential flow solver. IF IGRID equals zero, the off-body air velocities are determined directly from the potential flow solver. IDEICE is a flag that controls which de-icer model will be utilized. IDEICE can have values from 0 to 4. Zero indicates that a de-icing routine will not run. One activates a 1D stead state anti-icer. Two will perform the analysis using the standard heat transfer coefficient assuming an ice roughened surface. Three will use laminar heat transfer coefficient, which assumes a clean surface. This flag value is recommended for anti-icing simulations that create a small ice shape [35].

The second section, &DIST, defines the particle size and distribution. The first variable, FLWC, is the volume fraction of the total liquid water content contained in each droplet. The sum of the FLWC values must equal one. DPD is the size of the water droplets in microns. If only one input is entered, then that value represents the MVD [35].

The third section, &ICE1, provides the meteorological and flight conditions of the icing simulation. The first variable is the CHORD, which is the distance, in meters, from the leading edge to the trailing edge. For cylinders, it would be the cross-sectional diameter. AOA is the angle of the attack, which represents the angle of the body with respect to the incoming flow in degrees. VINF represents the ambient velocity (flight speed) in meters per second. The next variable, LWC, is the liquid water content of the air (icing cloud) in g/m^3. TINF is the ambient static temperature in degrees Kelvin and PINF is the ambient static pressure in Pascals (N/m^2). The last input variable for this section is RH, which denotes the percentage of relative humidity. This value is usually assumed to be 100% in an icing cloud [35].

The final section in the main input file is the &LPRNT. This section controls output file print options. The user can control the amount of output information for each icing simulation. Output files can entail flow solution, heat transfer coefficients, collection efficiencies, energy balance, mass balance, droplet trajectories and debugging information [35]. An example of the main input file generated for a LEWICE simulation is shown in Figure 23.

```
Matlab Auto-Generated LEWICE Input
&LEW20
ITIMFL =1
TSTOP = 600
IBOD =  1
IFLO =  1
DSMN = 0.00040
NPL = 30
RHOP = 1000.9
SLD = 0
IGRID = 0
IDEICE = 3
&END

&DIST
FLWC = 1.00
DPD = 20.00
&END

&ICE1
CHORD = 0.7239
AOA = 0.000
VINF = 52.000
LWC = 0.40
TINF = 265.15
PINF = 99781.00
RH = 100
&END

&LPRNT
FPRT = 1
HPRT = 1
BPRT = 1
EPRT = 1
MPRT = 1
TPRT = 0
IDBF = 1
&END

&RDATA
&END

&BOOT
&END
```

Figure 23: Example of a LEWICE main input file for simulation.

2.1.4. De-Icer Input File

LEWICE will read in a de-icer input file that is supplied by the user. The input file can be unformatted or contain comments to improve readability. The de-icer file is divided in five sections: description of the de-icer geometry and physical properties, heater power and cycle classification, description of boundary conditions, definition of various flags for certain features, and description of input/output/saving options.

The first line of the de-icer input identifies the total number of layers in the normal direction and the total number of heater sections in the wrap direction. Each layer must be defined by the number of points in the normal direction for each layer, thickness (m), thermal conductivity (W/mK) at 0°C in the normal direction, thermal diffusivity (W/mK^2), anisotropy ratio, and the slope of the thermal conductivity with temperature (W/mK^2). The number of points defines the grid spacing in the normal direction for that layer. The first layer is the innermost layer and the last layer will be the top surface. The thermal conductivity of a layer in the normal direction is defined as a function of temperature, shown in Equation (4). Where k_{ref} is the thermal conductivity (W/mK) at the reference temperature, 0°C, and m is the slope of the temperature dependence (W/mK^2).

$$k = k_{ref} + m\left(T - T_{ref}\right) \tag{4}$$

The user also inputs an anisotropy ratio, which is the ratio of thermal conductivity in the wrap direction to thermal conductivity in the normal direction. Most materials will have an anisotropy ratio of 1, which means the anisotropy ratio is constant and the variation of conductivity with temperature is the same in the wrap and normal direction. The thermal diffusivity must be identified by the user. The equation that defines thermal diffusivity (α) is shown in Equation (5), where k is the thermal conductivity (W/mK), ρ is the density (kg/m^3) and C_p is the specific heat (J/kgK).

$$\alpha = \frac{k}{\rho * C_p} \tag{5}$$

A sample data of the layer properties for the de-icer input file are presented in Figure 24. An example of the de-icer input section for the heater layer is displayed in Figure 25. The thermal properties identified here will be used only in the heater layer of an electro-thermal system. These layer and heater properties are an example from the LEWICE manual [35].

```
C
C     Data for each layer: C
C     nodes = # of points in that layer or section
C     length = length (thickness) of layer or section
C
 # of   length   conductivity  diffusivity  anisotropy  slope (b) of
 nodes   (m)       (W/m/K)       (m^2/s)      factor     temp. eqn.
"node"  "elde"      "ak"          "alp"        "al"       "slope"
C     substrate
 15    3.430d-3    0.120d0      1.652d-7      1.d0       0.d0
C     insulation
 08    8.900d-4    0.294d0      1.045d-7      1.d0       0.d0
C     insulation
 18    2.800d-4    0.256d0      1.473d-7      1.d0       0.d0
C     heater
 07    1.300d-5   41.000d0      1.194d-5      1.d0       0.d0
C     insulation
 18    2.800d-4    0.256d0      1.473d-7      1.d0       0.d0
C     abrasion shield
 08    2.030d-4   16.270d0      4.035d-6      1.d0       0.d0
C     ice
 21    2.540d-3    2.232d0      1.151d-6      1.d0       0.d0
```

Figure 24: Example of a LEWICE de-icer input file identifying layers [35].

```
C
C      Data for each heater/gap section:
C
 # of   length    cond.     diff.  anisotropy  slope(b) of     add.     layer
 nodes    (m)     (W/m/K)   (m^2/s) of heater  temp. eqn.  length (m)  number
C      gap (no heat input)
 10     0.9144d0  0.256d0  1.637d-7    1.d0       0.d0        0.d0        3
C      heater G
 14     3.175d-2  41.000d0  1.194d-5   1.d0       0.d0        0.d0        3
C      heater E
 21     2.540d-2  41.000d0  1.194d-5   1.d0       0.d0        0.d0        3
C      heater C
 21     2.540d-2  41.000d0  1.194d-5   1.d0       0.d0        0.d0        3
C      parting strip - heater A
 36     1.905d-2  41.000d0  1.194d-5   1.d0       0.d0        0.d0        3
C      heater B
 21     2.540d-2  41.000d0  1.194d-5   1.d0       0.d0        0.d0        3
C      heater D
 21     2.540d-2  41.000d0  1.194d-5   1.d0       0.d0        0.d0        3
C      heater F
 14     3.175d-2 41.000d0  1.194d-5   1.d0        0.d0        0.d0        3
C      gap (no heat input)
 10     0.9144d0  0.256d0  1.637d-7   1.d0        0.d0        0.d0        3
```

Figure 25: Example of a LEWICE de-icer input file identifying sections [35].

The next section of input data describes the heater power and cycle times. There are two types of heater modes: time control or temperature control. The initial heater mode specifies heater power wattages and the ON/OFF cycle times. The latter heater mode utilizes temperature to control the cycling of the heaters. An example of each type of heater cycle is shown in Figure 26 [35].

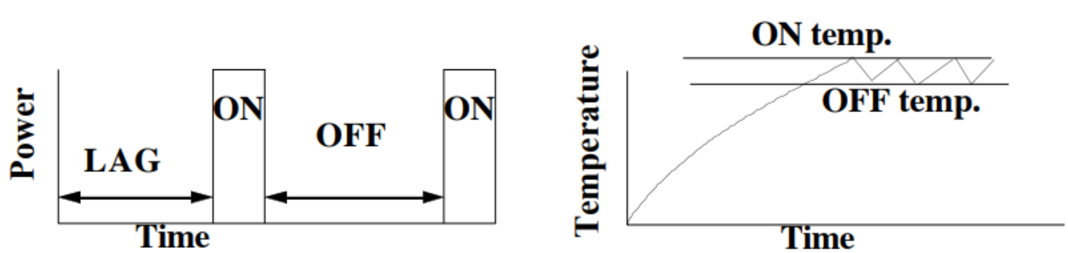

Figure 26: Two heater modes: time control (left) and temperature control (right) [35].

The first line of this heater section contains three variables: the layer number for an electro-thermal heater (IJDE), the offset for the parting strip heater (OFFSET) and the number of parameter studies (IPAR). The OFFSET variable contains the distance, in meters, of the center computational domain from the leading edge. If OFFSET equals zero, the midpoint of the de-icer sections will be aligned with the midpoint of the airfoil in the wrap direction. A negative value will shift the sections towards the bottom of the leading edge, and positive values will shift the sections towards the top of the airfoil [35].

The next lines of data encompass the heater power and cycle times. The user must input data for each section, even if there is no heat generation in that section. Each line contains the heater power (kW/m^2), heater ON time (sec), heater OFF time (sec), heater lag time (sec), and the flag denoting if the user is applying time or temperature heater modes. If the flag equals zero, it represents the time control heater mode. If the flag is greater than zero, then it represents the layer number used to control the heater cycle via temperature. This process for each heater mode continues until the simulation stoppage time reached. An example of the de-icer input file from the LEWICE manual for this section is exhibited in Figure 27 [35].

```
C
ijde  offset ipar
004   0.005   1
      “QDE”         “TON”       “TOFF”       “TLAG”      “ICFLAG”
 heater density  time on     time off    lag time  temp cntrl.
 (kWatts/m^2)     (sec)       (sec)       (sec)    flag
C     gap (no heat input)
      0.0d0          0.d0        0.d0         0.d0      0
C     heater G
     12.02d0         5.d0      115.d0       115.d0      0
C     heater E
     11.19d0         5.d0      115.d0       115.d0      0
C     heater C
     11.25d0         5.d0      115.d0       110.d0      0
C     parting strip (heater A) does not turn off
     07.78d0       150.d0        0.d0         0.d0      0
C     heater B
     11.68d0         5.d0      115.d0       110.d0      0
C     heater D
     11.27d0         5.d0      115.d0       115.d0      0
C     heater F
     11.75d0         5.d0      115.d0       115.d0      0
```

Figure 27: Example of a LEWICE de-icer input file identifying heater details [35].

The de-icer input file encompasses many variables that dictate the boundary conditions, ambient temperatures, heat transfer coefficients, heat flux boundaries, bleed-air heating, mass flow rate, conduction during lag time, initial temperature profile, shedding behavior, wet or evaporative mode, and saving characteristics. Due to extensive de-icer input data, only the first two sections of the de-icer file are covered in this paper.

2.1.5. MATLAB Batch Code

Modeling efforts were driven by the ability to mass produce results. Development of a batch code in MATLAB delivered that capability. The user must create .txt files with the variable values for each test case. These quantitative parameters could be temperature, flight speed, LWC, MVD, icing simulation time, heater power density or heater cycle times. The program loads that file and auto-creates the main input file for LEWICE, after deleting the previous test case file. It will perform a similar action for the de-icer input file containing the heater configuration. The code implements the new parameters and utilizes the LEWICE batch file to open the software. It automatically inputs the airfoil geometry and runs the icing simulation. When the simulation is completed, MATLAB locates and saves certain output files of interest. It will load, read, graph and save the output files the user desires. After completing the process, it deletes the input and output files and loads the new test case parameters. This process repeats until all test cases are completed and saved. This code delivered the capability to mass produce modeling results and perform trades studies.

2.1.6. Anti-Icing Test Matrix

Modeling and testing were conducted throughout this research. A test matrix was selected to compare modeling results with experimental data. The objective of this test matrix was to find quantitative power densities that effectively prevent ice accretion on the airfoil. From a conservative view, the heater configuration would be successful at less severe icing conditions if proven effective at the severe icing condition (large LWC – large MVD). It must be noted that wind turbines, since placed on the ground, do not see the low temperatures that a flying vehicle could encounter in flight, as summarized by the FAR Appendix C icing envelopes. Operators indicate that the lower temperatures they observed is -8°C, with the worst ice accretion effects on power generation occurring at approximately -4°C. Therefore, each test case was conducted at -8°C with a 0.9 g/m^3 LWC and 35 µm MVD combination (coldest temperature expected, requiring maximum power densities). As stated earlier in Chapter 1, the higher LWC – MVD combinations prove to be more severe at lower temperatures [22]. The parameters for this test matrix are shown in Table 1. The results comparing experimental data are presented in Chapter 4 of this paper.

Table 1: Anti-Icing Modeling Test Matrix

Test Case	Power Density Strip (W/cm^2)	Power Density Auxiliary (W/cm^2)	Icing Time (mins)	Temperature (°C)	LWC (g/m^3)	MVD (µm)	Flow Velocity (m/s)
1	0.3	0.09	3	-8	0.9	35	52
2	0.43	0.13	3				
3	0.43	0.18	3				
4	0.56	0.18	3				
5	0.42	0.23	3				
6	0.42	0.37	3				
7	0.58	0.37	3				
8	0.58	0.37	5				
9	0.58	0.37	10				

Chapter 3: Testing Facility and Experiment Configuration

The Pennsylvania State University's Adverse Environment Rotor Test Stand (AERTS) facility was used to acquire experimental data for the goals and objectives stated in Chapter 1. This chapter discusses the facility's capabilities, as well as an Arduino and LABVIEW interface developed to control and monitor the ice protection system. The sensors and equipment utilized for these experiments are explained in detail.

3.1. Adverse Environment Rotor Test Stand

3.1.1. Facility Overview

The AERTS testing facility was designed and constructed at the Vertical Lift Research Center of Excellence (VLRCOE) at The Pennsylvania State University [37]. AERTS is a state-of-the-art facility utilized to test truncated wind turbine blades, propellers and helicopter blades. The facility also conducts extensive ice adhesion strength testing for various ice protective coatings. The rotor stand is enclosed by a 6m x 6m x 3.5m ballistic wall for safety purposes. A general schematic of the industrial walk-in cold chamber is shown in Figure 28.

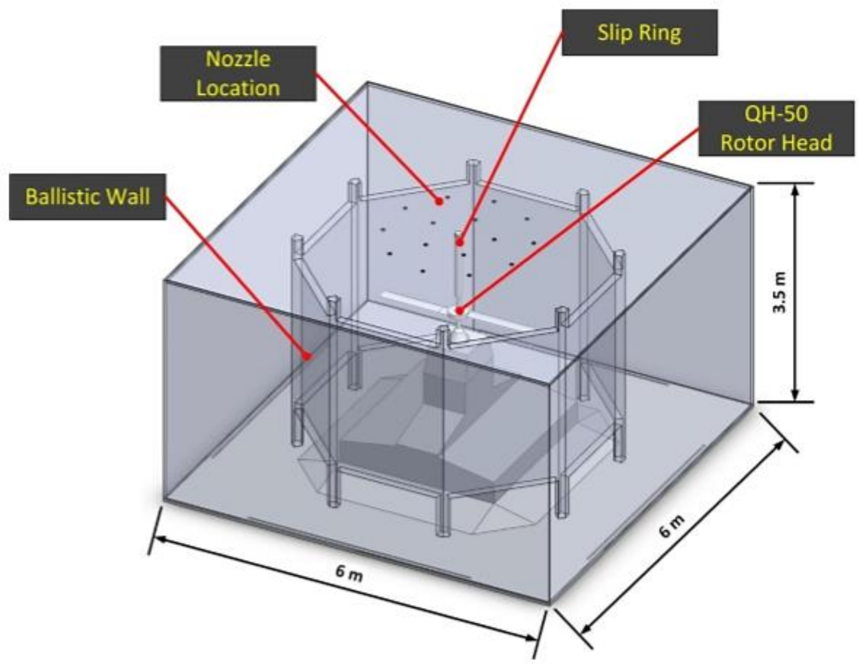

Figure 28: Schematic of AERTS facility chamber [37].

The chamber is cooled by a 10 HP, water-cooled cooling system with controllable temperatures between -25°C and 0°C. The rotor stand has a 125 HP motor, which can achieve RPMs from 200 to 1600. The rotor hub is from a QH-50D DASH Unmanned Helicopter that was donated by Gyrodyne Helicopter Historical Foundation. The QH-50D is a co-axial UAV designed for the Navy in the early 1950's [37]. The hub was modified to have linear actuators that control the collective and lateral pitch. A 6-axis load cell was installed in the bell housing of the hub to monitor the forces and moments during experiments. A built-in torque sensor above the driving shaft monitors the torque provided by the 125 HP motor. Four slip-rings carry 48 signal channels and 24 power channels from the fixed frame (control room) to the rotating frame (rotor blades). The ceiling of the chamber, above the rotor stand, has two concentric rings of NASA standard atomizing nozzles. The inner ring holds 5 nozzles, while the outer ring has 10 nozzles. The rotor stand equipped with NACA 0012 blades is exhibited in Figure 29.

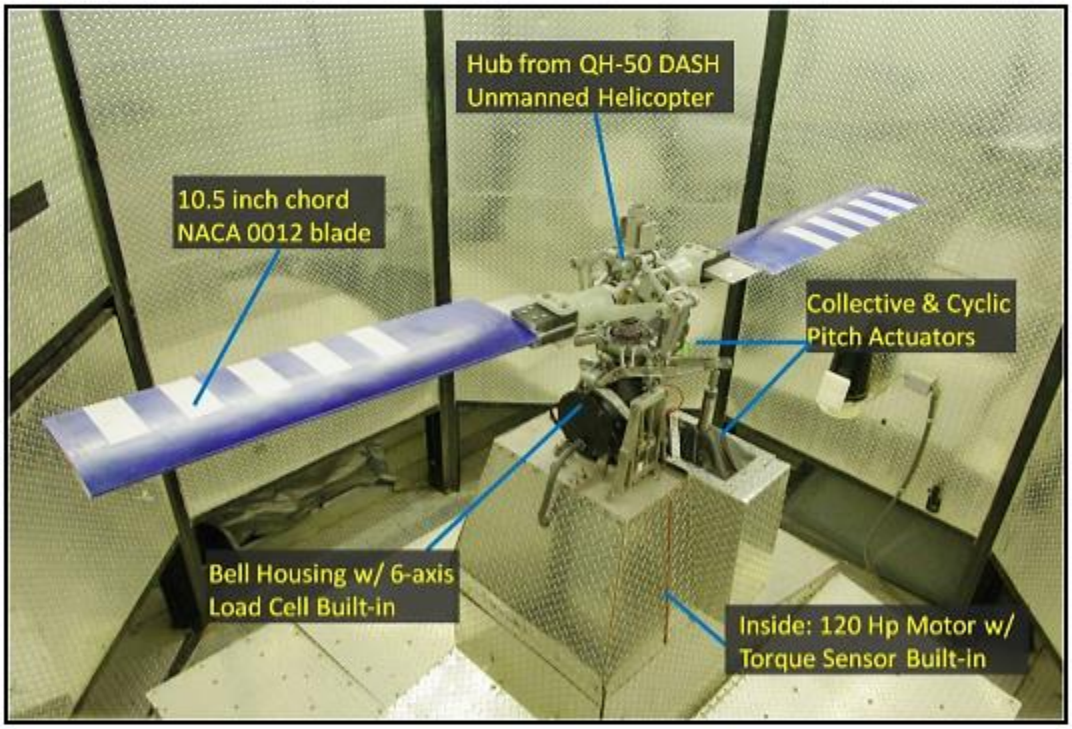

Figure 29: Photograph of AERTS rotor stand with NACA 0012 blades [18].

The chamber can accommodate rotor test blades with a maximum diameter of 2.743 m (9 ft). Depending on the experiment objective, the blades can be modified to carry a "paddle" tip section. Figure 30 displays the rotor stand equipped with NACA 0012 paddle blades. A photograph of the DU 93-W-210 paddles section is exhibited in Figure 31. The airfoils were covered in fiberglass to represent the thermal conductivity on the wind turbine. The maximum chord for the paddle section is 0.813 m (32 in.) due to flow interactions from the ballistic wall and floor. The minimum distance between the tip of the rotor blade and the ballistic wall is approximately 18 inches and the ice shapes are taken at 95% of the blade radius. The downwash flow can be affected by the floor, which can reduce the mass flow rate through the rotor disk and alter flow patterns. Experiments were performed at NASA Langley Research Center that showed approximately 50% of the ground effect is dependent on the fuselage shape [38]. The ground has "virtually the same effect" on hover performance when H/D ranges between 0.43 and 1.4, where H denotes test model distance to the ground and D is the disk diameter. The H/D ratio for the AERTS facility is approximately 0.78. The ground effect is considered a secondary issue at low thrust conditions (30 lbf) in the AERTS testing facility and a minimal issue once ice accretion starts.

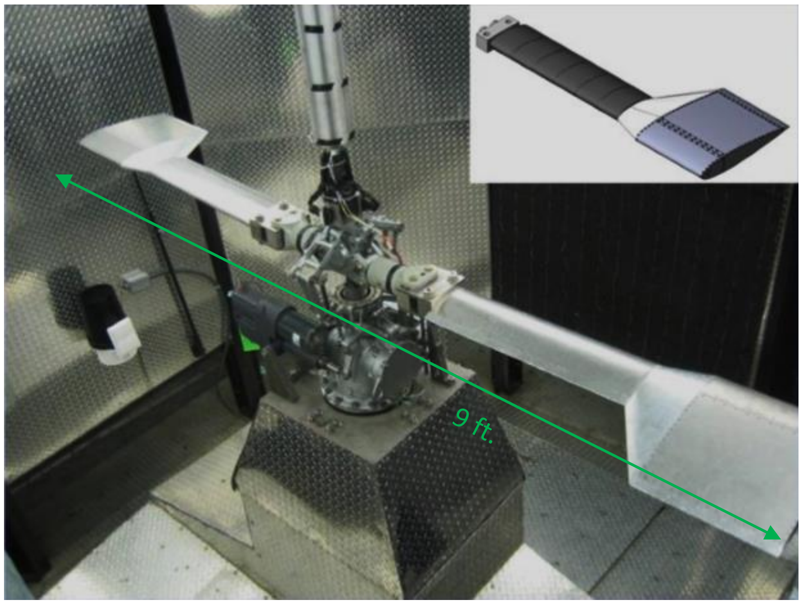

Figure 30: Photograph of AERTS equipped with paddle test sections [40,43].

Figure 31: Photograph of DU 93-W-210 paddle blade section.

3.1.2. Nozzle Spray System

The AERTS facility produces an icing cloud with a total of 15 NASA standard nozzles. These nozzles were donated by NASA IRT are configured in two concentric rings on the chamber ceiling. The inner ring holds five nozzles and the outer ring holds ten. A nozzle control system manipulating air and water pressure that controls the water droplet MVD. This creates the ability to produce various icing cloud combinations with certain values of LWC and MVD. A photograph of the nozzle spray system in AERTS is shown in Figure 32.

Figure 32: Nozzle spray system in AERTS facility [29].

Achievable LWC values range from 0.2 g/m^3 to 5.0 g/m^3 with MVD values between 10 μm and 50 μm. The nozzles operate by aerosolizing water droplets with a precise combination of water and air pressure. The water and air pressure differential create a water droplet with the appropriate MVD, generating an icing cloud according to the calibration chart. The NASA standard icing nozzle calibration chart is shown in Figure 33. The test temperature, MVD and air pressure are controlled by operating an in-house LabVIEW code. LabVIEW, Laboratory Virtual Instrument Engineering Workbench, is a graphical object-oriented programming (GOOP) language commonly used for data acquisition and instrument control. The front panel interface of the LabVIEW control system is exhibited in Figure 34.

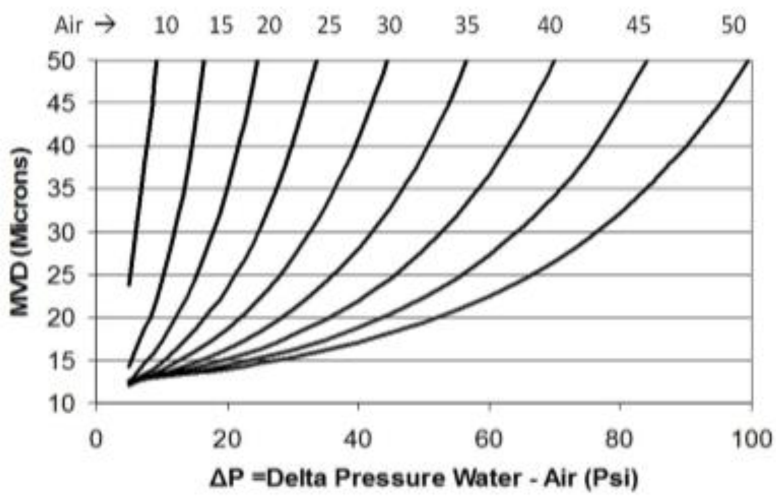

Figure 33: NASA standard icing nozzle operation chart [23].

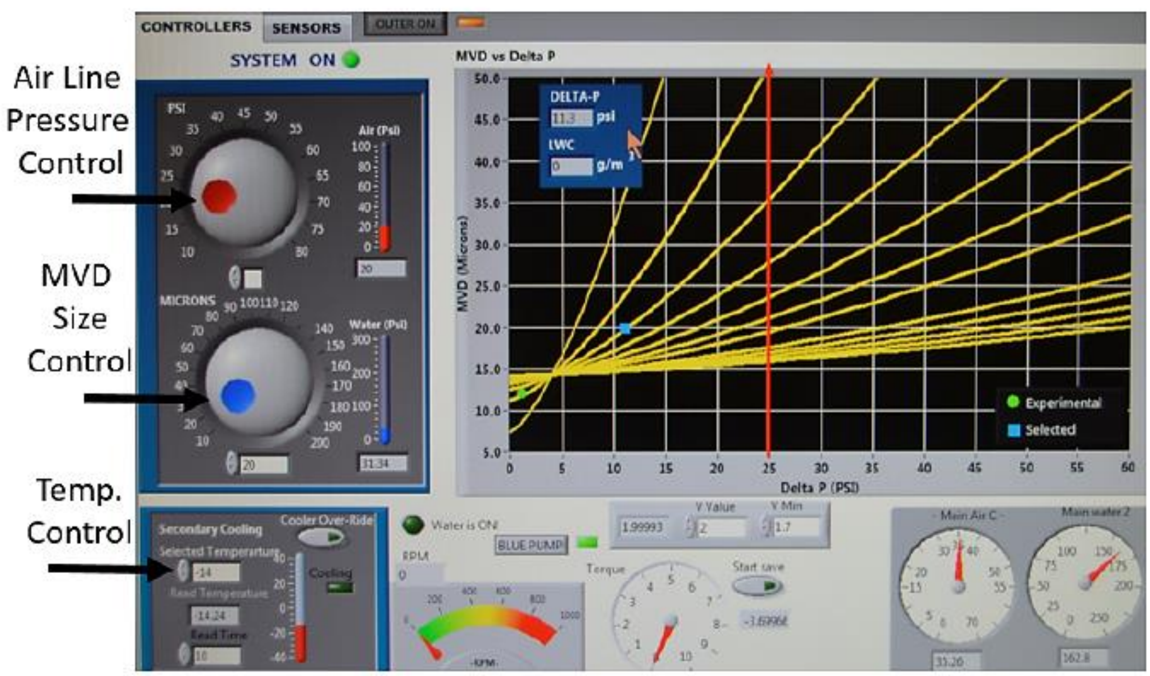

Figure 34: Front panel of LabVIEW code for AERTS icing cloud.

3.1.3. LWC Measurements

LWC is the characteristic water-to-air concentration in a two-phase flow and denoted with units of g/m^3. LWC plays an important role in determining icing conditions for experiments, because it directly affects the ice accretion rate per time. Static LWC sensors are not applicable in the AERTS facility due to operational velocity conditions and the centrifugal forces impairing their ability to accurately measure LWC in the rotating frame [18]. Therefore, the local LWC needs to be determined by experimental measurements.

The LWC is found by measuring ice thickness at the stagnation point of the airfoil. There are certain icing conditions that are favorable for measuring LWC values. As discussed in Chapter 1, glaze ice is produced by warmer temperatures (-4°C) and cause the water droplets to splash and run-back after impact. These effects will decrease the stagnation ice thickness and produce LWC values lower than the true value. At colder temperatures (-20°C), rime ice forms and tightly follows the contour of the body with limited run-back water. Therefore, rime icing conditions are ideal for experimental LWC measurements.

An algorithm was developed by Yiqiang Han at The Pennsylvania State University to calculate the LWC when given temperature, MVD, icing time, impact velocity of water droplets, and the final ice thickness at the stagnation point [18]. The foundation of the algorithm branches from a NASA method used in the Icing Research Tunnel [23]. This process is an iterative scheme that compares experimental ice thickness to a predicted thickness found by varying the freezing fraction. The freezing fraction is defined as the fraction of water flux entering a control volume that freezes within it. In the algorithm, the freezing fraction is altered until the experimental thickness matches the predicted thickness [18]. The drawback regarding this procedure is the icing time parameter. After the nozzle spray system is turned on, it takes about 10 seconds for the cloud to become uniform. Also, after long periods of time the body accretes ice that alters its aerodynamic shape, which will change the collection efficiency. Thus, the LWC calculations will not be representative of the physical cloud. To mitigate these effects, it has been determined that approximately one to two-minute icing times are appropriate for LWC measurements. A flowchart explaining the logic of the algorithm is shown in Figure 35.

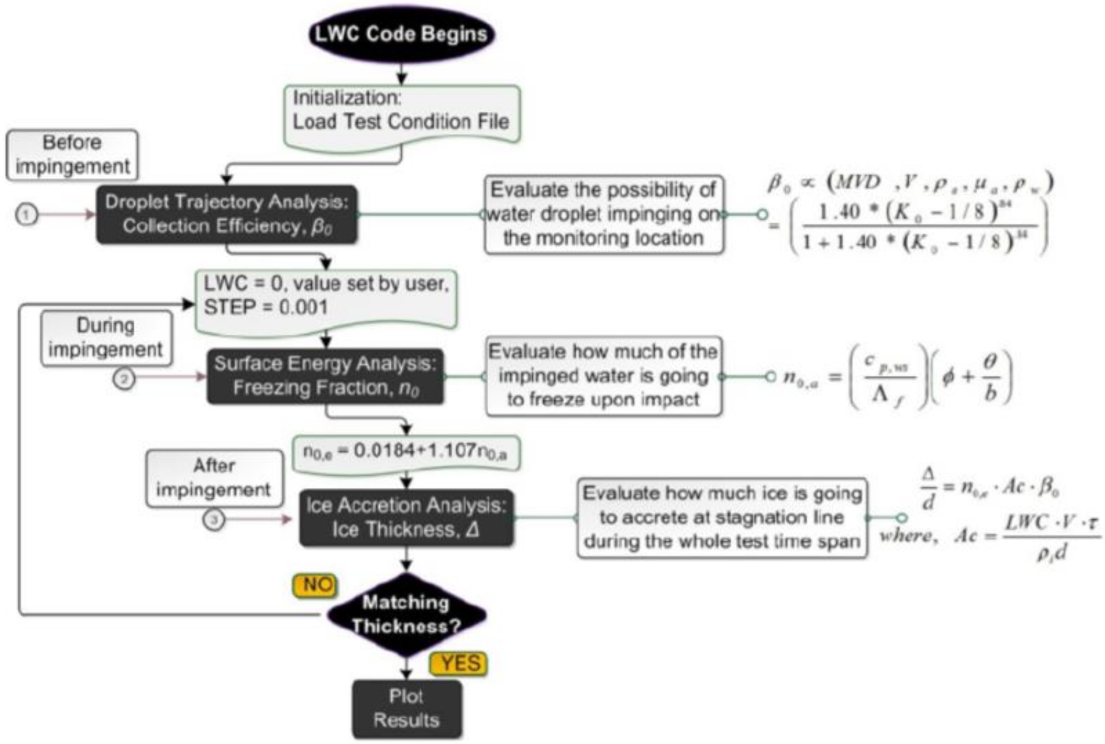

Figure 35: Algorithm flowchart to determine experimental LWC values [18].

To find experimental LWC values for the DU 93-W-210 airfoil, the AERTS icing chamber was cooled to -20°C. The LabVIEW controller was utilized to vary MVD between 20 μm and 35 μm with an airline pressure of 15 psi. The leading-edge radius for this airfoil is approximately 19 mm and the icing duration was two minutes. The impact velocity can be calculated from the measured RPM of the rotor stand. For 400 RPM, the impact velocity is 52 m/s on this blade configuration. The number of nozzles used dictates the ice accretion rate per time. For these experiments, the number of nozzles needed for several icing conditions were determined using Han’s algorithm. The experimental ice thicknesses and LWC values are presented in Figure 36 and

37, respectively. For medium icing conditions, 0.4 LWC was selected and 3 nozzles at 20 MVD represented this icing condition. For severe icing conditions, 0.9 LWC was selected and 4 nozzles at 35 MVD characterized this icing condition.

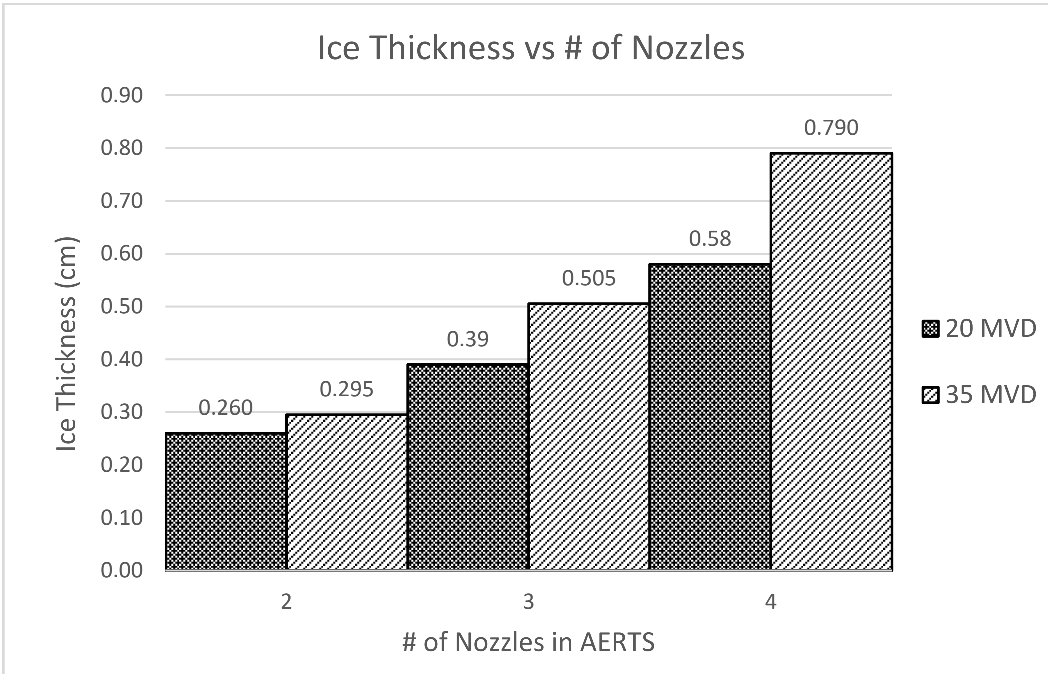

Figure 36: Ice thickness vs # of nozzles in AERTS.

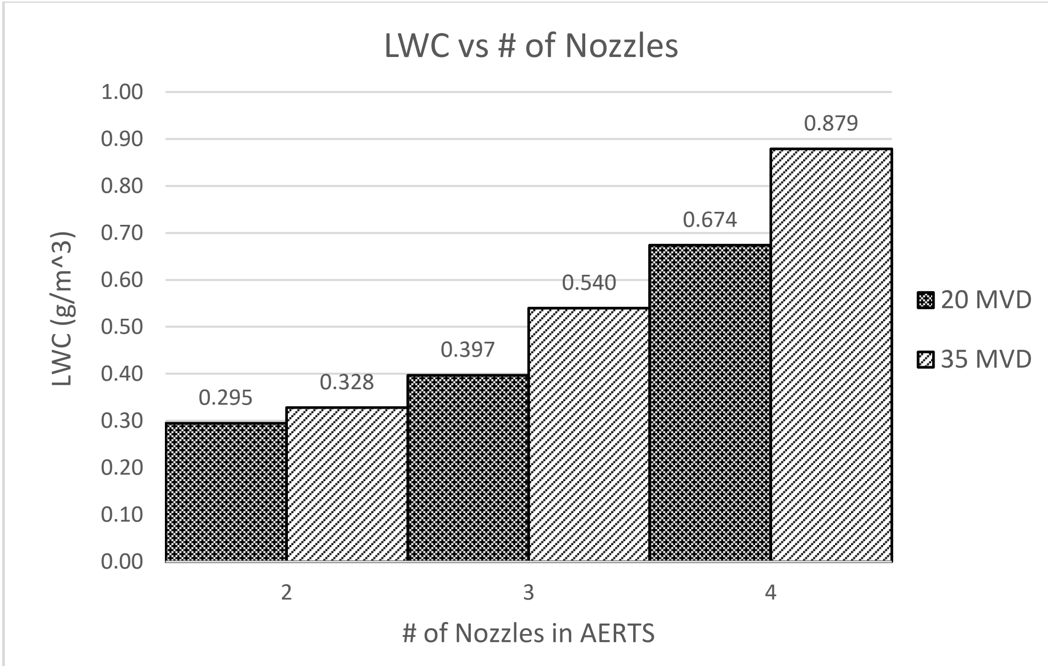

Figure 37: LWC vs # of nozzles in AERTS.

3.2. Experiment Set-Up

3.2.1. Arduino/LABVIEW

The objective of the software system was to control heater ON/OFF timing, measure power densities to various electro-thermal heater zones on the rotor blades and quantify heater temperatures. The code read and saved real-time temperature, torque, current and power density. An Arduino Mega 2560 microcontroller, shown in Figure 38, was used for communication to the LabVIEW interface. The microcontroller is USB programmable with 54 digital and 16 analog input/output pins. The hardware component responsible for timing and iterations to the electro-thermal heaters was the Sunfounder 2 channel DC 5V relay module, shown in Figure 39. A LabVIEW code was developed to allow the user to input what heater sequence was desired. Heater sequence refers to the option or control to select various heater zones at arbitrary time intervals. This heater sequence manipulates the supplied power from the voltage dividers (denoted as variacs) that vary the AC voltage sent to the electro-thermal heaters on the rotor blades (controlled between 0 and 208 VAC). The relay delivered a chosen voltage through the slip-ring to the heaters in the rotating frame. A 20 amp in-line current sensor module, ACS-712, read real-time current. The LabVIEW code calculated power density and displayed both, current and power density, at that specific heater zone. The ACS-712 current sensor utilized is shown in Figure 40. A 3D printed enclosure, exhibited in Figure 41, was designed to protect the electronic hardware and organize the wiring.

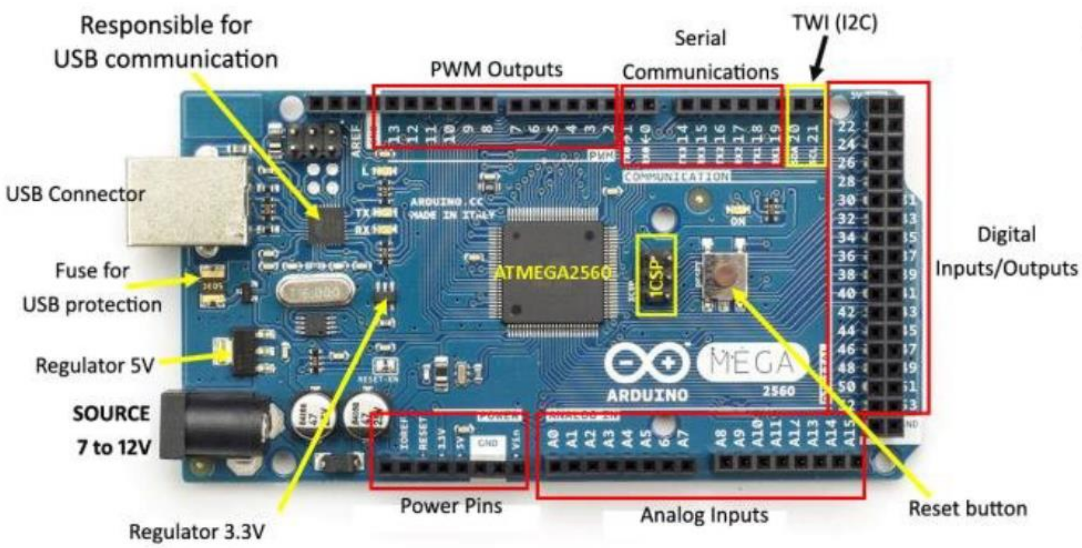

Figure 38: Arduino Mega 2560 microcontroller.

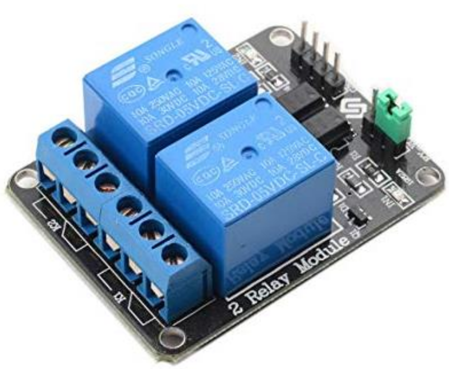

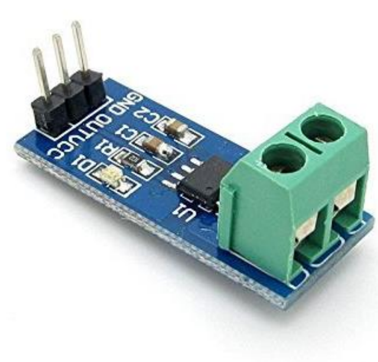

Figure 39: Sunfounder 2 channel relay module.

Figure 40: ACS-712 current sensor.

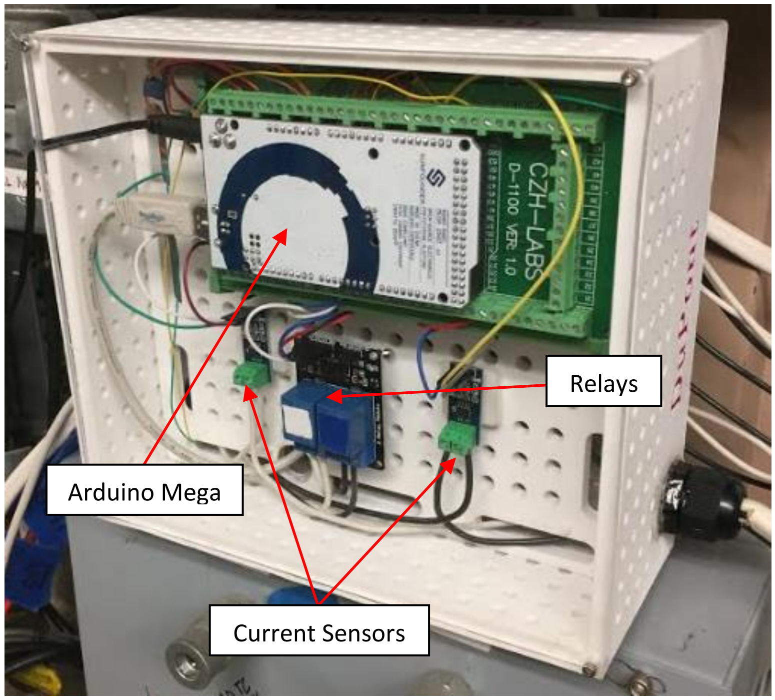

Figure 41: 3D printed enclosure (8.75" x 7.75").

A set of six thermistors on each test blade read the voltage differential through the slip-ring, which measured to the thermal resistance of the sensor. The LabVIEW code calculated the temperature correlation in Celsius. LabVIEW displayed the real-time measurement of temperature for all 12 thermistors on the front panel and saved the data into a .txt file. A schematic was developed on the front panel to denote the location of each thermistor on the leading edge of the airfoil. A photograph of the LabVIEW front panel created for these experiments is presented in Figure 42. Bench tests were conducted in the Vertical Lift Research Center of Excellence (VLRCOE) at The Pennsylvania State University to ensure each component of the system performed successfully. A flowchart outlining the general entities of the experiment is shown in Figure 43, and a photograph of the system during a pre-experiment bench test is exhibited in Figure 44. All data from experiments were saved, processed and analyzed through a post-test MATLAB code.

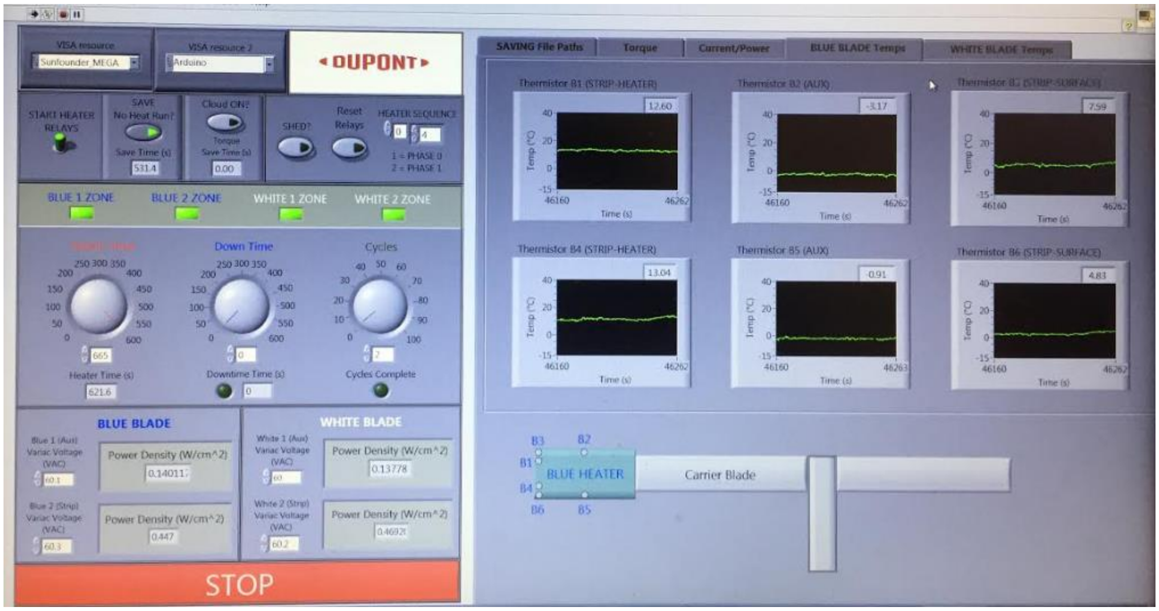

Figure 42: LabVIEW front panel controller/display.

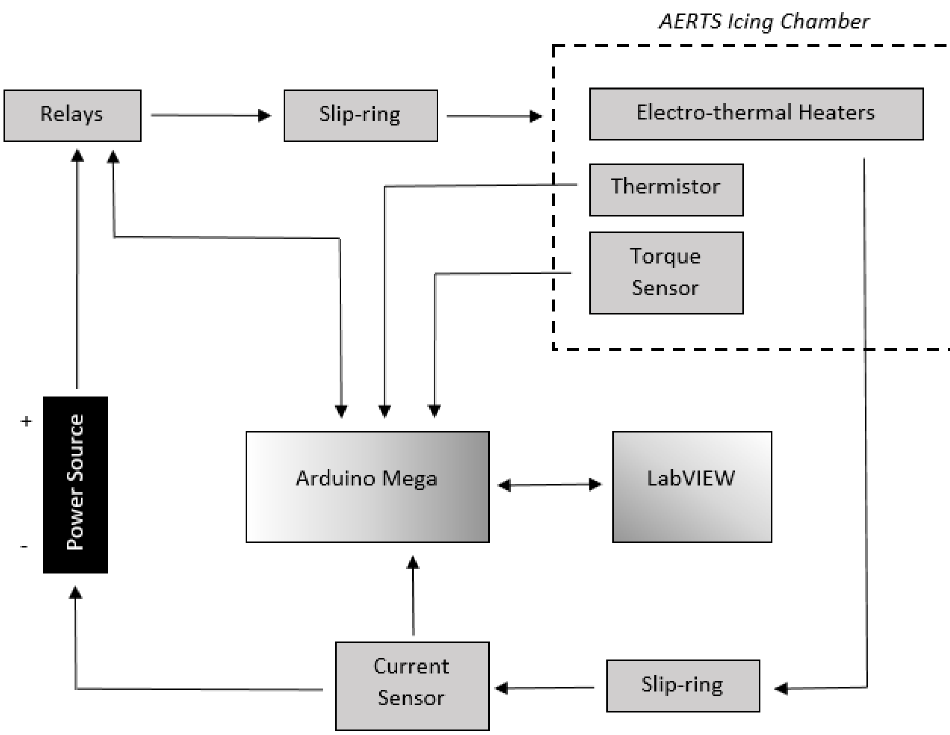

Figure 43: Flowchart of the experiment.

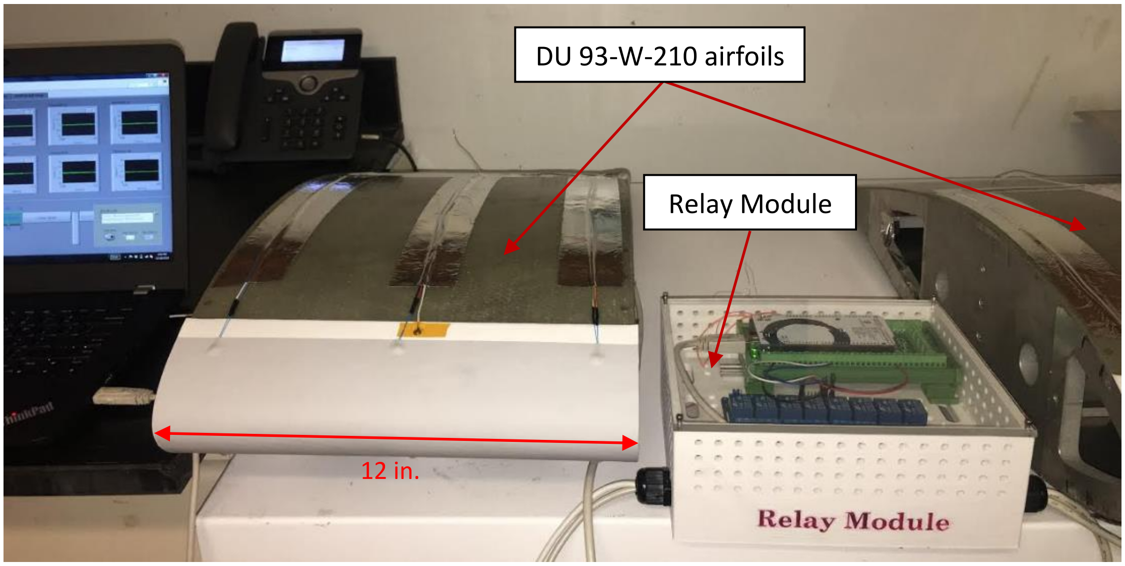

Figure 44: Bench test set-up in VLRCOE.

3.2.2. De-Icing Procedure

Before any test begins, the communication system must be linked. The DB's inside the control room must be connected to the module box to read thermistor data. The voltage variacs are adjusted to desired voltage and wired to the slip-ring in the control room, so the power is delivered to the rotor blades inside the cooling chamber. The torque sensor simply needs an active 12V power supply. Lastly, the USB terminals were joined to the computer allowing Arduino to communicate with the LabVIEW interface.

Once the LabVIEW front panel is updated with the test parameters, the rotor stand spins up to 400 RPM, which represents the water droplet impact velocity (52 m/s) in AERTS facility. The nozzle spray system creating the icing cloud is turned on, then the timer begins and the torque sensor data is graphed and saved. The cloud is shut off and the rotor stand spins down when the icing cloud duration is complete.

To represent the centrifugal forces on the accreted ice, first the ice mass must be known. Photographs of the cross-sectional ice area are taken and utilized to calculate the ice mass on the test section. The density of glazed ice is 0.917 g/cm^3 (917 kg/cm^3), based on experiments at NASA Glenn Icing Research Tunnel [39]. A metal hot plate was used to smoothly cut the feathers off the edge of the test section. Therefore, creating a perpendicular plane against the ice shape for thickness measurements. The photograph encompassing a predetermined scale was digitized using GetData Graph Digitizer. This software calculates the estimated cross-sectional area based on your identified arbitrary scale. An example of this progression is exhibited in Figure 45.

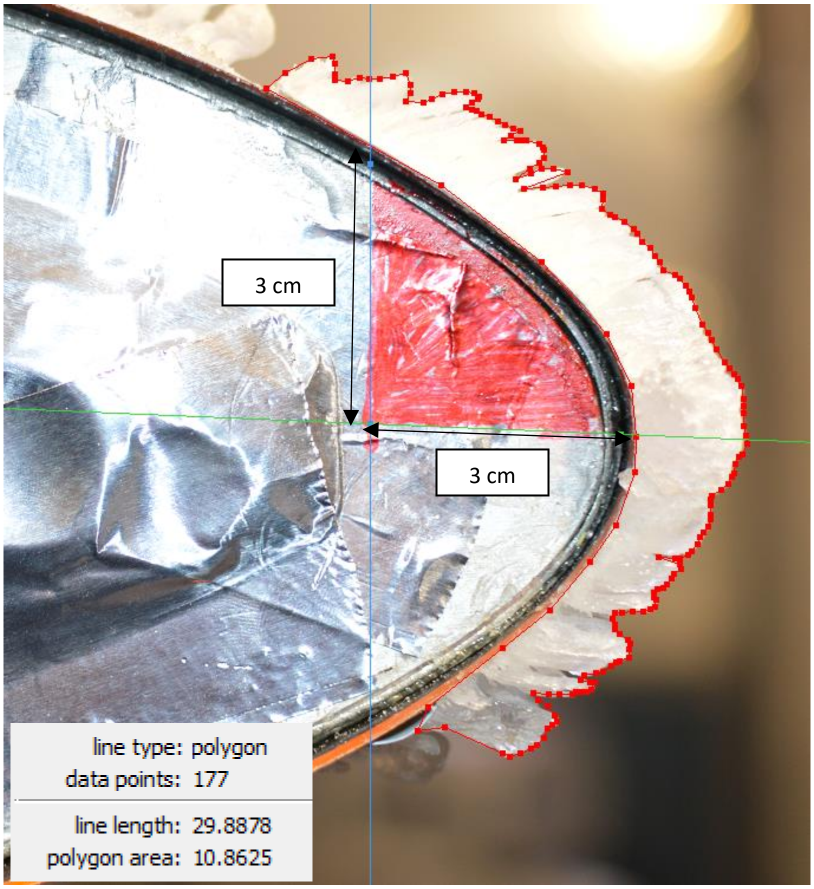

Figure 45: Digitized ice shape at -8°C with 0.4 g/m^3 LWC.

In this picture, the x and y axes (legs of red triangle) are 3 cm in length. The estimated ice area of the polygon is 16.05 cm^2 and the perimeter of the selected 2D ice area is 26.16 cm. Given density and the span of the heater test section (30.48 cm), the estimated ice mass is 448.6 grams. Equations (6) and (7) show how the assumed ice masses were calculated for these experiments.

$$m_{WT} = A_{CS} * L_{WT} * \rho \tag{6}$$

$$m_{AERTS} = A_{CS} * L_{AERTS} * \rho \tag{7}$$

It is important to test the representative centrifugal loading for different locations along the wind turbine blade span. Since the AERTS facility does not have the full-span of a full-scale wind turbine, to reproduce centrifugal forces, higher RPMs in AERTS must be used. The paddle section in the AERTS rotor can therefore represent the centrifugal load at different span locations along the wind turbine when spun at varying RPMs. The wind turbine of interest has a 45 meter radius and operates at 18 RPM (1.885 rad/sec).

The centrifugal forces that would be introduced on a wind turbine were reproduced in the AERTS facility based on the calculations shown below. Then the appropriate rotational velocity parameter for the AERTS facility was obtained. Equations (8-10) summarize the calculation process.

$$CF_{WT} = m_{WT} * \Omega_{WT}^2 * r_{WT} \tag{8}$$

$$CF_{AERTS} = m_{AERTS} * \Omega_{AERTS}^2 * r_{AERTS} \tag{9}$$

$$\Omega_{AERTS} = \sqrt{\frac{CF_{WT}}{m_{AERTS} * r_{AERTS}}} \tag{10}$$

The IPS heater configuration is designed relative to the heater manufacturer requirements and restrictions. Each turbine blade has 4 span-wise heater sections beginning at 26.7% span from the root and ending at 97.7% span. The span percentages used to represent the centrifugal forces were selected at the origin of each heater section. A schematic of the full-scale wind turbine is presented in Figure 46. The selection is done due to cohesive forces between two zones. Such forces must be overcome to promote ice shedding. When the ice accretion exceeds a critical point, the cohesion strength of the ice interface between zones is too large for the centrifugal forces to shed the ice layer, since it would remain attached to the inboard ice shape. Therefore, a minimal ice thickness exists to promote ice shedding (minimum thickness such that centrifugal loads are sufficient to exceed the cohesion strength between zones). Selecting the inner-most span percentage of the heater section is a conservative approach to ensure that the force generated at the inner location is sufficient to overcome cohesive forces. A schematic of the cohesive force opposing the centrifugal force is shown in Figure 47.

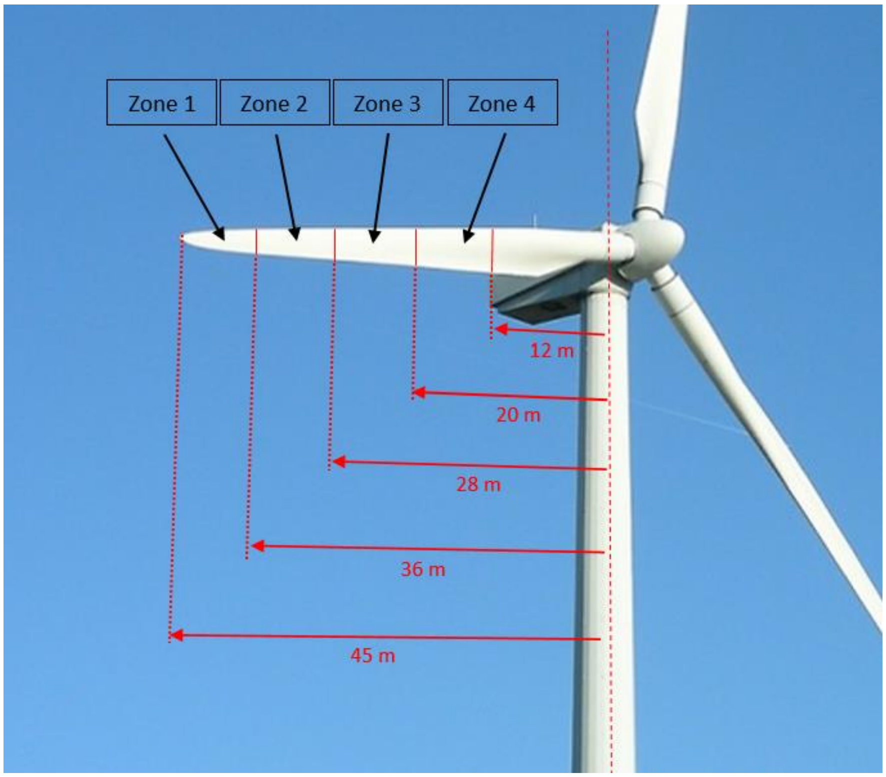

Figure 46: Schematic of full-scale wind turbine.

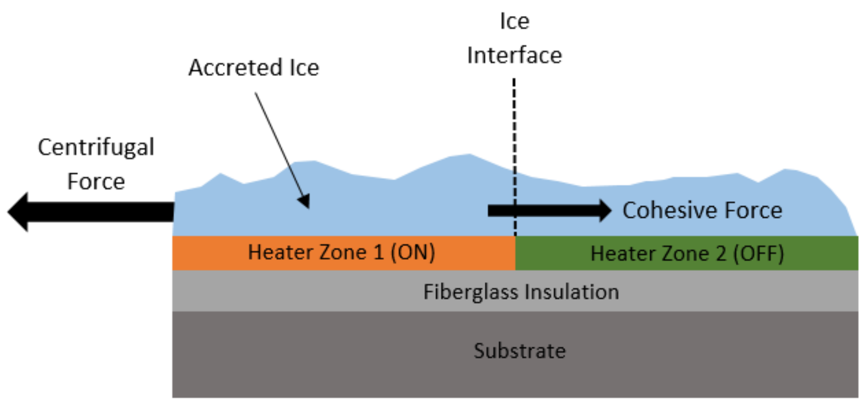

Figure 47: Cohesive force opposing the centrifugal force.

A MATLAB code was developed to calculate the corresponding full-scale RPM in AERTS at any span percentage on the wind turbine. After the test blade accreted ice for a predetermined time interval, a hot plate was used to remove the ice feathers from the tip of the rotor blade. An inch of ice at the tip of the heater section, span-wise, was removed due to the lack of heat production above the copper bus bar in the heating element. A photograph of the ice removal technique utilizing a hot plate is exhibited in Figure 48.

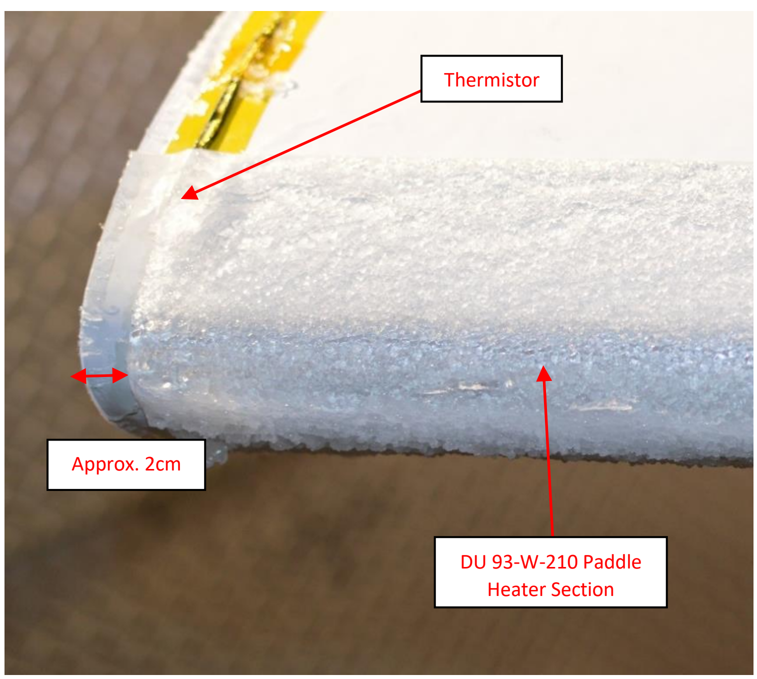

Figure 48: Photograph of the ice removal technique for de-icing experiments.

After the ice mass was photographed and the blades were balanced, the rotor stands was spun up to the RPM that matches with the centrifugal force at the full-scale blade span percentage of interest. When the rotor reaches the desired RPM, the electro-thermal heaters are turned on with the selected power density. The time until the ice sheds on each rotor blade was quantified and recorded. Effective ice shedding was deemed to be less than 30 seconds. After the test was completed and the data was saved, the rotor blades were cleaned and the test parameters are updated in LabVIEW codes (cloud control and heater control) for the next experiment.

3.3. De-Icing Experimental Test Matrix

3.3.1. Linear Ice Accretion

The objective of these tests was to find the ice accretion rate (slope of ice thickness over time) along the span of the blade at three different icing conditions. Data from these experiments play a role in the design of the de-icing time sequence controller. A *Light* icing condition was triggered by a 0.2 g/m^3 LWC and 20 µm MVD at a temperature of -8°C. A *Medium* icing condition consisted of a 0.4 g/m^3 LWC and 20 µm MVD at -8°C. Lastly, a 0.9 g/m^3 LWC and 35 µm MVD combination was selected for the *Severe* icing condition. The nomenclature for the icing conditions are used throughout the de-icing experiments and results.

The RPM established in AERTS during ice accretion must represent the water droplet impact velocity on the wind turbine. For this study, convective cooling plays a major role in the initial stages of ice accretion. A MATLAB code was developed to calculate the RPM correlation in AERTS that represents the impact velocity at a chosen span percentage. After spinning up to the appropriate RPM, the icing cloud was turned on for three different durations: 3, 5 and 7 minutes. The three icing durations would experience the light, medium and severe icing conditions. The key parameters for this set of experiments is shown in Table 2. Unfortunately, 80% span was not tested in the AERTS facility due to the large aerodynamic loads on the rotor stand at such speed. Also, at 67.86 m/s tip speeds (521 RPM), both blades would need to shed simultaneously or the force imbalance would become too large for the rotor stand. Note that the impact velocity is linear with RPM, while the centrifugal loads are square of the RPM. Therefore, once the desired ice shape was accreted, the RPM was varied to match the centrifugal loads of the full-scale span location.

Table 2: Linear ice accretion test matrix parameters.

Span %	Impact Velocity (m/s)	AERTS RPM	Accretion Time (mins)	Temperature (°C)	Icing Conditions
26.7	22.65	174	3, 5, 7	-8	Light Medium Severe
44.4	37.66	289	3, 5, 7		
62.2	52.76	405	3, 5, 7		
80.0	67.86	521	3, 5, 7		

3.3.2. Minimum Ice Thickness for Shedding

It is imperative that the ice mass sheds in a timely manner, before it becomes a hazard to the infrastructure of the wind turbine or the surrounding environment. Also, the allowed accreted ice mass must not produce high aerodynamic performance degradation. Cohesive failure of the ice from zone to zone is required and it was observed during shedding events. When the ice accretion reaches a critical point, the cohesion strength of the ice is exceeded by the centrifugal forces to shed the ice layer. The inner-most span percentage of the heater section, with the least amount of centrifugal force, was selected to ensure cohesive bridging does not occur for a given minimum ice thickness. Since impact velocity mostly affects the ice shape and has small effects on the heat transfer once ice is accreted (ice is an insulator), all test were conducted at an impact velocity of 52 m/s, which correlates to 400 RPM in AERTS. The increase of velocity for inner sections (26.7% and 44.4%) simply means that the accretion rate was increased and does not have any effects on the capability of the heaters to affect the bond-line. It must be noted that the ice shapes could deviate slightly from those accreted at representative span velocities, but ultimately, only the ice mass is of importance for this study.

As previously mentioned, successful shedding events are deemed to be less than 30 seconds. If the ice mass sheds within 30 seconds, the following test case accreted ice for a shorter duration, which decreased the ice thickness and the overall mass (and corresponding centrifugal force). This test method is performed until the minimum ice thickness is found for each heater section (i.e. RPM variation to represent varying span positions) in all icing conditions. Due to power restrictions on the full-scale wind turbine, the maximum power density available was 0.385 W/cm^2. This power density was used for all heater sections in every test case. The testing parameters to find the minimum ice thickness for effective shedding is presented in Table 3. As stated in the previous section, the *Light, Medium* and *Severe* icing conditions were sought.

Table 3: Test parameters to find minimum thickness for effective ice shedding.

Span %	Droplet Impact Velocity (m/s)	Shedding RPM in AERTS	Temperature (°C)	Heater Power Density (W/cm^2)	Icing Conditions
26.7	52	286	-8	0.385	Light Medium Severe
44.4	52	369			
62.2	52	437			
80.0	52	496			

3.3.3. Power Variation

The last area explored was the variation of power density delivered to the electro-thermal heater zones. These experiments were performed after the minimum ice thickness was found and analyzed for each span-wise heater zone. The objective was to quantify the required shedding times for reduced energies at the correlated minimum ice thickness. As stated in the previous section, effective ice shedding means the shedding event occurred within 30 seconds. Each test case accreted ice at a water droplet impact velocity of 52 m/s, which corresponds to 400 RPM in the AERTS facility. After the minimum ice thickness was accreted, the icing cloud was turned off and the rotor stands spun down. The same ice removal technique as stated earlier was conducted to eliminate the last inch of ice from the tip, span-wise. The rotor stand spun up to the desired RPM that corresponded to the centrifugal force at that heater zone. When the matching centrifugal force was achieved, power was delivered to the electro-thermal heaters at a selected power density. The ice shedding times were quantified and recorded for the *Light* and *Medium* icing conditions. The parameters for the power variation experiments are shown in Table 4.

Table 4: Test parameters for the power variation experiments.

Span %	Droplet Impact Velocity (m/s)	Heater Power Density (W/cm^2)	Shedding RPM in AERTS	Temperature (°C)	Icing Condition
26.7	52	0.385, 0.33, 0.27, 0.225	286	-8	Light Medium
44.4	52	0.385, 0.33, 0.27, 0.225	369		
62.2	52	0.385, 0.33, 0.27, 0.225	437		

Chapter 4: Results and Comparison

The AERTS facility was used to perform experiments concerning the capability of the electro-thermal heaters. The explored heater configuration found the optimum power density needed to keep the rotor blades free of ice in the anti-icing configuration. The hybrid heaters were utilized in a de-icing configuration to promote effective shedding and reduce power consumption. The experimental results are compared with LEWICE modeling to determine discrepancies in temperature and shedding events.

4.1. Anti-Icing

4.1.1. Experimental Results

The anti-icing experiments were conducted in the *severe* icing condition as a conservative approach. The *severe* icing condition is a 0.9 g/m^3 LWC and 35 µm MVD combination at -8°C with a droplet impact velocity of 52 m/s. The required power density to ensure ice free rotor blades at the *severe* icing condition will be successful at the *light* and *medium* conditions, since a lower icing severity will be encountered at the same temperature. The rotor stand has two rotor blades each equipped with two identical heater configurations. The test blades were labeled “BLUE” and “WHITE”. For consistency, the data results exhibited in this chapter are from the WHITE test blade. This mitigates uncertainty on the differences between blades from the heater and thermistor application process. A front-view and side-view schematic of the thermistor locations on the airfoil are shown in Figure 49. Thermistors 1 and 3 are on the leading-edge of the airfoil read temperature of the strip heater on the low-pressure side, while thermistors 4 and 6 read temperature on the high-pressure side of the strip heater. Thermistor 2 reads temperature for the aux heater on the low-pressure side and thermistor 5 reads temperature for the aux heater on the high-pressure side. The test matrix, Table 1, stated in Chapter 2 is displayed to reiterate the variation of power density and icing duration in each test case. The anti-icing experimental results are presented in Figures 50-67.

Each test case displays temperature data and a post-test photograph of the heater section. The legend on the temperature graphs represent each thermistor on the airfoil.

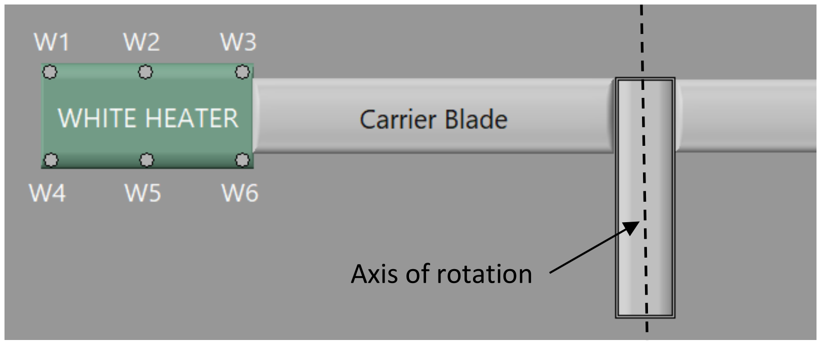

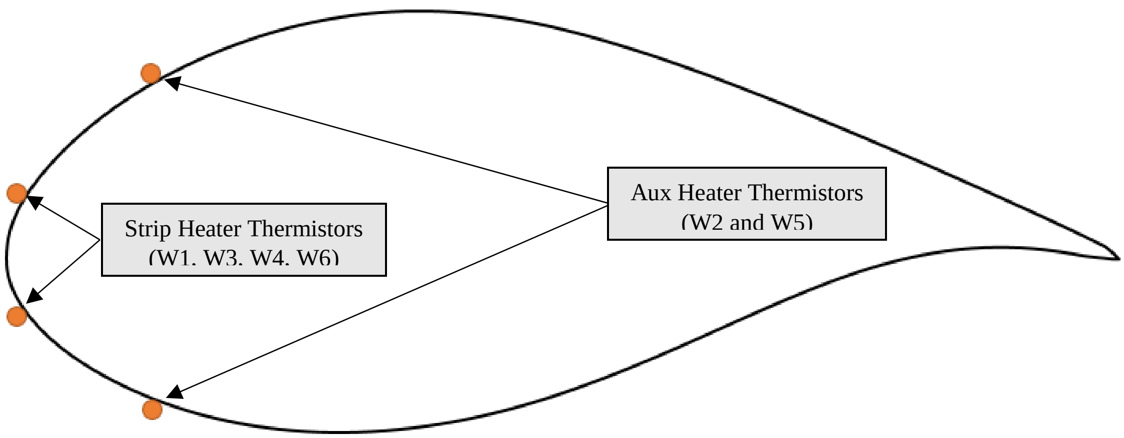

Figure 49: Front-view (top) and Side-view (bottom) schematics of the thermistor locations.

Table 1: Anti-Icing Modeling Test Matrix

Test Case	Power Density Strip (W/cm^2)	Power Density Auxiliary (W/cm^2)	Icing Time (mins)	Temperature (°C)	LWC (g/m^3)	MVD (μm)	Flow Velocity (m/s)
1	0.3	0.09	3	-8	0.9	35	52
2	0.43	0.13	3				
3	0.43	0.18	3				
4	0.56	0.18	3				
5	0.42	0.23	3				
6	0.42	0.37	3				
7	0.58	0.37	3				
8	0.58	0.37	5				
9	0.58	0.37	10				

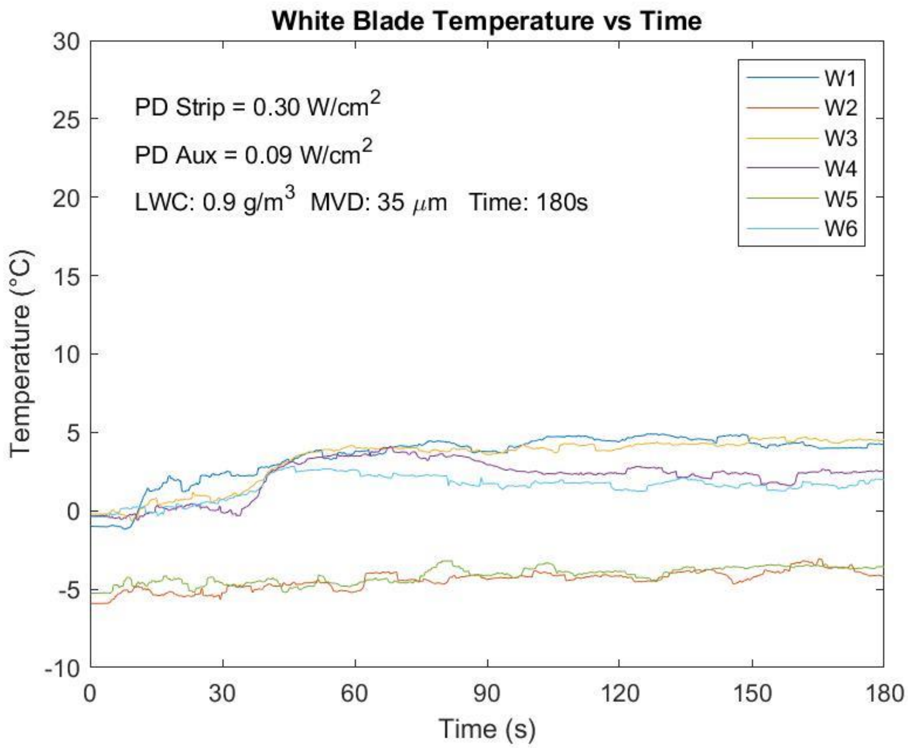

Figure 50: Temperature data – Test case 1.

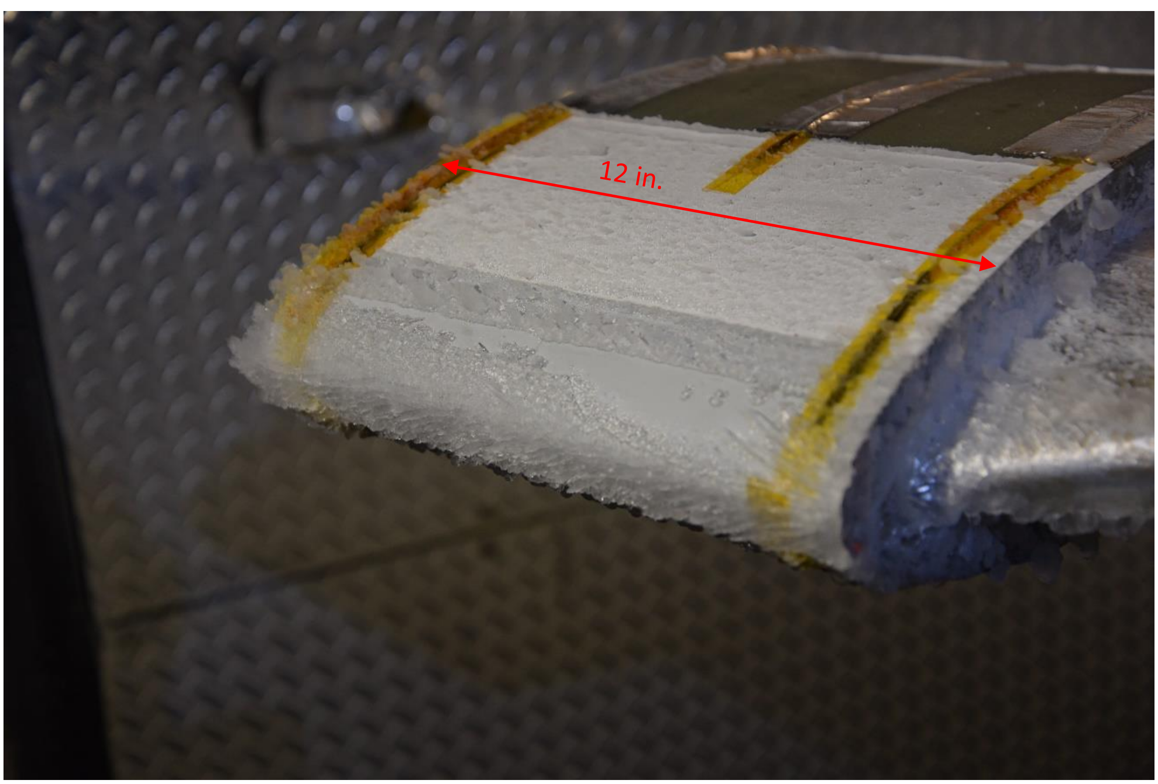

Figure 51: Photograph of heater section – Test case 1.

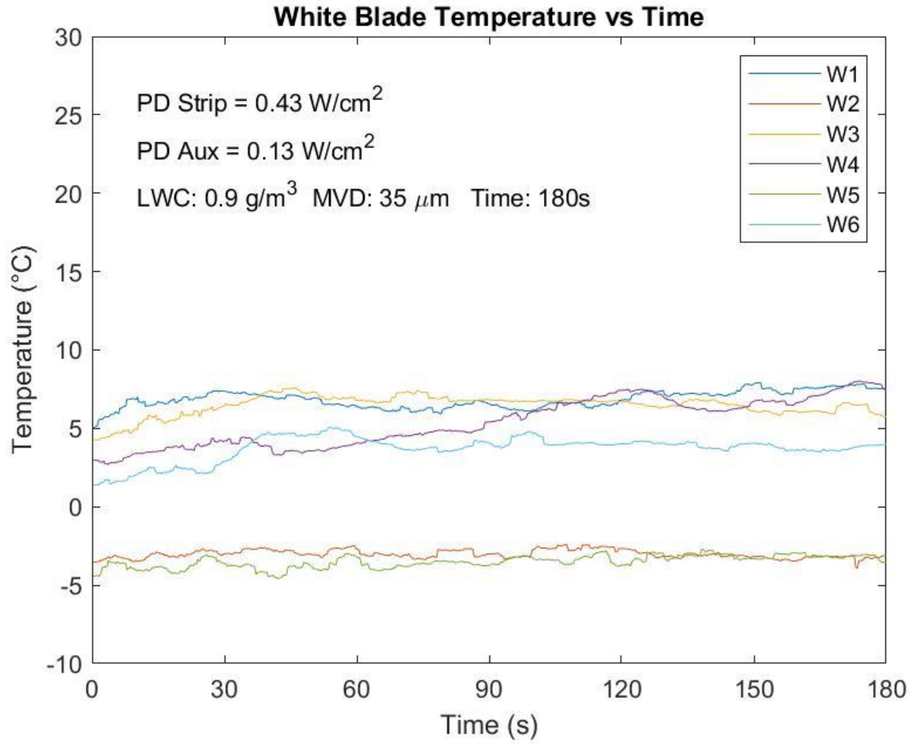

Figure 52: Temperature data – Test case 2.

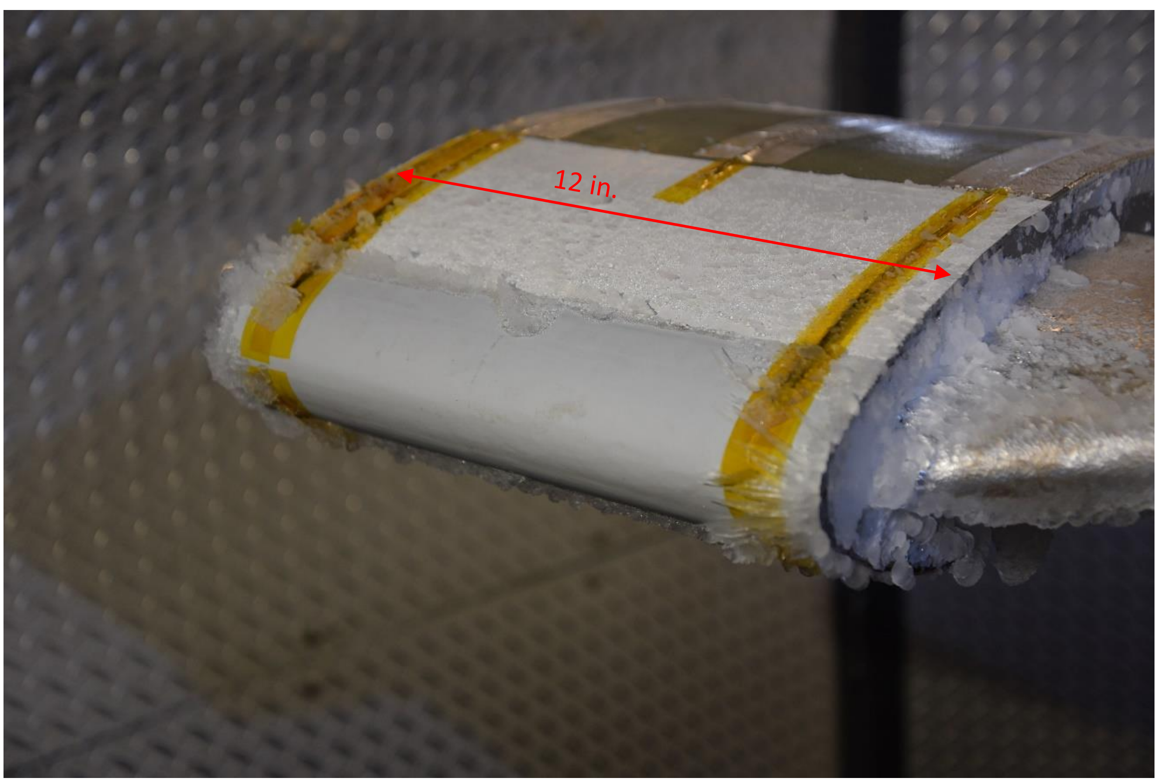

Figure 53: Photograph of heater section – Test case 2.

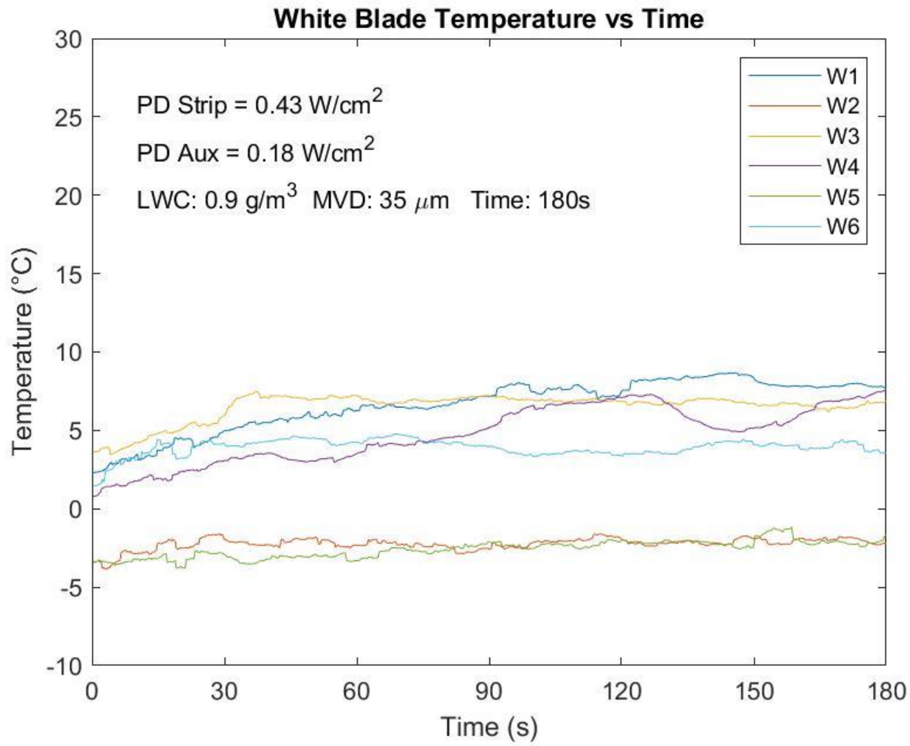

Figure 54: Temperature data – Test case 3.

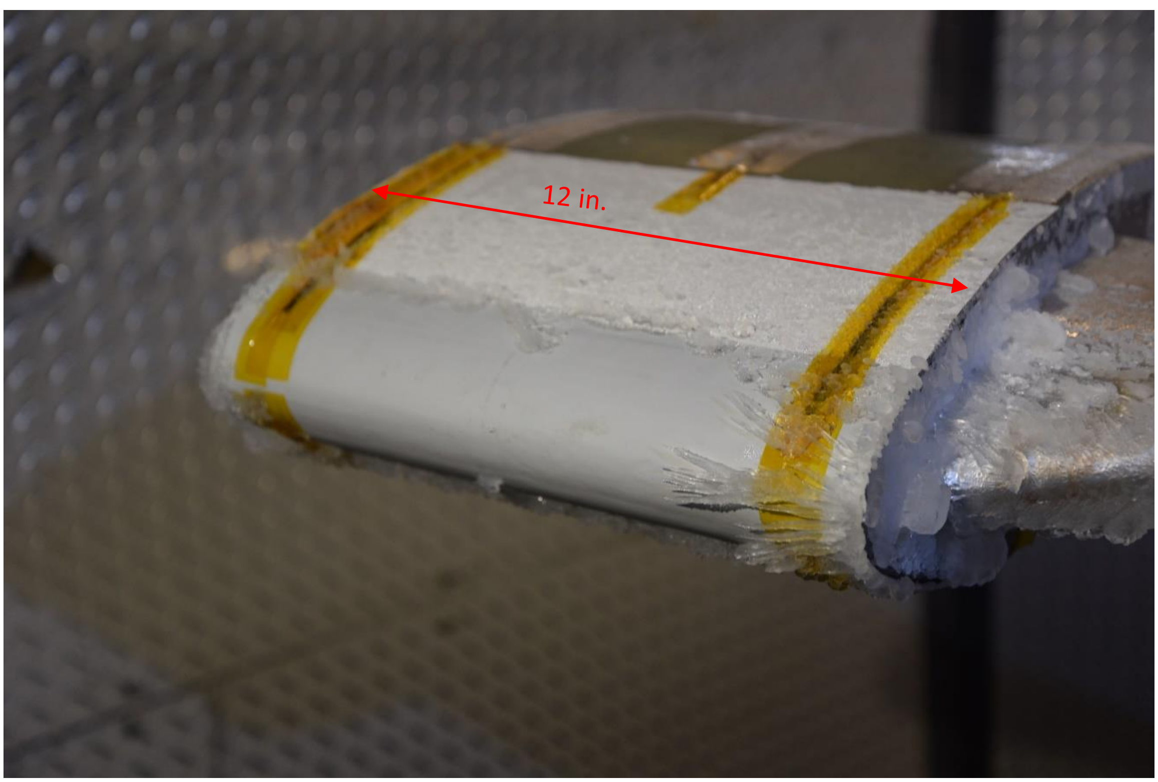

Figure 55: Photograph of heater section – Test case 3.

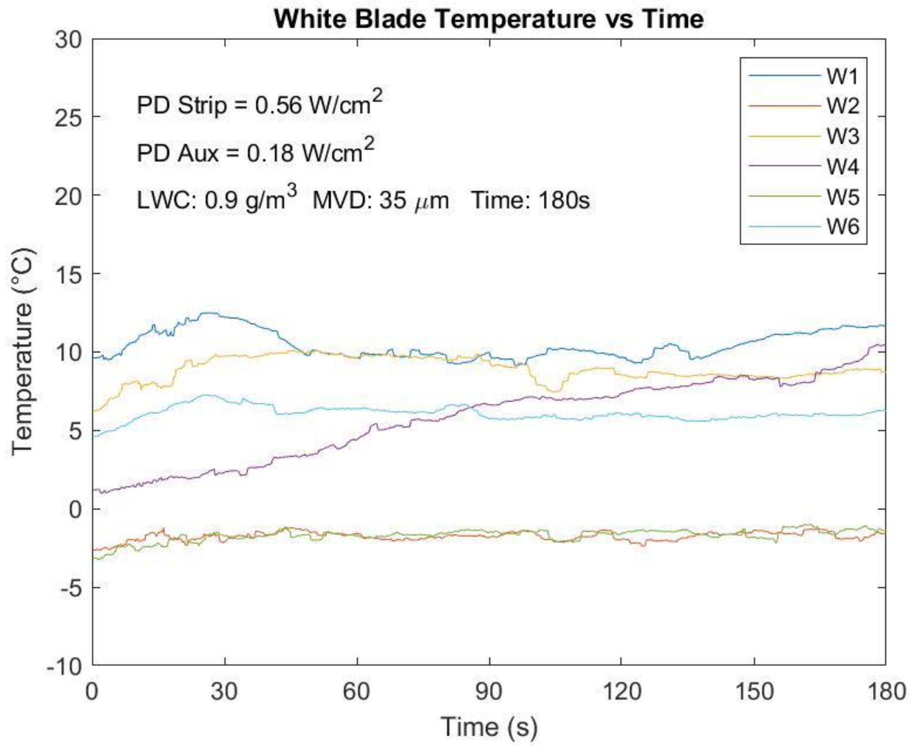

Figure 56: Temperature data – Test case 4.

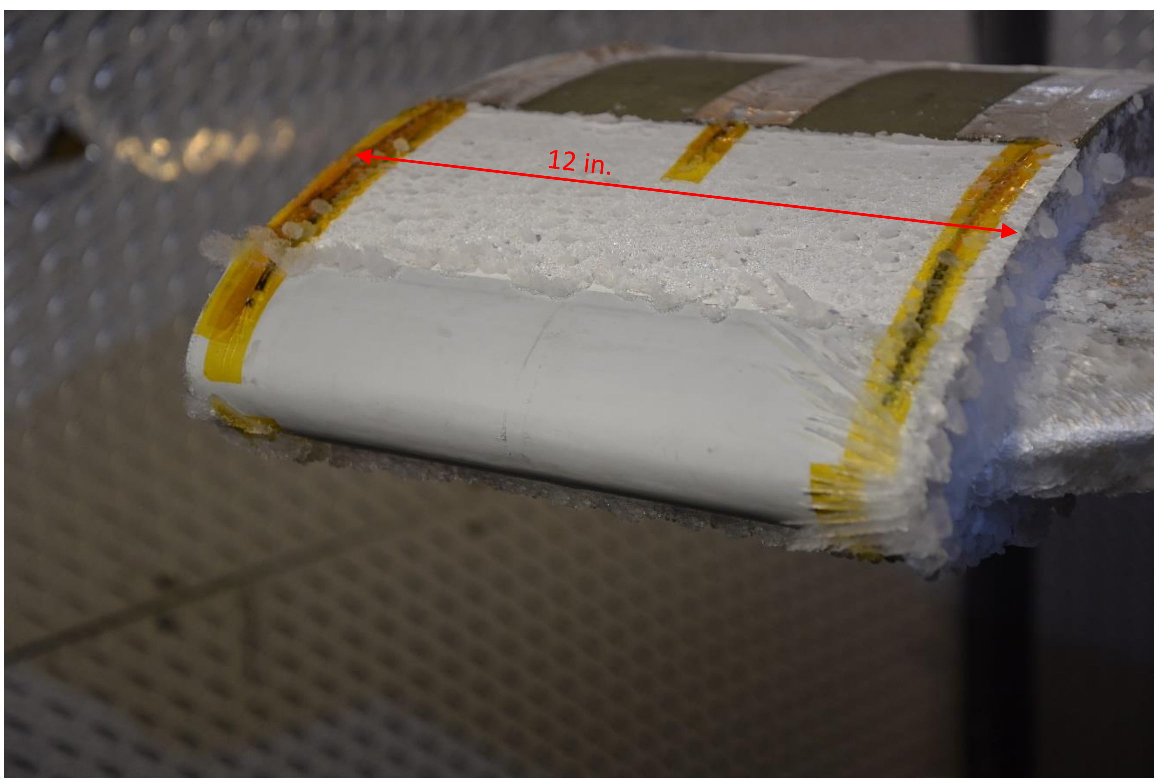

Figure 57: Photograph of heater section – Test case 4.

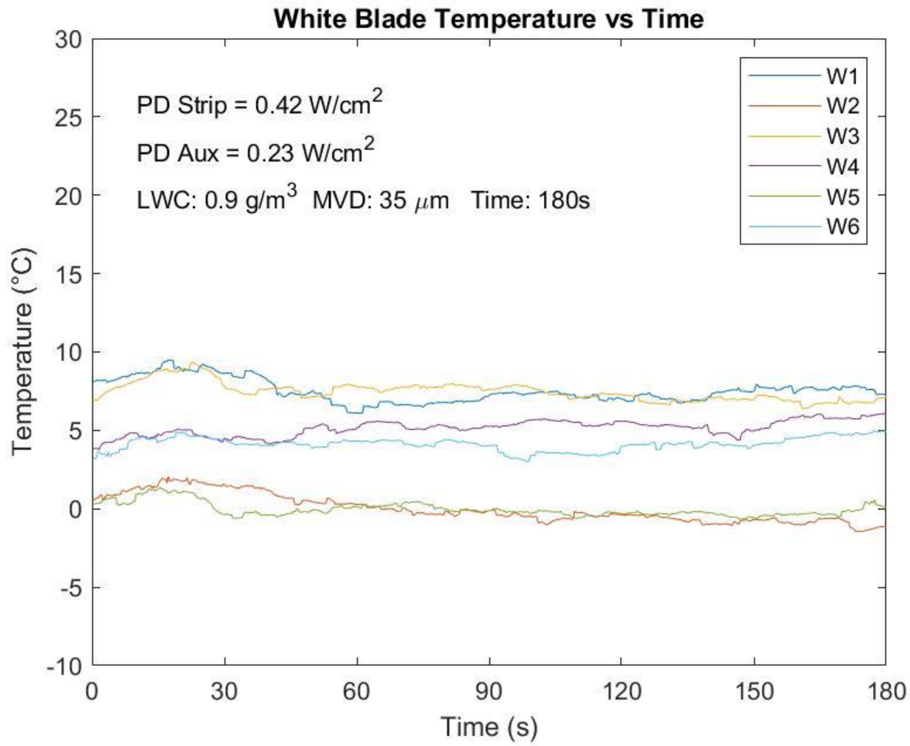

Figure 58: Temperature data – Test case 5.

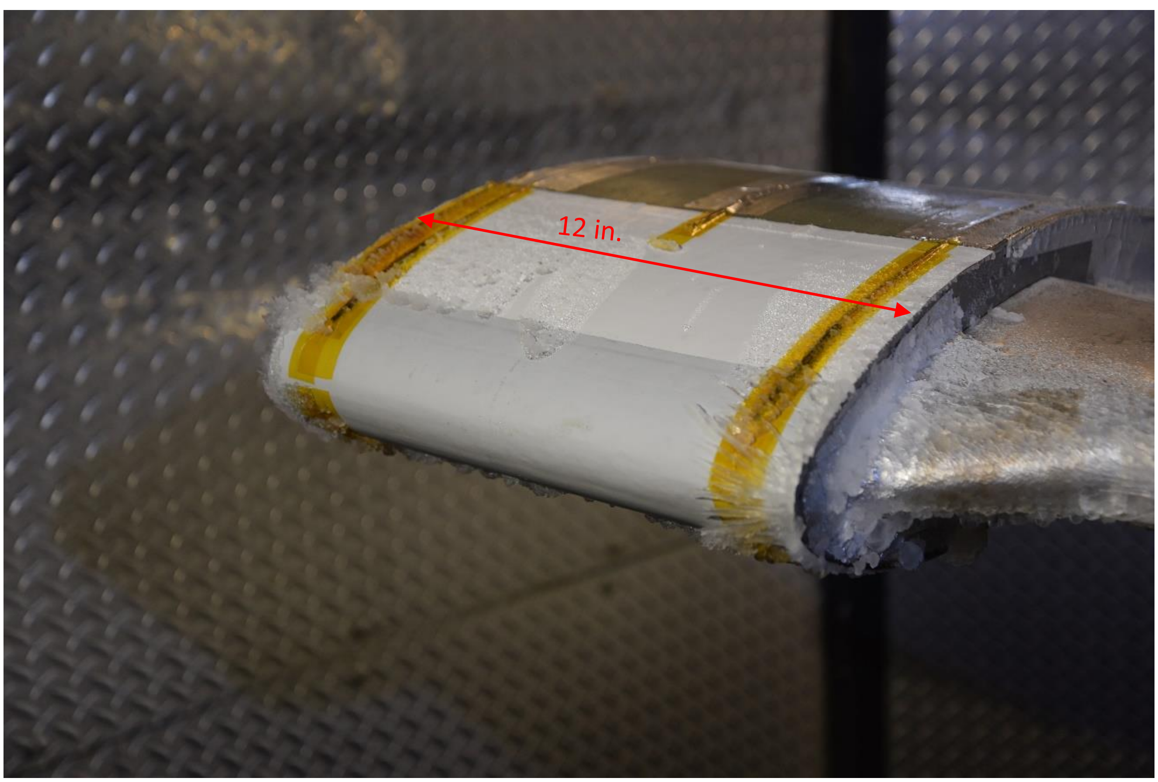

Figure 59: Photograph of heater section – Test case 5.

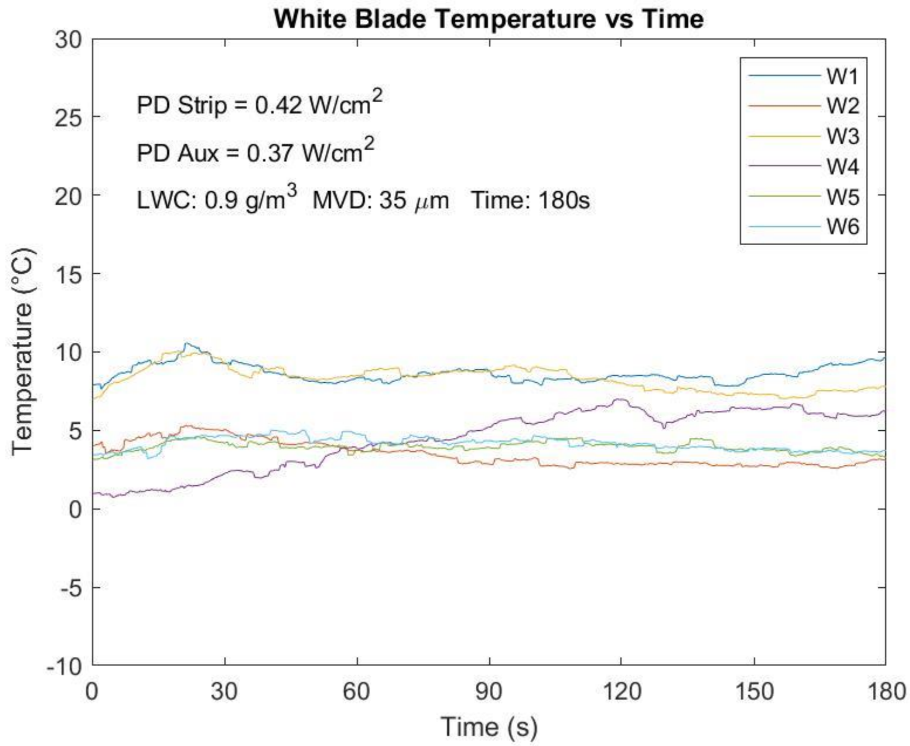

Figure 60: Temperature data – Test case 6.

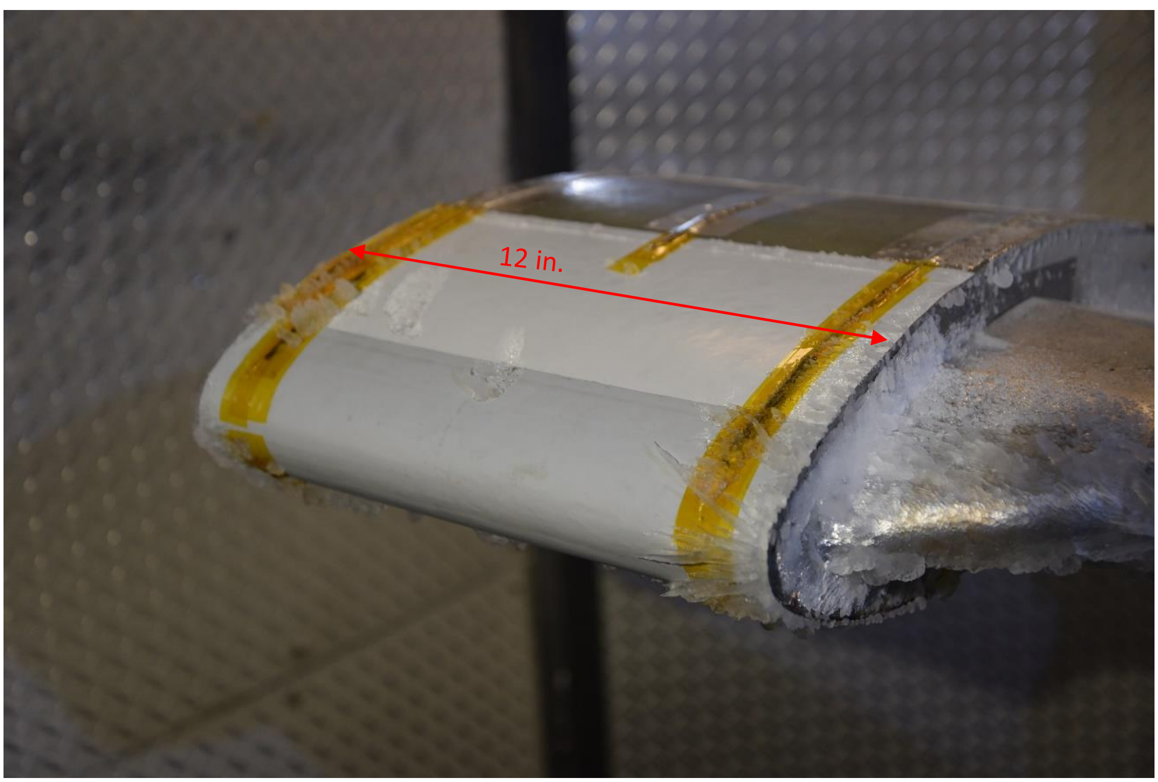

Figure 61: Photograph of heater section – Test case 6.

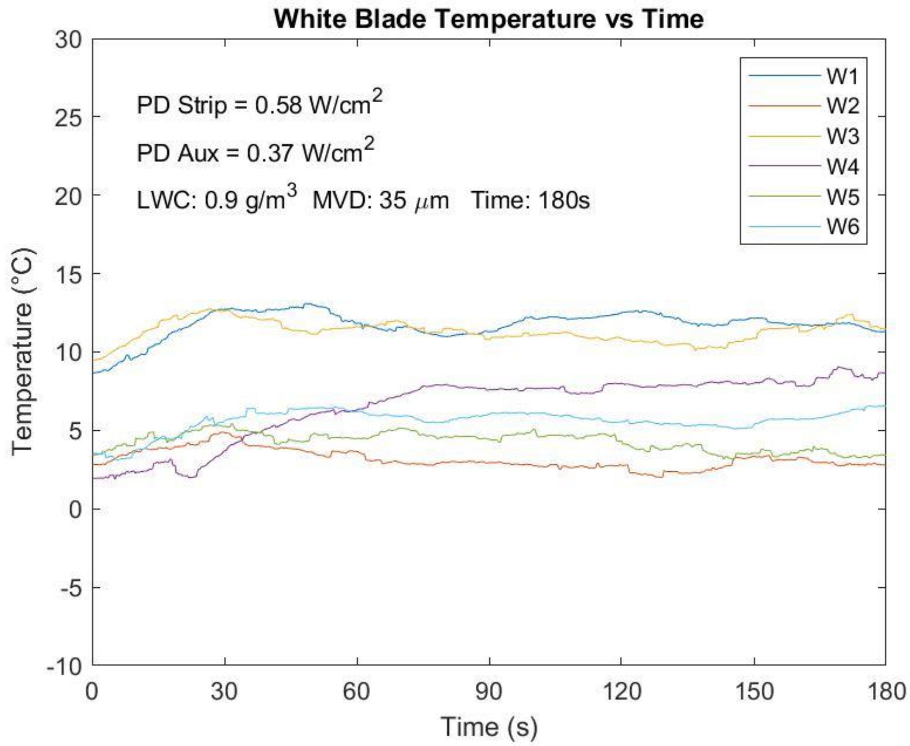

Figure 62: Temperature data – Test case 7.

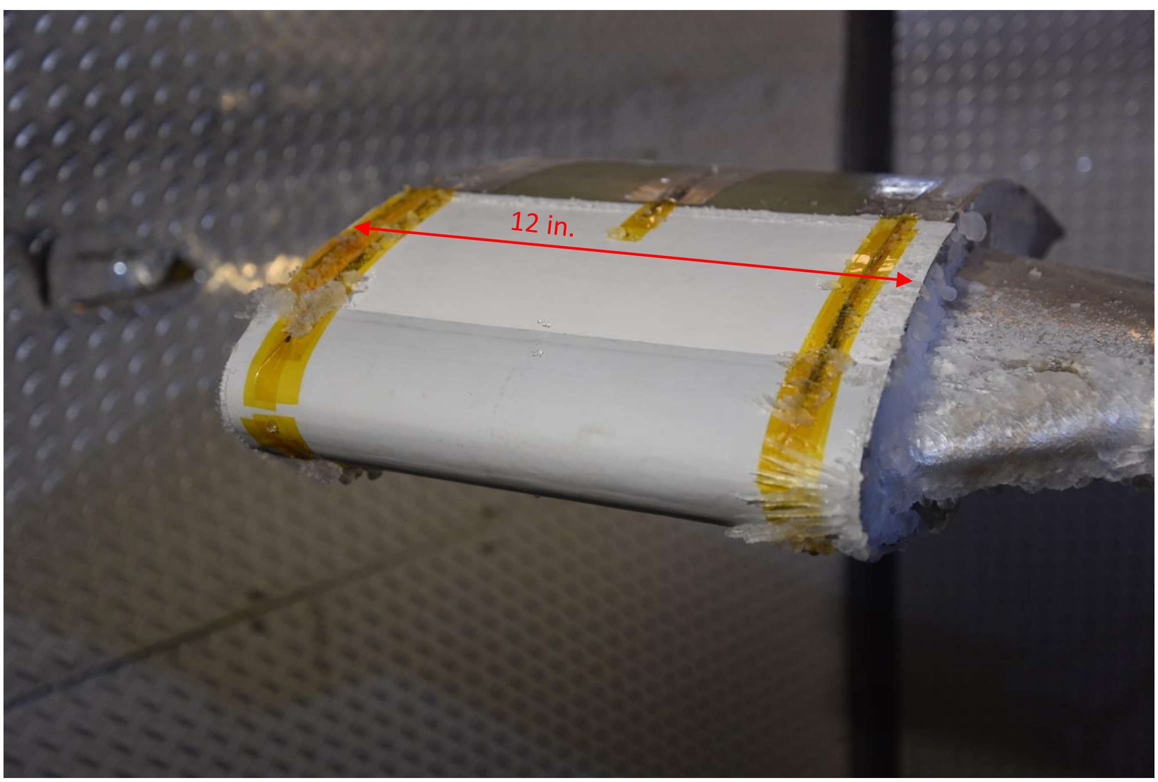

Figure 63: Photograph of heater section – Test case 7.

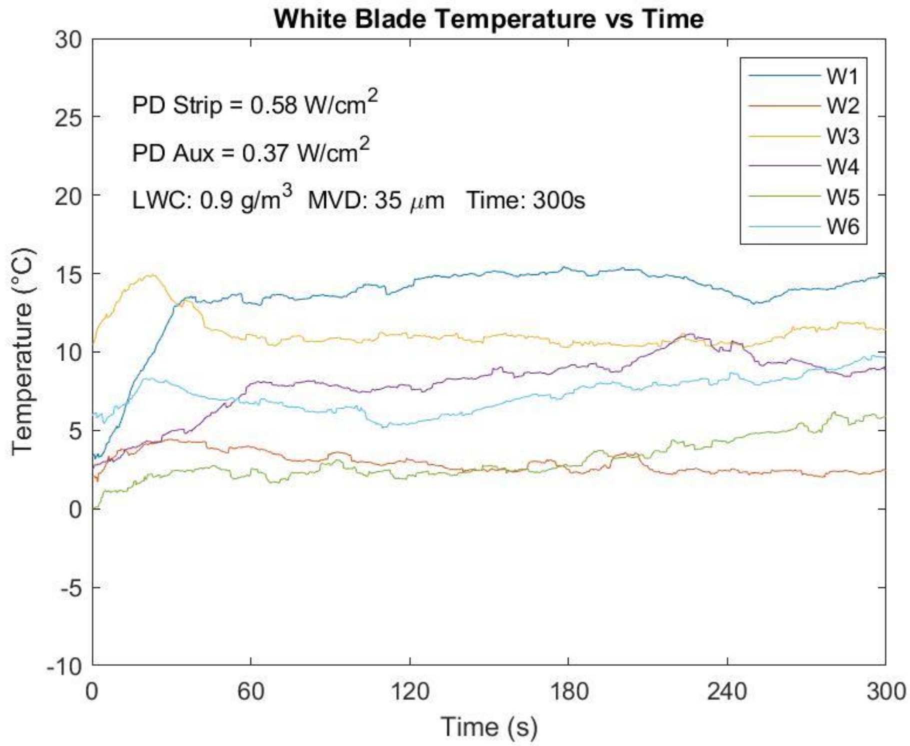

Figure 64: Temperature data – Test case 8.

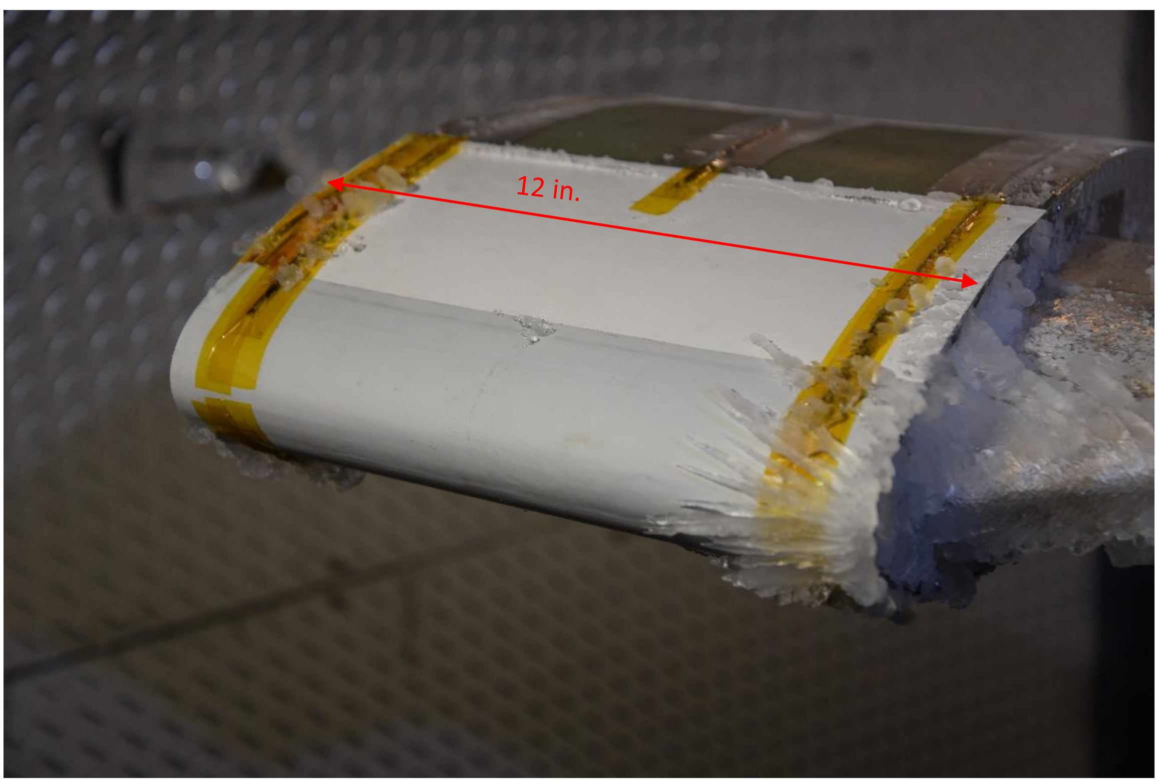

Figure 65: Photograph of heater section – Test case 8.

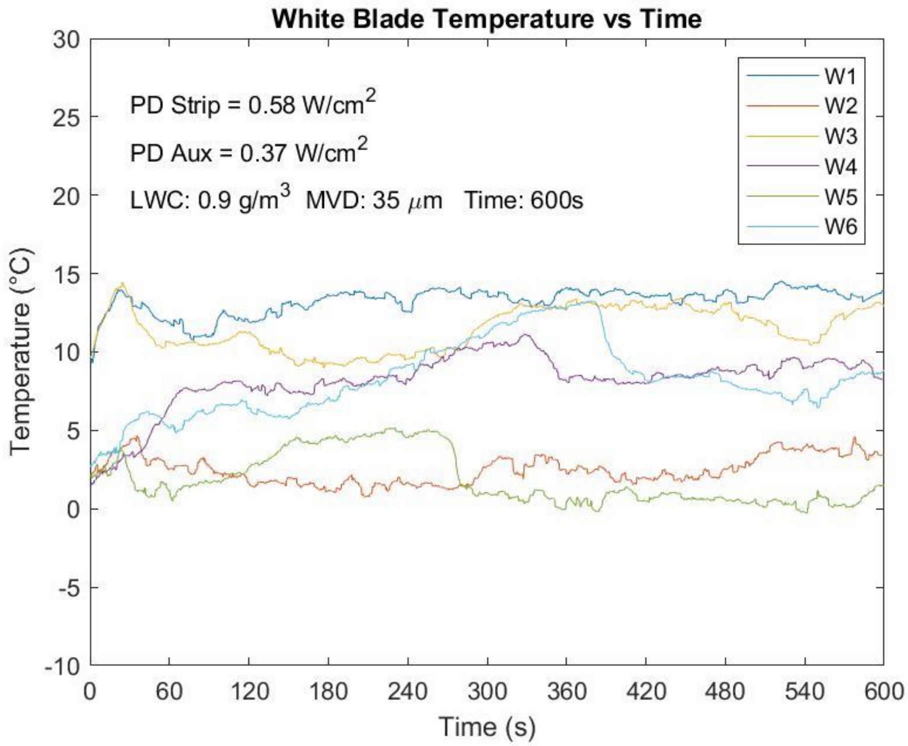

Figure 66: Temperature data – Test case 9.

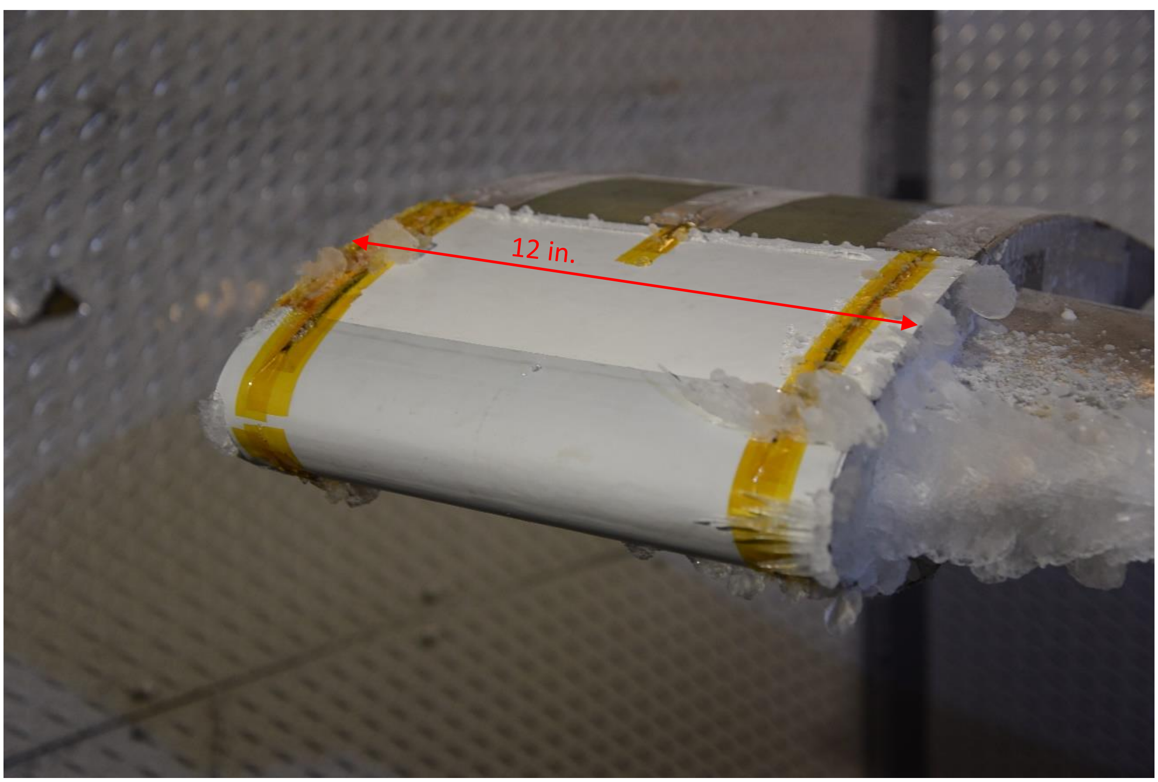

Figure 67: Photograph of heater section – Test case 9.

As seen from the temperature results, certain thermistor locations act similar in groups. Thermistors 1 and 3 are located on the top side of the leading edge and prove to be the hottest locations. Thermistors 4 and 6 are located on the bottom side of the leading edge and are typically colder than thermistors 1 and 3. Lastly, thermistors 2 and 5 are located on the aux heaters in the aft direction of the airfoil. As predicted in the design phase, this location grouping produced the lowest temperature results. The output temperature for the strip (top and bottom) and aux heater were averaged and plotted. The progression of the average temperature through each test case is shown in Figure 68. The average temperature output vs power density for the strip and auxiliary heaters are displayed in Figure 69. The correlation coefficients for the strip (top and bottom) and aux heaters are also presented, which is the percentage of the response variable variation that is explained by a linear model. The correlation has a range from -1 to 1, where 1 is a strong positive correlation. This statistical measurement identifies how close the data is to the fitted regression line.

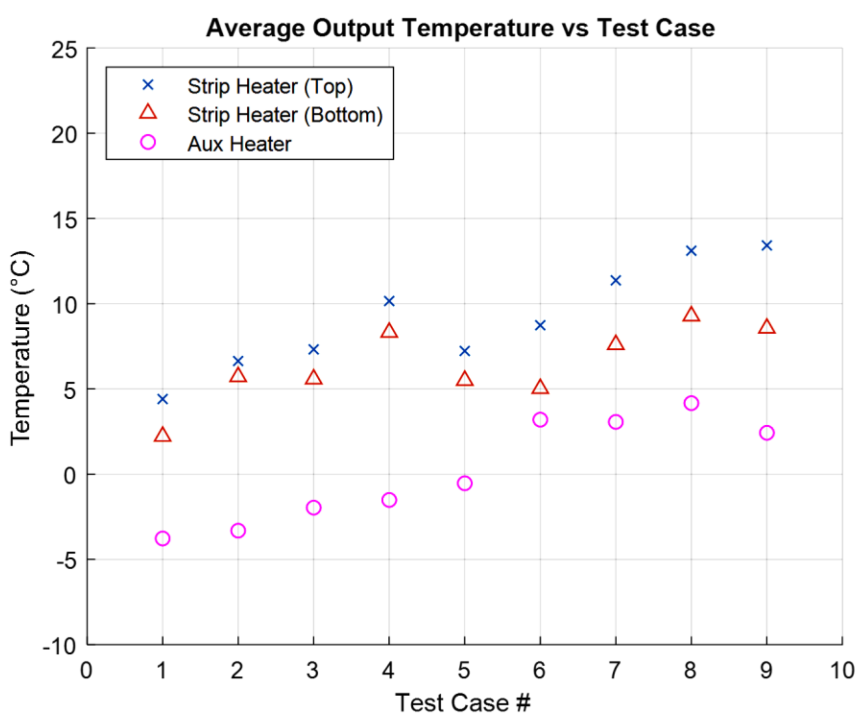

Figure 68: Average output temperature vs Test case.

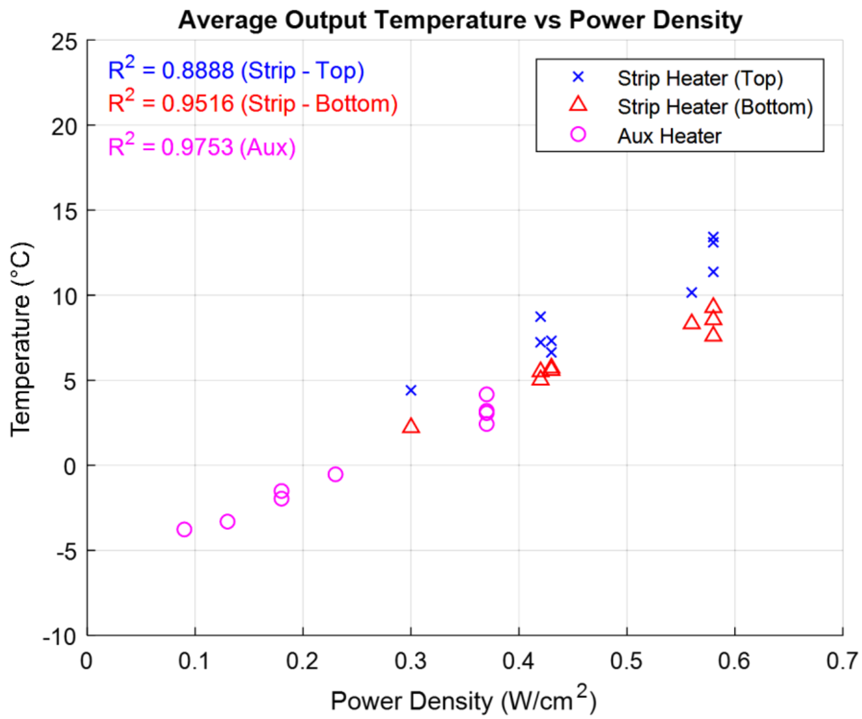

Figure 69: Average output temperature vs Power density.

The objective of these experiments was to find the power density needed to keep the airfoil free of ice at all times. The severe icing condition was selected as a conservative approach, due to the high combination of LWC and MVD. Based on the experimental data collected, anti-icing is not feasible with the available power requirements in the severe icing condition. The strip heater on the leading edge requires a 0.58 W/cm^2 power density, while only 0.385 W/cm^2 is available on the wind turbine. The 0.58 W/cm^2 power density was tested for several durations to ensure the rotor blade remains ice-free. From experiments, the average surface temperature on the leading-edge heater needs to reach a minimum steady-state value of 10°C to operate successfully in the anti-icing configuration.

4.1.2. LEWICE Comparison

The experimental temperature data obtained was compared to the analytical modeling from LEWICE. The final output temperature for the top and bottom side on the leading edge were documented after each experiment. The final temperature produced from LEWICE was recorded and compared to the appropriate experimental test case, shown in Figure 70. Since the icing conditions remained consistent, the output temperature from each power density was analyzed. The output temperature vs power density for the experiment and LEWICE is presented in Figure 71. LEWICE temperature predictions are consistently lower than the experimental data on the top-side of the leading edge. The average error percentage between the top-side temperature data and LEWICE prediction is 39.5%. However, the temperature predictions from LEWICE are closer to the experimental data on the bottom-side of the leading edge. The average error percentage between the bottom-side temperature data and LEWICE prediction is 11.1%.

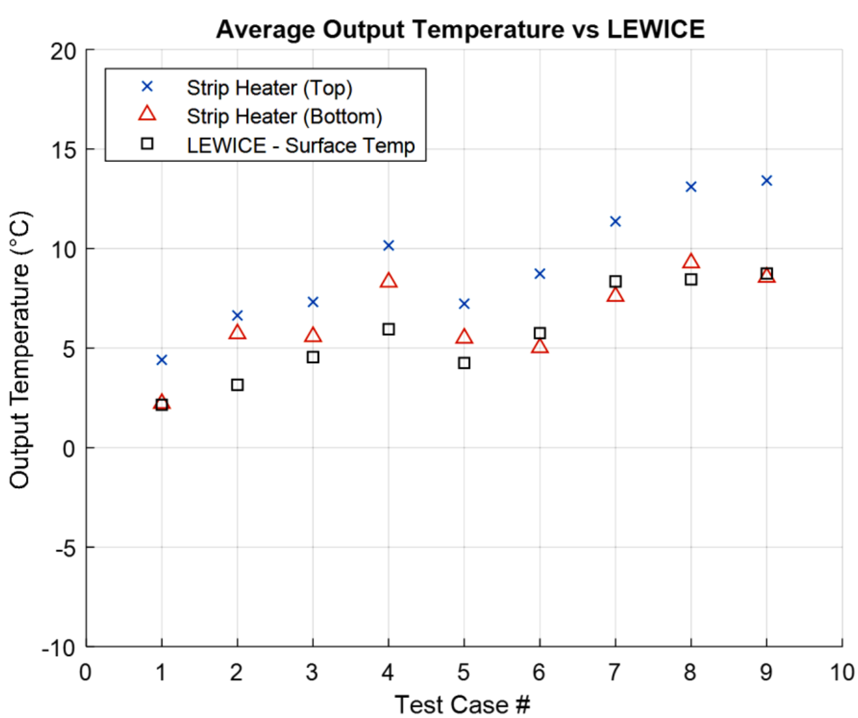

Figure 70: Experimental vs LEWICE output temperatures for each test case.

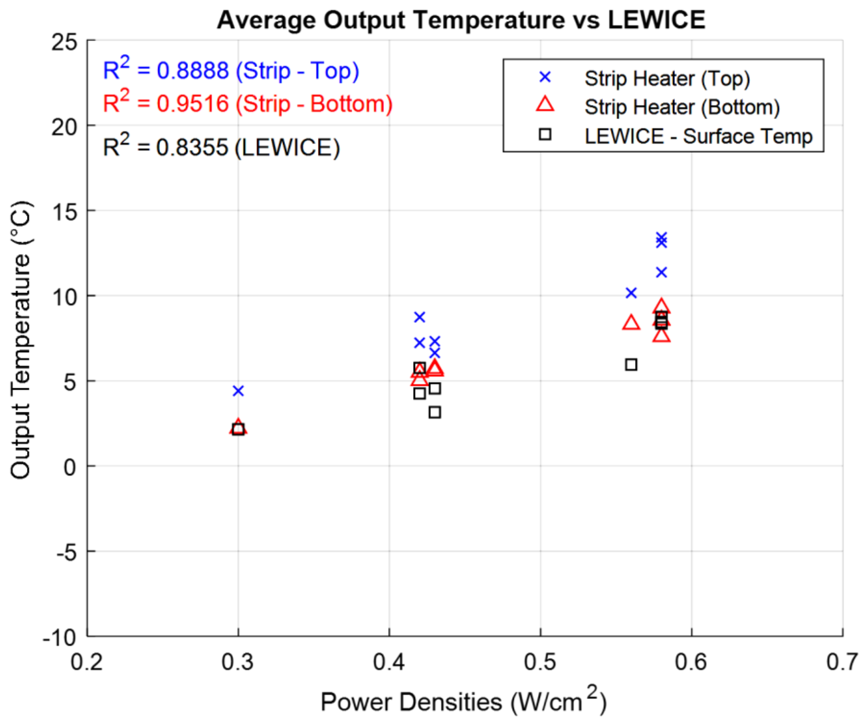

Figure 71: Experimental vs LEWICE output temperature for various power densities.

LEWICE verified that the power densities used in test case 9 prevent ice accretion on the airfoil. The final ice shape was graphed on the clean airfoil to display the locations of the ice thickness. As shown in Figure 72, the predicted ice shape produces a clean leading-edge, but runback water refreezes in the aft section of the airfoil.

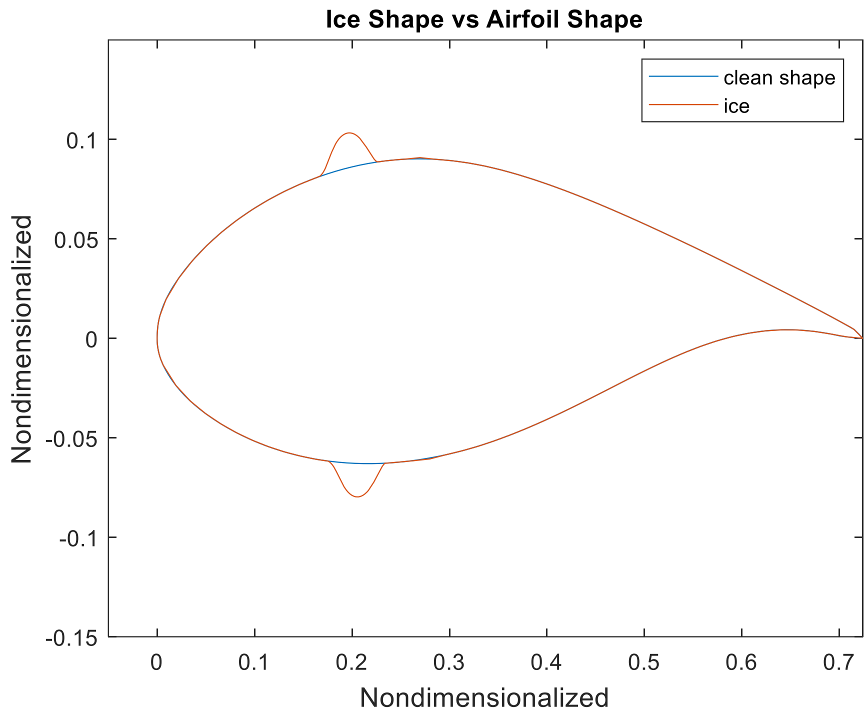

Figure 72. Predicted ice shape in LEWICE for test case 9.

The modeling efforts in LEWICE have the capability to predict output temperatures within a reasonable error on the pressure-side of the airfoil. The output temperatures and ice shapes confirm that the available power on the wind turbine is not feasible in the anti-icing configuration.

4.2. De-Icing

Since the anti-icing configuration is not possible with the power restrictions on the wind turbine, de-icing approaches must be considered for the ice protection system. The maximum available power density (0.385 W/cm^2) for each heater section was used to experimentally design the de-icing system. Ice accretion rates along the span of the rotor blade coupled with cohesive failure experiments design a time-sequence controller to allow a predetermined ice thickness to accrete and then activate heaters and use centrifugal forces to shed the ice.

4.2.1. Design Process

Many parameters must be considered during the design phase of an ice protection system. A flowchart characterizing the design process for the de-icing IPS is shown in Figure 73. Utilizing an analytical heat transfer modeling software is imperative to identify an initial power density. First, the dimensions of the heater zones must be selected and modeled based on power requirements from the manufacturer. The heater configuration can be optimized by performing many iterations in the modeling phase to find the lowest initial power density. This power density is used in the experiments to find the minimum ice thickness needed for effective shedding (less than 30 seconds).

The testing phases are categorized by “Rotor Environment” and “Power Variation”. Initially, the testing temperature in the cooling chamber is selected based on the operator’s knowledge of the wind farm location. The category, Rotor Environment, begins by matching the droplet impact velocity along the span of the rotor blade. These opening tests identify the ice accretion rate along the span of the rotor blade for various LWC values.

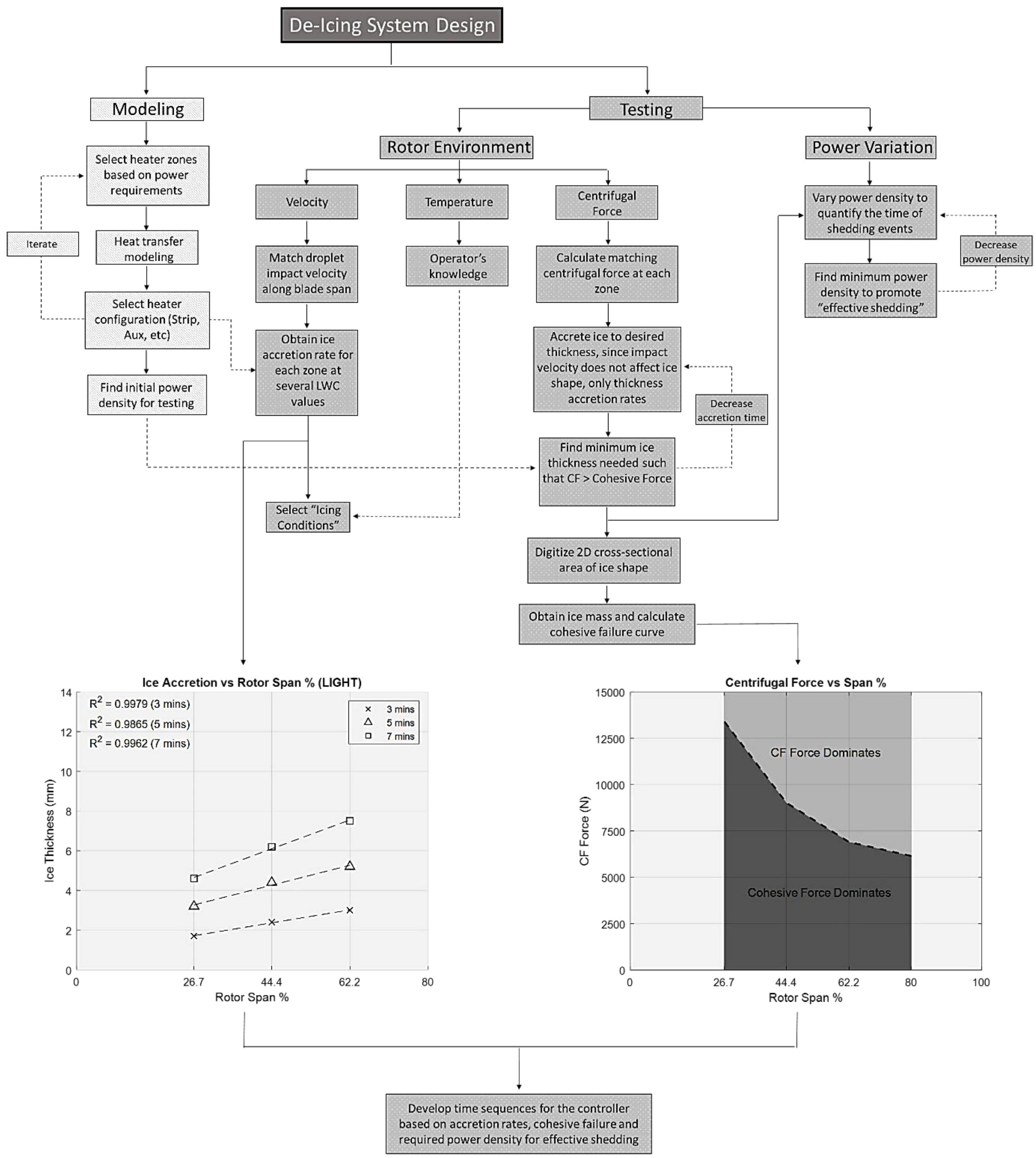

Figure 73. Flowchart identifying the design of the de-icing IPS.

The ice accretion rates coupled with the temperature identify the "Icing Conditions", which will be utilized by the heater controller to select the appropriate time sequence. Then, the centrifugal force in the testing facility must match the full-scale blade span at each heater zone location. By matching ice masses, these experiments identify the boundary of cohesive failure. If the ice thickness is too small, the cohesive force of the ice will dominate centrifugal forces, even if the ice-surface interface on the airfoil is melted. Therefore, there exists a minimum centrifugal force required to effectively shed the ice layer from the rotor blade. During these tests, ice is accreted to a desired thickness then the rotor stand spins to the appropriate RPM that matches the full-scale inner-zone location of the heater and delivers the selected power density from the modeling phase. If ice layer sheds in less than 30 seconds, the next test will decrease the accretion time, which decreases the ice mass. The objective is to find the minimum ice thickness needed for "effective" shedding at each heater zone location. After the thicknesses are found, the 2D cross-sectional are of ice is digitized to obtain the ice mass and calculate the centrifugal force. The final set of experiments are from the category, Power Variation. These experiments simply quantify the time of the shedding events as power density is decreased.

Lastly, the information gathered through the design process produces the capability to design time sequences for each icing conditions. The time sequences are utilized by the controller after ice is detected. Once ice is detected by hardware, a time begins and the ice thickness detector will read a thickness after one minute. The ice accretion rate determines the icing condition and the appropriate heater sequence is activated.

4.2.2. Experimental Results

4.2.2.1. Linear Ice Accretion Thickness

The objective of these tests was to find the ice accretion rate (slope of ice thickness over time) along the span of the rot blade at three different icing conditions. Data from these experiments play a role in the design of the de-icing time sequence controller. A *Light* icing condition was triggered by a 0.2 g/m^3 LWC and 20 μm MVD at a temperature of -8°C. A *Medium* icing condition consisted of a 0.4 g/m^3 LWC and 20 μm MVD at -8°C. Lastly, 0.9 g/m^3 and 35 μm MVD combination was selected for the *Severe* icing condition. The nomenclature for the icing conditions are used throughout the de-icing experiments and results.

The RPM established in AERTS during ice accretion must represent the water droplet impact velocity on the wind turbine. For this study, convective cooling plays a major role in the initial stages of ice accretion. A MATLAB code was developed to calculate the RPM correlation in AERTS that represent the impact velocity at a chosen span percentage. After spinning up to the appropriate RPM, the icing cloud was turned on for three different durations: 3, 5 and 7 minutes. The three icing durations would experience the light, medium and severe icing conditions. The key parameters for this set of experiments is shown in Table 5.

Table 5. Linear Ice Accretion Test Matrix.

Span %	Impact Velocity (m/s)	AERTS RPM	Accretion Time (mins)
26.7	22.65	174	3, 5 and 7
44.4	37.66	289	3, 5 and 7
62.2	52.76	405	3, 5 and 7
80.0	67.86	521	3, 5 and 7

Unfortunately, 80% span was not tested in the AERTS facility due to the large aerodynamic loads on the rotor stand at such speed. Also, at 67.86 m/s tip speeds (521 RPM), both blades would need to shed simultaneously or the imbalance on the system would become too large for the rotor stand. Note the impact velocity is linear with RPM, while the centrifugal loads are square of the RPM. Therefore, once the desired ice shape was accreted, the RPM was varied to match centrifugal loads of the full-scale span location.

The data produced from this research discovered linear ice accretion along the span of the rotor blade. If the origin of the icing cloud is determined, then the accretion rate delivers the capability to know the thickness at each span-wise heater location at any future time. The ice thickness at span percentages outside of the range, 26.7% to 62.2%, can be extrapolated from the data trend. The ice accretion for 3, 5 and 7 minutes at *light* icing conditions is shown in Figure 74.

The ice thickness for *medium* and *severe* icing conditions are presented in Figures 75 and 76, respectively.

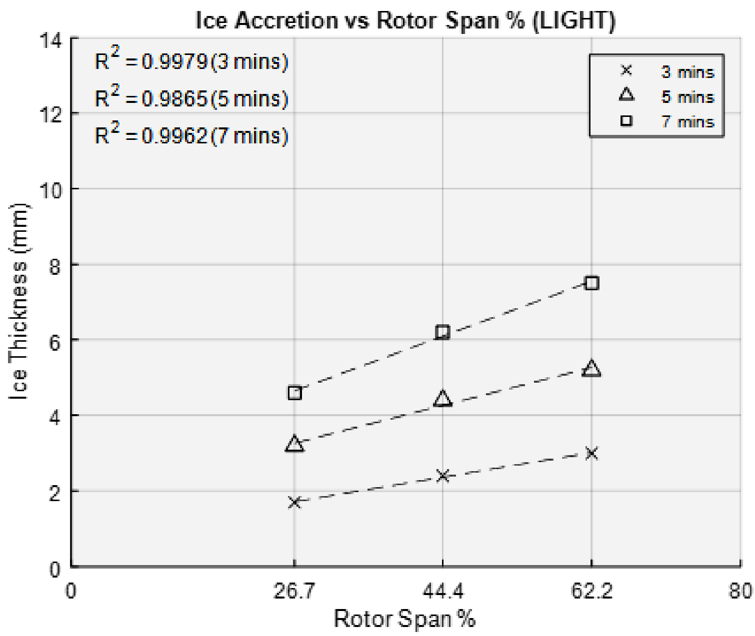

Figure 74. Ice thickness measurements for Light icing conditions.

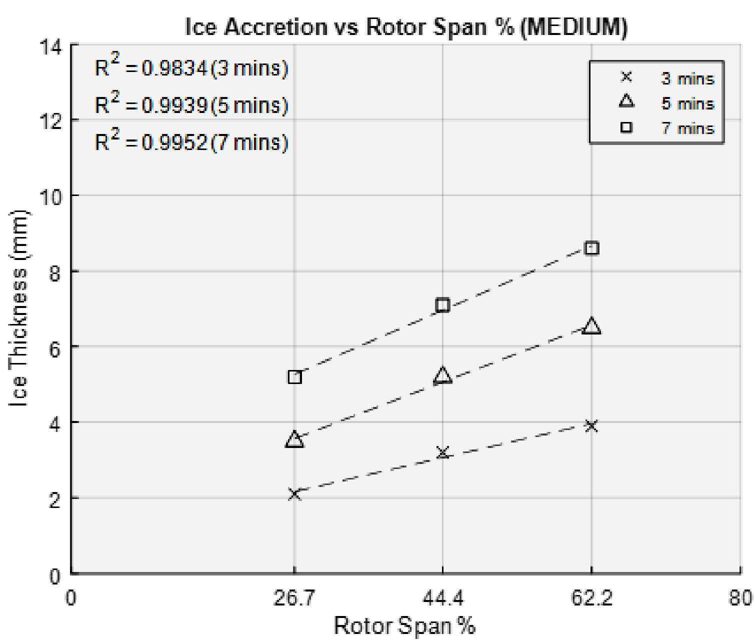

Figure 75. Ice thickness measurements for Medium icing conditions.

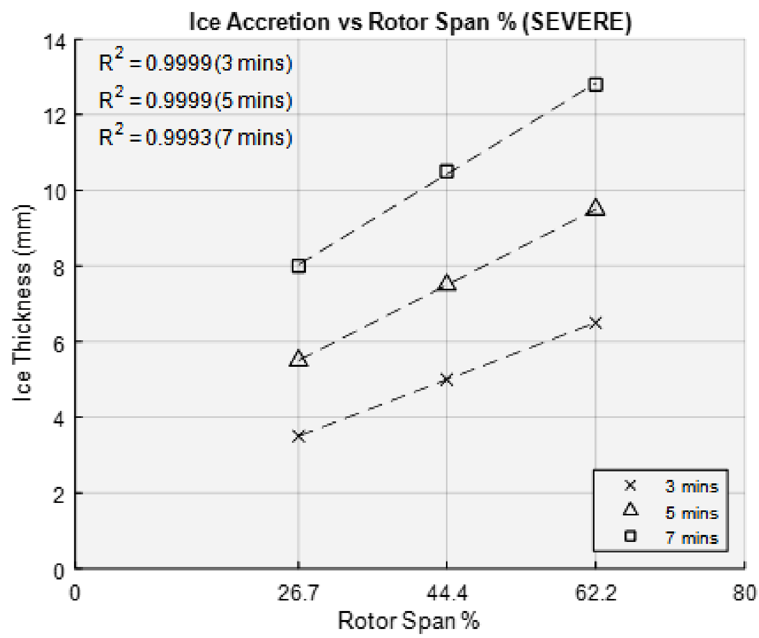

Figure 76. Ice thickness measurements for Severe icing conditions.

The data has strong positive correlation and demonstrates a linear behavior for ice thickness along the span of the rotor blade. The experimental measurements can be utilized to obtain the ice accretion rate at each zone location. Ice detection hardware can identify the initial presence of ice on the rotor blades. After a minute, the ice detection hardware can measure the ice thickness and the controller interface can calculate the ice accretion rate. This ice accretion rate determines the severity of the icing conditions and activates the appropriate heater sequence. The accretion rates for each zone in all the icing conditions is presented in Table 6.

Table 6. Ice Accretion Rates (mm/min) for each zone.

Heater #	Span %	Accretion Rate (LIGHT)	Accretion Rate (MEDIUM)	Accretion Rate (SEVERE)
1	26.7	1.350 mm/min	1.450 mm/min	1.850 mm/min
2	44.4	1.125 mm/min	1.175 mm/min	1.575 mm/min
3	62.2	0.950 mm/min	0.975 mm/min	1.375 mm/min
4	80.0	0.725 mm/min	0.775 mm/min	1.125 mm/min

4.2.2.2. Minimum Ice Thickness for Shedding

The ice mass ideally would shed in a timely manner before it becomes a hazard to the infrastructure of the wind turbine or the surrounding environment. Also, the allowed accreted ice mass must not produce high aerodynamic performance degradation. The following test cases identify the minimum ice thicknesses needed to promote ice shedding at each heater section. The span percentage at the origin of each heater section was selected to represent the centrifugal force to ensure cohesive bridging does not occur for a given minimum ice thickness. This is a conservative approach to accurately test for cohesive failure. For shedding to occur, the adhesion strength of the ice bridging the heater sections must be less than the centrifugal force pulling on the ice mass in the span-wise direction. If the cross-sectional area of the ice is too small, the adhesion strength will dominate the centrifugal force creating the inability to shed ice. Table 7 presents the parameters for these experiments.

Table 7. Properties for Minimum Ice Thickness Shedding.

Heater #	Span %	Droplet Impact Velocity (m/s)	Heater Power Density (W/cm^2)	Shedding RPM in AERTS
1	26.7	52	0.385	286
2	44.4			369
3	62.2			437
4	80.0			496

The procedure for each test case was consistent to remove as much uncertainty as possible. Each test case accreted ice at -8°C and an impact velocity of 52 m/s (400 RPM in AERTS), deeming the ice accretion rate constant through each icing condition. The impact velocity mostly affects the ice shape and has small effects on the heat transfer once ice is accreted (ice acts as an insulator).

The increase of velocity for inner sections (26.7% and 44.4%) simply means that the accrete rate was increased and does not have any effects on the capability of the heaters to affect the bond-line. It must be noted that the ice shape could deviate slightly from those accreted at representative span velocity, but ultimately, only the ice mass is of importance for this study. After the test blade accreted an ice shape for a predetermined time interval, a hot plate was utilized to remove the ice feathers at the tip of the paddle blade and photograph the cross-sectional area of the ice shape. After, the ice on the edge of the heater was removed to ensure the ice mass was free to shed. This is due to the lack of heat production above the copper bus bar in the heating element. This procedure was repeated for the *light, medium and severe* icing conditions. Figure 77 is a photograph that illustrates the tip of the heater section being prepared for shedding.

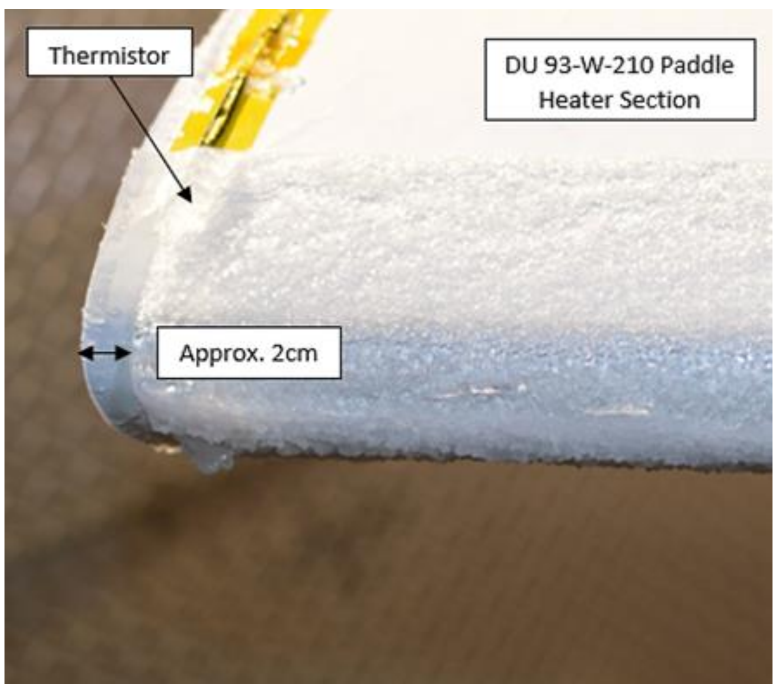

Figure 77. Photograph of the ice removed on the edge using a hot plate.

After the rotor test blade is prepared for shedding, the rotor stand spun up to the appropriate centrifugal force at the full-scale blade span percentage of interest. When the rotor stand reaches the desired RPM, the relay module activates the heaters and delivers a 0.385 W/cm^2 power density from the voltage variacs. Due to power restrictions on the full-scale wind turbine, the maximum power density available was 0.385 W/cm^2. The time limit for effective ice shedding is 30 seconds. If the ice mass sheds within 30 seconds, the following test case will accrete ice for a shorter duration of time, decreasing the thickness/mass of the ice. This method is conducted until the minimum ice thickness is found for each heater section. After the test was competed and the data was saved, the rotor blades were cleaned and the test parameters are updated in LabVIEW codes (cloud control and heater control) for the next experiment. The data trends for these tests are presented in Figure 78.

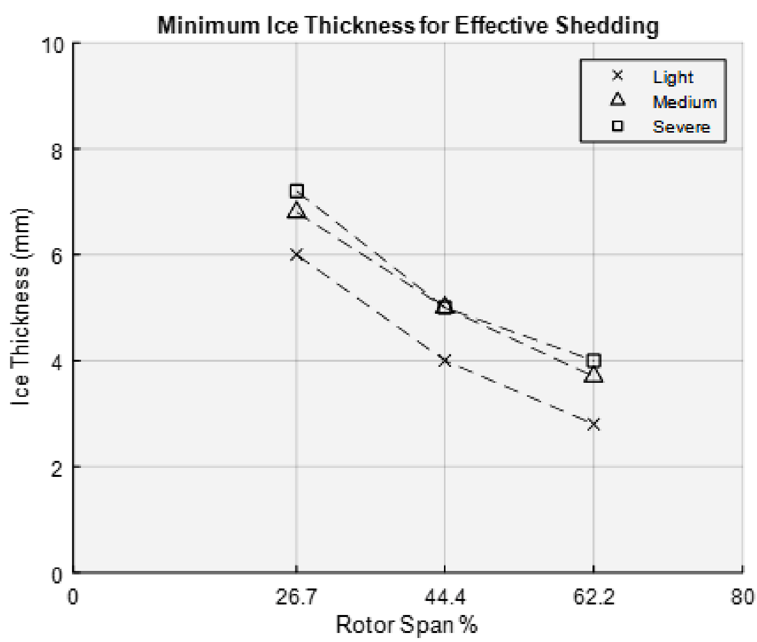

Figure 78. Minimum ice thickness needed for effective shedding.

The minimum ice thicknesses for the *light* icing conditions at the 26.7%, 44.4% and 62.2% span are 6 mm, 4 mm and 2.8 mm, respectively. The average shedding time between both rotor-blades for these tests were 24, 25 and 28 seconds. For the *medium* icing conditions, the minimum ice thicknesses are 3.7 mm, 5 mm and 6.8 mm, respectively. The average shedding time for these cases were 25, 25 and 23 seconds. Lastly, the minimum ice thicknesses for the *severe* icing conditions are 4 mm, 5 mm and 7.2 mm, respectively. The ice shedding times for these tests were 34, 24 and 20 seconds.

The minimum thicknesses along the span of the wind turbine blade for the *severe* icing conditions should be considered for the design of the controller. This is a conservative approach for a great reason; the smallest variation of ice mass could allow the ice adhesion strength to dominate the centrifugal forces. In this situation, the ice shape stays attached to the airfoil as the electro-thermal heaters melt the ice interface on the surface. The ice becomes an insulator and continues to accrete ice on the leading edge and further in the aft direction. The icing dynamics are unpredictable thereafter and eventually the wind turbine would be forced to shut down due to torque and vibration loads. It is imperious to keep these ice thicknesses at a minimum for the safety of the surrounding environment on the wind farms.

This cohesive failure event happened multiple times during the experiments. The following photographs are from a test case demonstrating the failure to shed and the success of the ice adhesion strength over the centrifugal forces. Figure 79 is an image of an ice shape accreting 9 mm of ice at -8°C in *Medium* icing conditions. Figure 80, from the same test case, displays the melted interface after delivering a 0.385 W/cm^2 power density from the heaters for 180 seconds and failing to shed at 90 RPM. Schematics of the melted interface experienced from cohesive failure are shown in Figure 81. As shown, on the inboard section of the heater zone, there is a lack of heat generation on purpose to simulate the cohesive forces. This represents full-scale bridging effects from zone to zone in the field.

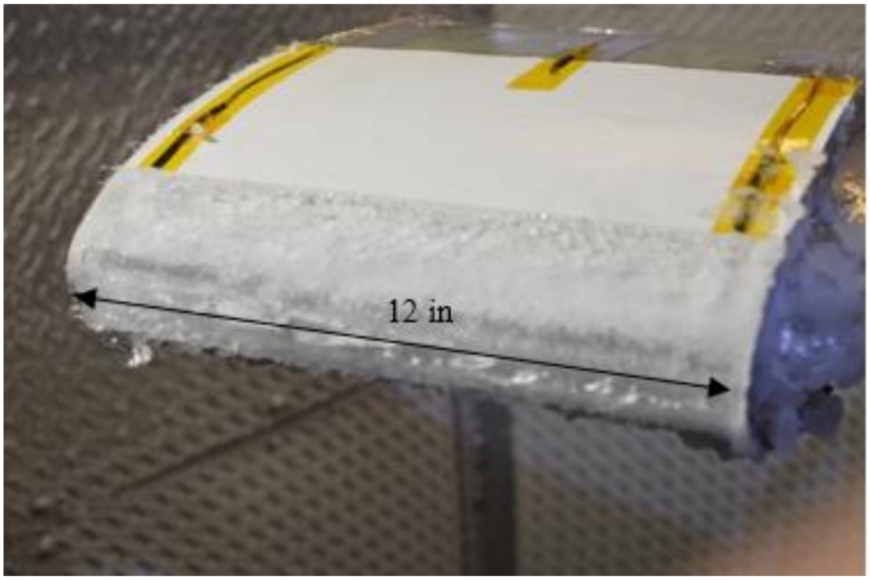

Figure 79. 9 mm ice shape at -8°C in *Medium* icing conditions.

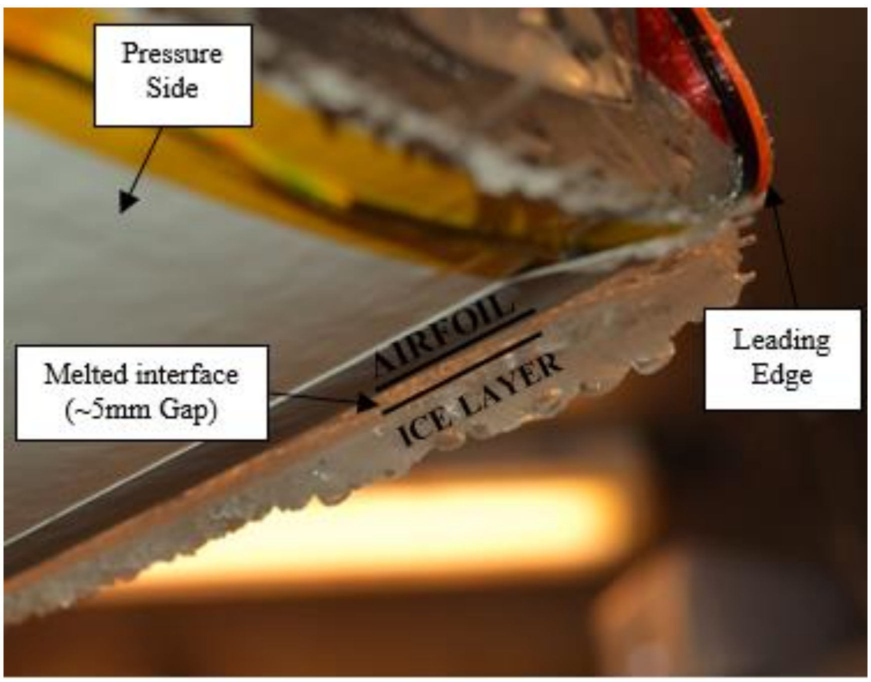

Figure 80. Melted interface of ice shape resulting in cohesive failure.

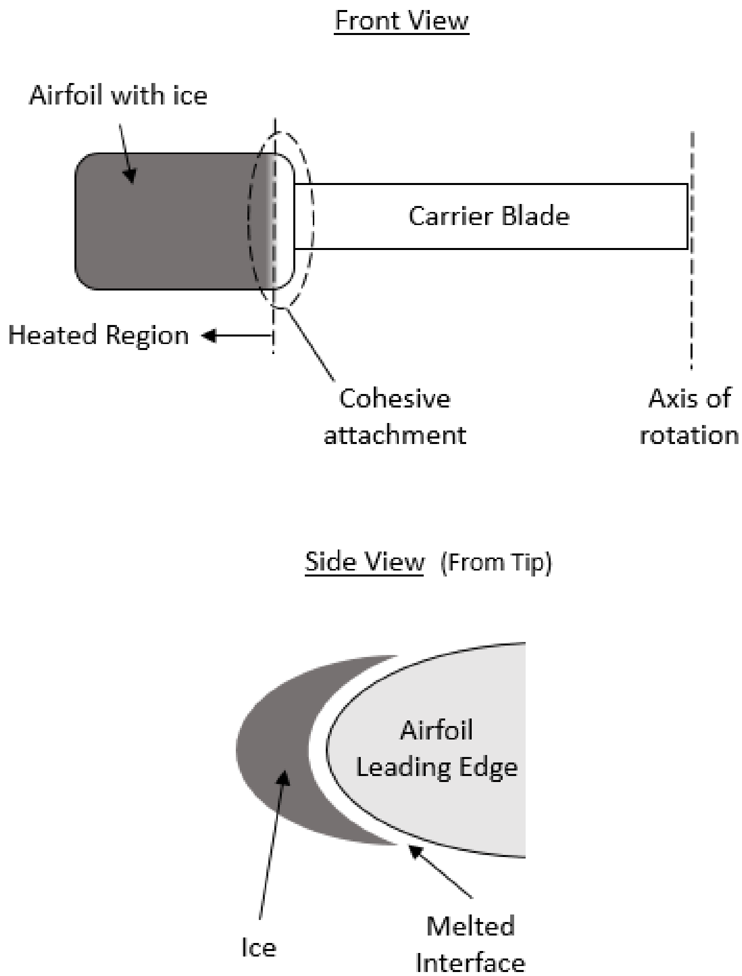

Figure 81. Schematic of melted interface experienced from cohesive failure.

A 7 mm ice shape at -8°C in *Medium* icing conditions is displayed in Figure 82. A photograph of a successful shedding event after 23 seconds for the 26.7% span correlation, the innermost heater zone, is exhibited in Figure 83.

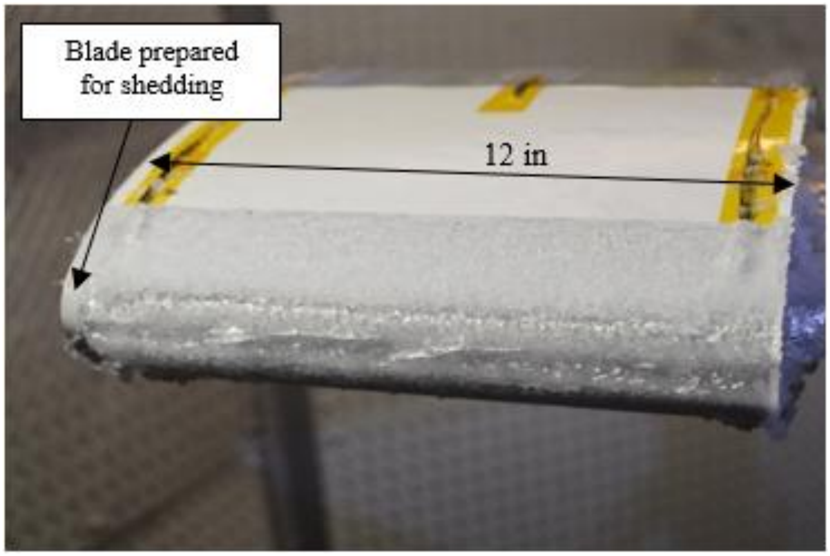

Figure 82. 7 mm ice shape at -8°C in *Medium* icing conditions.

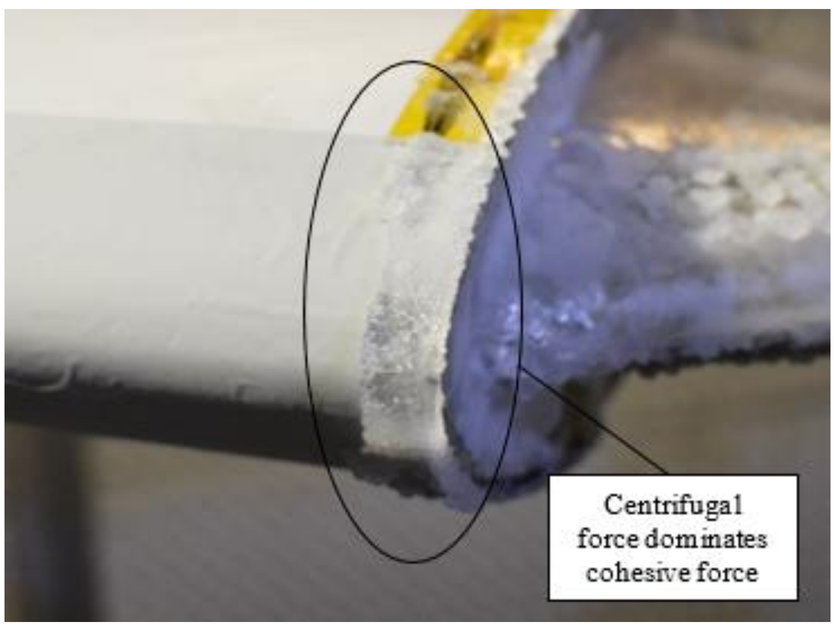

Figure 83. Successful ice shedding event.

The minimum ice thicknesses along the span for the severe icing condition were used to determine the cohesive failure curve. The cross-sectional area of the ice shape was photographed and digitized to obtain the 2D area, as stated earlier. The ice mass was used to calculate the centrifugal force at each heater span location. This data curve represents the minimum centrifugal force needed to exceed the ice cohesive force. If the ice thickness (mass) exceeds the boundary, centrifugal forces will dominate the cohesive forces. The boundary curve is presented in Figure 84.

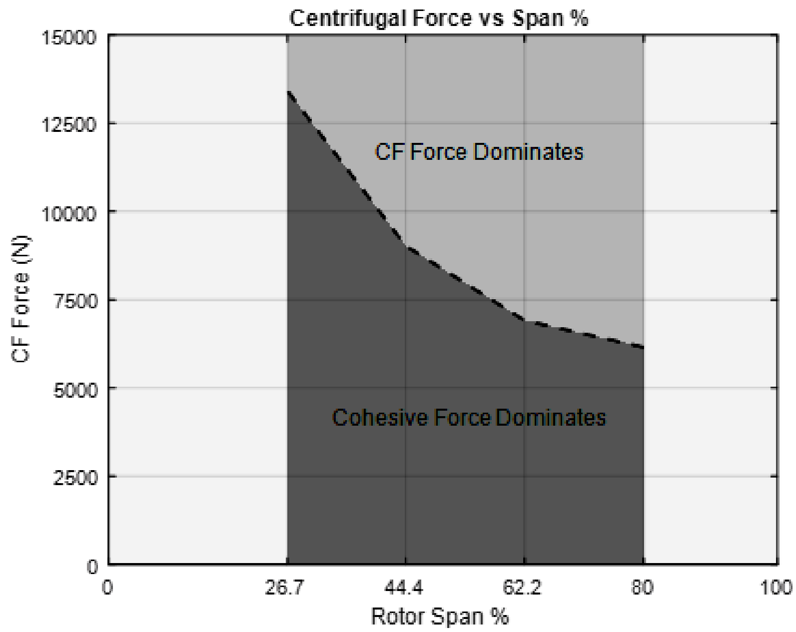

Figure 84. Cohesive failure curve.

4.2.2.3. Power Density Variation

The last area explored was the variation of power density delivered to the electro-thermal heater zones. These experiments were performed after the minimum thickness was found and analyzed for each span-wise heater zone. The objective was to quantify the required shedding times for reduced energies at the correlated minimum ice thickness. As stated in the previous section, effective ice shedding means the shedding event occurred within 30 seconds. Each test case accreted ice at a water droplet impact velocity of 52 m/s, which corresponds to 400 RPM in the AERTS facility. After the minimum thickness was accreted, the icing cloud was turned off and the rotor stand spun down. The same ice removal technique as stated earlier was conducted to eliminate the last inch of ice from the tip, span-wise. The rotor stand spun up to the desired RPM that corresponded to the centrifugal force at that heater zone. When the matching centrifugal force was achieved, power was delivered to the electro-thermal heaters at a selected power density. The maximum available power density from system requirements, 0.385 W/cm^2, was initial value before decreasing power density for the latter test cases. The ice shedding times were quantified and recorded for the *Light* and *Medium* icing conditions. To reaffirm, the L*ight* icing condition pertains to a 0.2 g/m^3 LWC and 20 µm MVD at a -8°C temperature. The M*edium* icing conditions are a 0.4 g/m^3 LWC and 20 µm MVD at a -8°C temperature. The parameters of the test matrix for the power variation experiments are shown in Table 8.

Table 8. Test matrix for de-icing IPS power variation

Heater #	**Span %**	**Heater Power Density (W/cm^2)**	**Shedding RPM in AERTS**	**Icing Condition**
4	26.7	0.385, 0.33, 0.27, 0.225	286	LIGHT & MEDIUM
3	44.4	0.385, 0.33, 0.27, 0.225	369	LIGHT & MEDIUM
2	62.2	0.385, 0.33, 0.27, 0.225	437	LIGHT & MEDIUM

The test cases for the innermost heater zone, Heater 4, accreted an average of 6 mm of ice on the leading edge in *Light* icing conditions. For the 0.385, 0.33, 0.27 and 0.225 W/cm^2 power densities, the average shedding times were 28, 35, 83 and >180 seconds, respectively. The test cases for Heater 4 on average accreted a 7 mm ice thickness on the leading edge in *Medium* icing conditions. For the 0.385, 0.33, 0.27 and 0.225 W/cm^2 power densities, the average shedding times were 22, 42, 65 and >180 seconds, respectively. The data trend for the innermost heating section, zone 4, are shown in Figure 85.

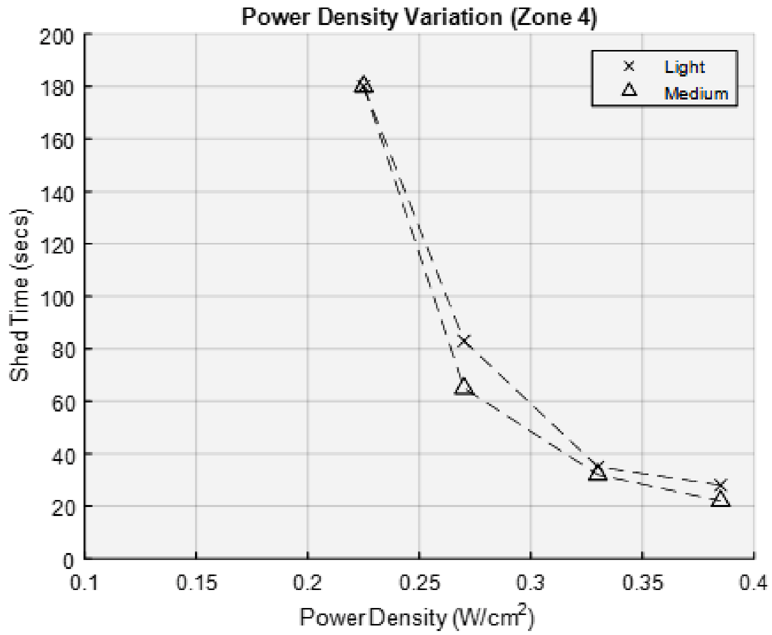

Figure 85. Power density variation for heater zone 4.

The test cases for heater zone 3 accreted an average ice thickness of 4 mm on the leading edge in *Light* icing conditions. For the 0.385, 0.33, 0.27 and 0.225 W/cm^2 power densities, the average shedding times were 25, 48, 88 and >180 seconds, respectively. Test cases in the *Medium* icing conditions accumulated an average ice thickness of 5 mm. For the 0.385, 0.33, 0.27 and 0.225 W/cm^2 power densities, the average shedding times were 25, 38, 82 and >180 seconds, respectively. The data trend for heater zone 3 is shown in Figure 86.

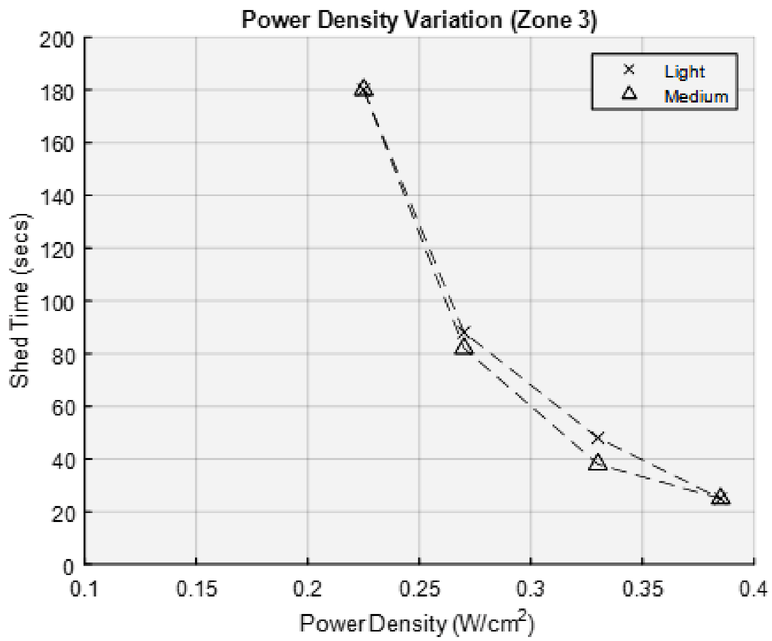

Figure 86. Power density variation for heater zone 3.

Lastly, heater zone 2 accreted 3 mm of ice on the leading edge for *Light* icing conditions. For the 0.385, 0.33, 0.27 and 0.225 W/cm^2 power densities, the average shedding times were 28, 47, 67 and >180 seconds, respectively. Test cases in the *Medium* icing conditions accreted an average ice thickness of 3.7 mm. For the 0.385, 0.33, 0.27 and 0.225 W/cm^2 power densities, the average shedding times were 24, 57, 85 and >180 seconds, respectively. The power variation data trend is presented in Figure 87.

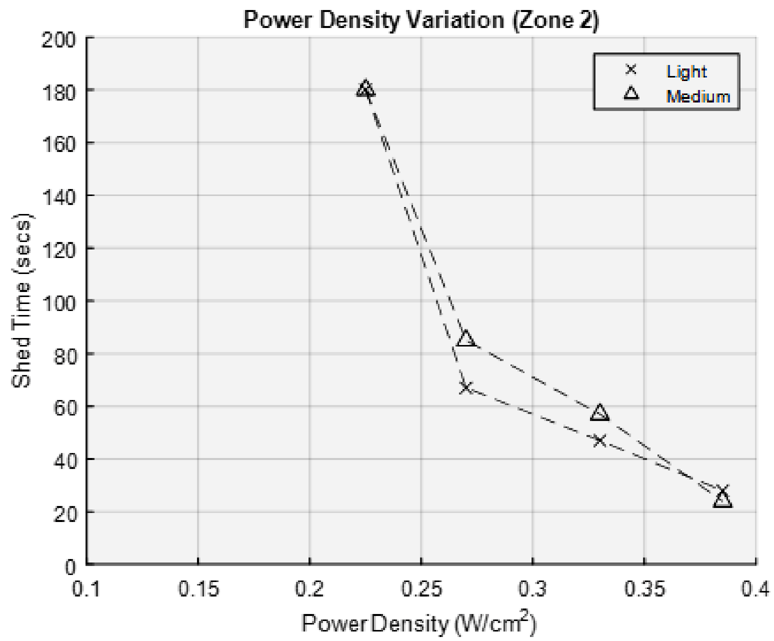

Figure 87. Power density variation for heater zone 2.

The data shows a parabolic trend indicating that the variation of power density plays a critical role in the heat transfer physics. The slightest change in power density can result in shedding times above the "effective shedding" requirement. Therefore, the maximum available power from the system requirements must be used for the de-icing ice protection system and cannot be reduced for robust de-icing.

4.2.3. Time-Sequence Controller

The controller is dependent upon the ice accretion rates, found in Table 7, and the minimum ice thickness required for effective shedding. The crucial hardware for this system is an ice detection sensor. The controller interface needs to know when ice is initially present and the ice thickness after one minute. These two steps are imperative for identifying the icing condition. The ice accretion rate determines the icing condition experienced. Each icing condition has a repeatable time sequence operation to de-ice the rotor blades. The time sequence incorporates the minimum ice thickness needed to ensure the ice accretion reaches that critical value to overcome cohesive forces. The controller time sequences for *Light*, *Medium* and *Severe* icing conditions are presented in Figures 88-90, respectively. The controller operations are illustrated as a flowchart in Figure 91.

If an ice thickness detector/sensor is not present, the Light sequence controller can be activated as a conservative approach. The ice accretion rates in the light condition are smaller, so the time it takes for the ice accretion to reach the critical thickness is longer. If the wind turbine is experiencing severe icing conditions in reality, the light sequence controller would still be successful. Although, the ice thickness on each heater section would be larger since the ice accretion would happen for a longer duration.

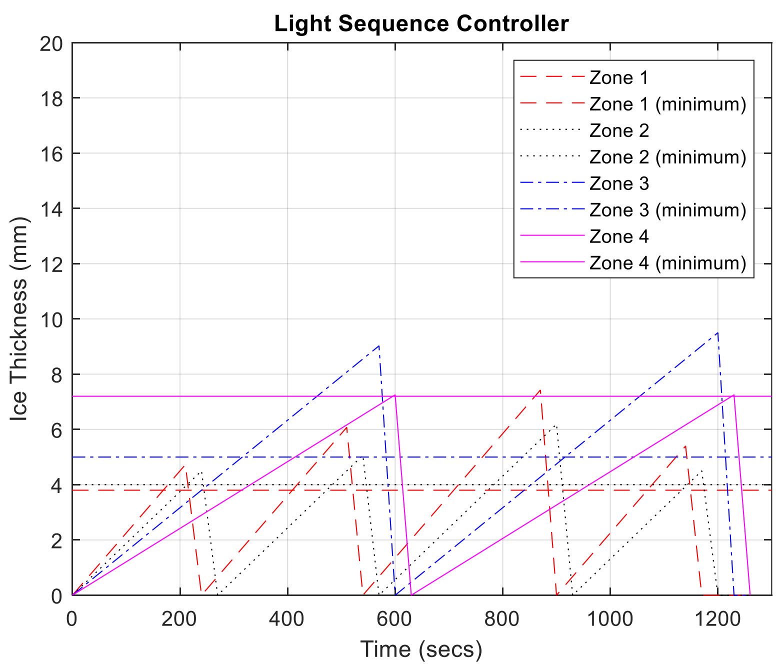

Figure 88. Repeatable time sequence for *Light* icing condition.

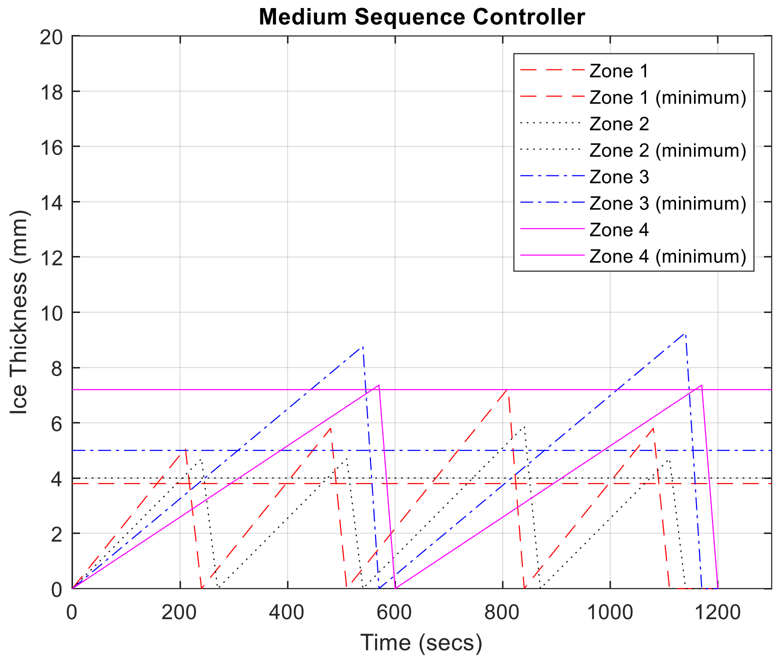

Figure 89. Repeatable time sequence for *Medium* icing condition.

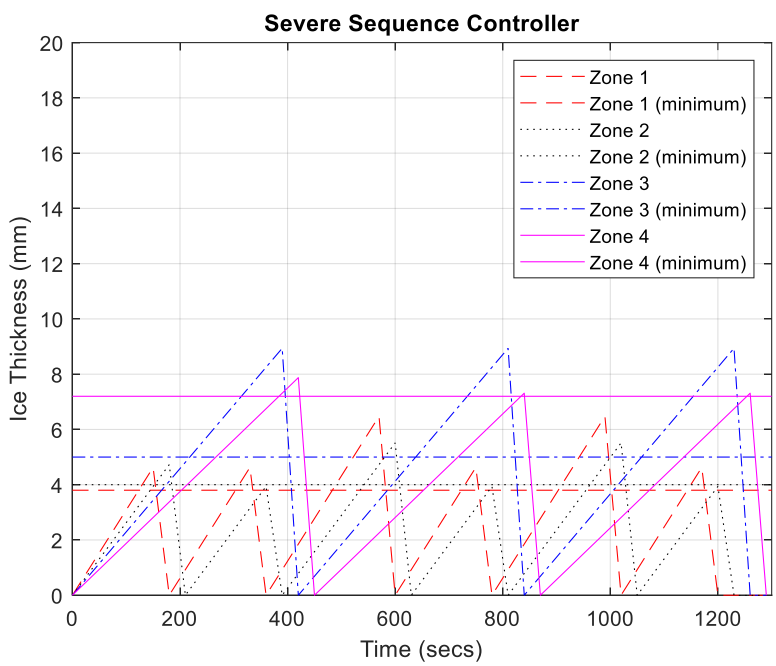

Figure 90. Repeatable time sequence for *Severe* icing condition.

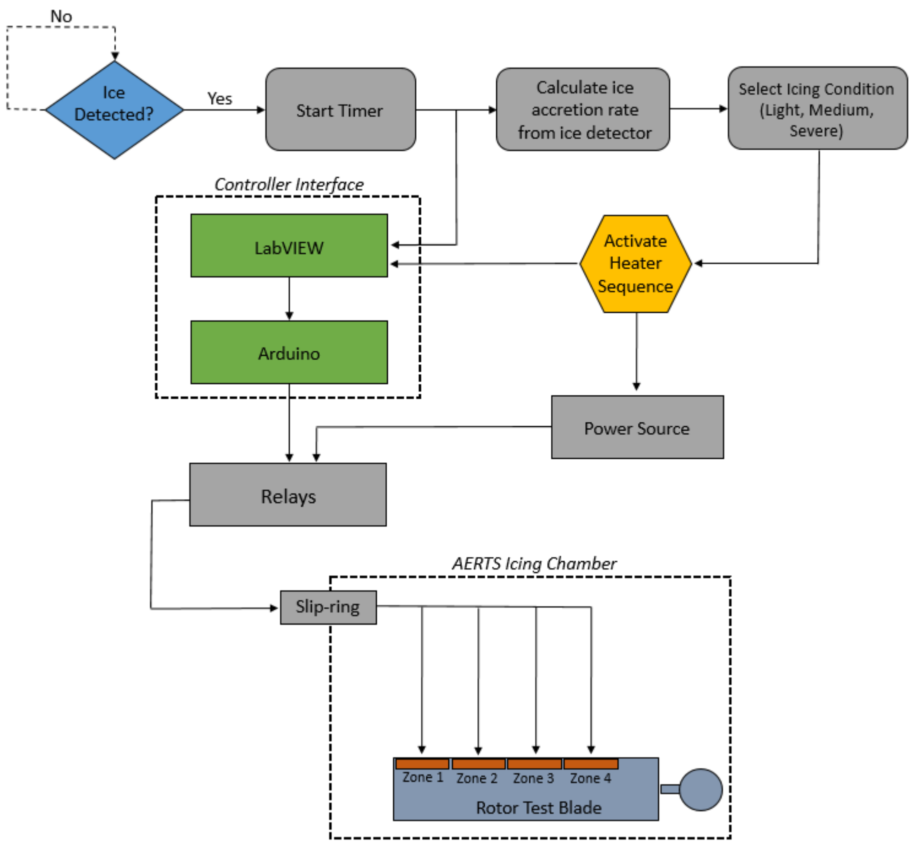

Figure 91. Flowchart of Controller operations.

Chapter 5: Conclusions and Recommendations for Future Work

5.1. Conclusions

This research effort explored anti-icing and de-icing configurations for an electro-thermal ice protection system with application to wind turbines. The airfoil selected to represent the 1.5MW wind turbine of interest was the DU 93-W-210 airfoil. The wind turbine rotor blade had 4 span-wise heater sections and each heater unit has a power density availability limit of 0.385 W/cm^2. The power limitation was guided by wind turbine operators. A LabVIEW code was developed to interface with an Arduino microcontroller to operate the heaters, read blade temperatures and quantify changes in rotor torque. The module has the capability to control and iterate relay sequencing, measure current, calculate power density, quantify torque data, read and display thermistor temperatures on the airfoil, and save all data for post processing. The anti-icing performance was compared with an analytical modeling software, LEWICE. The modeling effort focused on initial estimation of power requirements and to assess the feasibility of anti-icing schemes for wind turbines given the operator's power availability limits. Design procedures for the de-icing configuration were developed and the system's performance was experimentally evaluated.

5.1.1. Anti-Icing

The objective of this research was to find the optimum power density needed to keep the rotor blades free of ice in the anti-icing configuration. The DU93210 airfoil and its' material layers were modeled in LEWICE to predict ice shapes and temperatures on the surface of the airfoil. This model was used to guide experimental testing and to compare with experimental data from the AERTS facility at the severe icing condition. The RPM in AERTS was calculated to represent impact velocity at each heater zone span location. From this research in the anti-icing mode, the following conclusions were made:

- Thermistors 1 and 3 on the low-pressure side of the leading-edge heater produced the hottest temperatures. The average error percentage between the experimental temperature data on the suction-side and LEWICE was 39.5%.
- Thermistors 4 and 6 on the bottom-side of the leading edge read temperatures closer to the LEWICE predictions. The average error percentage between the experimental temperature data on the pressure-side and LEWICE was 11.1%.
- The output temperature vs power density had a positive correlation coefficient. The correlation coefficient for the suction-side and pressure-side of the strip heater was 0.88 and 0.95, respectively. The correlation coefficient for the aux heaters was 0.97.
- Based on experimental results, the anti-icing configuration is not feasible with the 100 kW power limitations on the full-scale wind turbine. The leading-edge strip heater requires a 0.58 W/cm^2 power density with the aux heaters producing a 0.37 W/cm^2 power density to keep the airfoils free of ice.

5.1.2. De-Icing

The objective of the de-icing configuration was to develop a process and procedure to design a de-icing ice protection system. The testing temperature in the cooling chamber was chosen based on operator's knowledge and the power density of 0.385 W/cm^2 was selected from the maximum available power requirement. The ice accretion rate was measured for each heater zone location on the rotor blade, representative of the full-scale 1.5 MW wind turbine.

- The ice accretion rates (mm/min) for 80%, 62.2%, 44.4% and 26.7% span locations in the light icing conditions were 1.35, 1.125, 0.95 and 0.725, respectively.
- The ice accretion rates (mm/min) for 80%, 62.2%, 44.4% and 26.7% span locations in the medium icing conditions were 1.45, 1.175, 0.975 and 0.775, respectively.
- The ice accretion rates (mm/min) for 80%, 62.2%, 44.4% and 26.7% span locations in the severe icing conditions were 1.85, 1.575, 1.375 and 1.125, respectively.

The minimum ice thickness required to shed was quantified by matching the centrifugal force of each heater section. The objective of these tests were to prompt shedding events within 30 seconds to satisfy the "effective shedding" requirement and overcome the ice cohesive force. The data collected from these experiments produced the capability to design heater time sequences for each icing conditions. The minimum thicknesses along the span of the wind turbine blade for the severe icing condition were considered for the time sequence design as a conservative approach to ensure the centrifugal force dominates the cohesive force of the ice.

- The minimum ice thicknesses for 62.2%, 44.4% and 26.7% span locations in the light icing condition were 2.8 mm, 4 mm and 6 mm, respectively. The ice shedding events occurred at 24s, 25s and 28s, respectively.
- The minimum ice thicknesses for 62.2%, 44.4% and 26.7% span locations in the medium icing condition were 3.7 mm, 5 mm and 6.8 mm, respectively. The ice shedding events occurred at 25s, 25s and 23s, respectively.
- The minimum ice thicknesses for 62.2%, 44.4% and 26.7% span locations in the severe icing condition were 4 mm, 5 mm and 7.2 mm, respectively. The ice shedding events occurred at 34s, 24s and 20s, respectively.

The de-icing ice protection system was designed to not exceed the power limitations on the full-scale wind turbine. The heater configuration (layers and partitions) can be optimized further by performing many iterations in the modeling phase to reduce the required power density. If icing conditions are known by operators at the wind farm location, then ice accretion rates along the span of the rotor blade can be experimentally observed and utilized to quantify the time it takes to reach the minimum thickness needed to overcome ice cohesion forces and effectively shed (≤ 30 seconds) ice on each heater section. This design process presented in this research can be applied to other wind turbines with different properties and power restrictions.

5.2. Recommendations for Future Work

For the anti-icing configuration, the minimum power density could be reduced by optimizing the heat transfer through the layers of the airfoil. Since running wet is very expensive, superhydrophobic coatings could be implemented to avoid runback issues of ice refreezing in the aft section of the airfoil. Therefore, the overall dimensions of the electro-thermal heaters is reduced to minimize power density and costs. Erosion affects of the coatings must be considered and evaluated. Also, a hybrid scheme could be explored using a parting strip at the stagnation point of the airfoil and de-icing zones aft of the parting strip in the chord-wise direction.

The design of the de-icing system is dependent upon detecting the initial presence of ice. When ice is detected and the overall icing condition is estimated, the appropriate heater sequence can be activated. In addition, the ice detection sensor would calculate the ice accretion rate after one minute and determine more accurately what type of icing condition the wind turbine will experience. Environmental data could be organized and utilized to define and standardize icing envelopes for wind turbines.

More testing efforts should be explored to further verify the de-icing ice protection system. Full-scale blade testing should be investigated to confirm the ice cohesive failure across adjacent heater sections. It is imperative that the heater section sheds the ice mass while the adjacent inboard section remains accreting ice. Also, the time sequence algorithms for each icing condition could be implemented into a controller and activated on a full-scale test.

High speed cameras could be utilized to study the fractures of ice shedding events. Ideally, the ice mass would break up into smaller pieces as it moves away from the rotor blades into the surrounding environment.

References

[1] Hepbasli A, Ozgener O. *A review on the development of wind energy in Turkey*. Renewable and Sustainable Energy Reviews 2004; 8(3):257-76.

[2] Deal WF. *Wind Power: an emerging energy resource.* Technology and Engineering Teacher 2010; 9:9-15.

[3] Price TJ, Blyth JC. *Britain's first modern wind power pioneer.* Wind Engineering 2005; 29(3):191-200.

[4] Deng Y. *Design optimization of a micro wind turbine using computational fluid.* Hong Kong: The University of Hong Kong; 2008.

[5] Ackerman T. Der LS. *An overview of winder energy status*. Renewable and sustainable Energy Reviews 2002:6(1-2):67-127

[6] Xu J. He D. Zhao X. *Status and prospects of Chinese wind energy.* Energy 2010; 35(11):4439-44.

[7] Joselin Herbert GM, Iniyan S, Sreevalsan E, Rajiapandian S. *A review of wind energy technologies*. Renewable and Sustainable Energy Reviews 2007; 11(6):1117-45.

[8] Wind power report. 7th ed. London: ABS Energy Research: 2010.

[9] Leung, Dennis, and Yuan Yang. *Wind Energy Development and Its Environmental Impact*. Renewable and Sustainable Energy Reviews 16, 2011.

[10] The Global Wind Energy Council. United States. Available from: http://www.gwec.net/index.php?id=121; 2011.

[11] The Global Wind Energy Council. PR China. Available from: http://www.gwec.net/index.php?id=125; 2011.

[12] Musial W, Butterfield S, Ram B. *Energy from offshore wind.* Offshore technology conference. Texas: Houston; 2006.

[13] Lamraoui, F., Fortin, G., Benoit, R., Perron, J., and Masson, C., *Atmospheric icing impact on wind turbine production.* Cold Regions Science and Technology, vol. 100, 2014, pp. 36–49.

[14] Feng, F., Li, S., Li, Y., and Tian, W., *Numerical simulation on the aerodynamic effects of blade icing on small scale Straight-bladed VAWT.* Physics Procedia, vol. 24, 2012, pp. 774–780.

[15] Barber, S., and Wang, Y., European Wind Energy Conference (EWEC 2010). *The Impact of Ice Formation on Wind Turbine Performance and Aerodynamics Abstract*. Wind Energy, 2010.

[16] Gillenwater, Daniel, Masson, C., and Perron, J., *Wind Turbine Performance during Icing Events.* 46th AIAA Aerospace Sciences Meeting and Exhibit, Reno, Nevada (2008).

[17] N. Dalili, A. Edrisy, R. Carriveau *A review of surface engineering issues critical to wind turbine performance*. Renewable and Sustainable Energy Reviews, Vol. 13, pp. 428-438, 2009.

[18] Han, Y. and J. Palacios (2012) *Analytical and Experimental Determination of Airfoil Performance Degradation Due to Ice Accretion.* 4th AIAA Atmospheric and Space Environments Conference, New Orleans, Louisiana, pp.1–25.

[19] Fakorede, O., Ibrahim, H., Ilinca, A., and Perron, J., *Experimental Investigation of Power Requirements for Wind Turbines Electrothermal Anti-icing Systems.* Wind Turbines - Design, Control and Applications, 2016.

[20] Lehtomäki, V., *Wind Energy in Cold Climates Available Technologies*. 2016.

[21] Ruff, G. and Berkowitz, B. *User's Manual for NASA Lewis Ice Accretion Prediction Code. 1990.* NASA CR 185129.

[22] Heinrich, A. et al., *Aircraft Icing Handbook, Volumes I-III.* Atlantic City International Airport, NJ: FAA Technical Center, 1991. DOT/FAA/CT-88/8-1, AD-A238 039.

[23] Ide, R.F. and Oldenburg, J.R., *Icing Cloud Calibration of the NASA Glenn Icing Research Tunnel.* AIAA-2001-0234 and NASA/TM – 2001-210689, 39th Aerospace Sciences Meeting and Exhibit, January 2001.

[24] Federal Aviation Regulation Part 25 *Airworthiness Standards: Transport Category Airplanes* and Part 29 *Airworthiness Standards: Transport Category Rotorcraft*. FAA, Washington DC.

[25] Flemming, R., A *History of Ice Protection System Development at Sikorsky Aircraft.* Chicago, IL: FAA In-Flight Icing/Ground De-Icing International Conference and Exhibition, 2003. 2003-01-2092.

[26] Botura, G., Sweet, D., and Flosdorf, D. *Development and Demonstration of Low Power Electrothermal De-icing System*. Reno, NV: 43rd AIAA Aerospace Sciences Meeting and Exhibit, 2005. AIAA 2005-1460.

[27] Buschhorn, S. et al., *Electro thermal Icing Protection of Aero surfaces using Conductive Polymer Nanocomposites.* Boston, AIAA, 2013. AIAA 2013-1729.

[28] Samuel T. Buschhorn, Seth S. Kessler, Noa Lachmann, Jennifer Gavin, Greg Thomas, and Brian L. Wardle. *Electrothermal Icing protection of Aero surfaces Using Conductive Polymer Nanocomposites.* 54thAIAA/ASME/ASCE/AHS/ASC Structures, Structural Dynamics, and Materials Conference, pages 1–8, 2013.

[29] Brouwers, E. Peterson, A. Palacios, J. Centolanza, L., *Ice Adhesion Strength Measurements for Rotor Blade Leading Edge Materials*. Virginia Beach, VA: AHS-2011-272.

[30] Burkett, B., *Ice Phobic Coatings on Controlled and Covered Surfaces*. Fort Worth, American Helicopter Society 68th forum, 2012.

[31] Coffman, H., *Helicopter Rotor Icing Protection Methods*. Journal of the American Helicopter Society, April 1987, Vol. 32.

[32] Goehner, R., Glover, N., Hensley D., *Electro-Impulse-Deicing*-EIDI: ERDC/CRREL TR-09-X, 1987.

[33] Charles a. Martin and James C. Putt. *Advanced pneumatic impulse ice protection system (PIIP) for aircraft*. Journal of Aircraft, 29(4):714–716, 1992.

[34] W Geer and M Scott. *The Prevention of the Ice Hazard on Airplanes*. Technical report, Washington D.C., 1930.

[35] Wright, W. *User's Manual for LEWICE Version 3.2*. NASA/CR-2008-214255 (2008).

[36] Wright, W. B. and Rutkowski, A., *Validation Results for LEWICE 2.0*. NASA CR 208690, Nov. 1998.

[37] Brouwers, E., *The Experimental Investigation of A Rotor Icing Model with Shedding*. Master Thesis, May 2010.

[38] Banta, R.M., Kelley N.D., Pichugina, Y.L. and Brewer, W.A., *Atmospheric Remote Sensing for Improving Wind Energy Technology*. NOAA-NREL SEAS Lecture, Sept 2009.

[39] Vargas, Mario, et al. *Local and Total Density Measurements in Ice Shapes*. NASA, Mar. 2005.

[40] Overmeyer, Austin D. *Actuator Bondline Optimization and Experimental Deicing of a Rotor Blade Ultrasonic Deicing System*. The Pennsylvania State University, May 2012.

[41] B Wright. *User Manual for the NASA Code Ice Accretion Code LEWICE*. August 2002. NASA Glenn, Cleveland, Ohio, 2018.

[42] Blasco, Peter M. *An Experimental and Computational Approach to Iced Wind Turbine Aerodynamics*. The Pennsylvania State University, 2015.

[43] Han, Yiqiang. *Theoretical and Experimental Study of Scaling Methods for Rotor Blade Ice Accretion Testing*. The Pennsylvania State University, Aug. 2011.